THE EFFECT OF CAPILLARY CONDENSATION ON THE GEOMECHANICAL AND ACOUSTIC PROPERTIES OF TIGHT FORMATIONS

by

Aamer Albannay

A thesis submitted to the Faculty and the Board of Trustees of the Colorado School of Mines in partial fulfillment of the requirements for the degree of Doctor of Philosophy (Petroleum Engineering).

Golden, Colorado

Date _____

Signed: _____
Aamer Albannay

Signed: _____
Dr. Azra Tutuncu
Thesis Advisor

Signed: _____
Dr. Binh Bui
Thesis Advisor

Golden, Colorado

Date _____

Signed: _____
Dr. Jennifer Miskimins
Associate Professor and Interim Head

Department of Petroleum Engineering

ABSTRACT

The main objective of this research is to experimentally assess how capillary condensation affects the mechanical and acoustic properties of tight rocks. In order to do so, a new facility was built to experimentally investigate the changes in the mechanical and acoustic properties due to capillary condensation. The experimental set-up is capable of the simultaneous acquisition of coupled stress, strain, resistivity, acoustic and flow data. Carbon dioxide was used as the pore pressure fluid in these experiments.

Capillary condensation is the condensation of the gas inside nanopore space at a pressure lower than the bulk dew point pressure as a result of multilayer adsorption. Capillary condensation occurs due to the high capillary pressure inside the small pore throat of unconventional rocks. This condensation affects the phase behavior of the pore fluid, which in turn significantly impacts hydrocarbon-in-place evaluation and assessment. Due to condensation, the mechanical and acoustic properties of the rock may change. Acoustic properties variation due to capillary condensation provides us a tool to monitor phase change in reservoir as a result of nano-confinement as well as mapping the area where phase change occurs. This is particularly important in tight formations where confinement has a strong effect on phase behavior that is challenging to measure. Acoustic data provides an indirect tool for this purpose. It can also be used to characterize pore size distribution. Theoretical studies have examined the effects of capillary condensation, however, these findings have not been verified experimentally.

The main components of the experimental facility are: triaxial load cell, pore fluid injection system, back pressure system, vacuum system, axial and confining pressure system and a temperature control system. The axial and confining pressure system is capable of simultaneously applying overburden pressure (axial) and isotropic horizontal stress (confining pressure). The facility can handle stress and pore pressure up to 10,000 psi with temperature

up to 100°C. Both top and bottom axial pistons are equipped with 1 MHz resonant frequency compressional (P) and shear (S) wave transducers. A serial digital communication protocol acquires and transfers pressure and syringe volume data from pump controllers. The system temperature fluctuation of 0.1°C ensures reliable high-quality data due to minimal temperature disturbance since pore volume change due to capillary condensation and permeability measurements are very sensitive to temperature changes.

In this research, I conducted a series of experimental investigations to study the changes in the acoustic and geomechanical properties using core samples from the Diyab and Austin Chalk formations with and without capillary condensation. Carbon dioxide was used as the pore fluid in these experiments. Nitrogen adsorption experiments were also conducted to characterize the pore size distribution of the core samples. A grain-contact model was developed to predict the mechanical and acoustic changes of the samples during the experiments. The model is capable of predicting changes in acoustic and mechanical properties with temperature, phase saturation, frequency, pore pressure and effective stress. Results of the model prediction show a good match to the experimental data.

Experimental data on core samples tested from the Austin Chalk and the Diyab formations show a 5% increase in Young's Modulus as carbon dioxide condensation occurs. This increase is attributed to the increase in pore stiffness as condensation occurs reinforcing the grain contact. We also observed a noticeable increase in shear velocity when capillary condensation occurs. This is because of the confined fluid's lower mobility and higher resistance to shear relative to the gas phase. These geomechanical and acoustic signatures were observed at around 750-800 psi at 27°C which is lower than the unconfined CO_2 bulk dew point pressure of 977 psi. These experimental findings are the first observation of the signature of capillary condensation on the acoustic and mechanical properties of tight samples. Therefore, it is recommended to further investigate this phenomenon in field-scale and to use acoustic data as a tool for monitoring condensation during the lifecycle of the reservoir.

TABLE OF CONTENTS

LIST OF FIGURES

LIST OF TABLES

LIST OF SYMBOLS

Deformation . . . . . α

Interfacial tension . . . . . γ

Change in enthalpy in a closed system . . . . . ΔH

Amplitude of oscillation . . . . . Δh

Change in elastic energy of two spheres in contact . . . . . ΔU_E

Change in surface energy between two spheres . . . . . ΔU_S

Cross-sectional area of molecule . . . . . δ_a

Kronecker delta . . . . . δ_{ij}

Binary interaction coefficient for component m . . . . . δ_{mn}

Strain . . . . . ε

Dielectric constant of the spheres . . . . . ε_1

Dielectric constant of the fluid . . . . . ε_3

Contact angle . . . . . θ_c

Inverse Debye-Huckel length parameter . . . . . κ

Lame's coefficient . . . . . λ

Viscosity of gap fluid . . . . . μ

Vapor-like average density . . . . . ρ_A

Fluid density . . . . . ρ_F

Matrix density without kerogen . . . . . ρ_G

Kerogen density . . . . . ρ_K

Bulk density . . . . . ρ_b

Reservoir density gradient of hydrocarbon . . . . . ρ_h

Matrix density . . . . . ρ_m

Stress . . . . . σ

Maximum in-situ horizontal stress . . . . . σ_H

Collision parameter . . . . . σ_{cp}

Minimum in-situ horizontal stress . . . . . σ_h

Vertical stress . . . . . σ_v

Shear stress . . . . . τ

Poisson's Ratio . . . . . ν

Dynamic Poisson's Ratio . . . . . ν_{dyn}

Static Poisson's Ratio . . . . . ν_{st}

Porosity . . . . . ϕ

NMR total porosity . . . . . ϕ_{NMR}

Friction angle . . . . . ϕ_f

Zeta potential . . . . . ψ

Angular frequency . . . . . ω

Acentric factor for component m . . . . . ω_m

Hamaker constant . . . . . A

BET surface area . . . . . A_s

Wave number C

Coordination number . . . . . C_n

Gas compressibility . . . . . c_g

Peneloux volume correction factor for component m . . . . . c_m

Conversion factor . . . . . CF

Viscous resistance . . . . . D_o

Young's Modulus . . . . . E

Dynamic Young's Modulus . . . . . E_{dyn}

Static Young's Modulus . . . . . E_{st}

Electronic charge . . . . . e

Applied force . . . . . F_o

Total Surface Force . . . . . F_{ts}

Frequency . . . . . f

Shear modulus . . . . . G

Hydrogen index of the pore fluid . . . . . HI_{PF}

Plank's constant . . . . . h

Initial separation distance . . . . . h_o

Zeroth order Bessel function . . . . . J_0

Bulk modulus . . . . . K

Structural constant . . . . . K_1

Gap stiffness . . . . . K_{gap}

Bulk modulus of saturated fluid . . . . . K_{fluid}

Normal stiffness of dry matrix . . . . . $K_{n,m}$

Tangential stiffness of dry matrix . . . . . $K_{t,m}$

Permeability . . . . . k

Boltzman constant . . . . . k_{BM}

Inertia . . . . . L_o

Structural constant l

Compressional modulus . . . . . M

Avogadro's number . . . . . N_a

Ion concentration . . . . . n

Refraction index of the solid spheres . . . . . n_1

Refraction index of the fluid . . . . . n_3

Number of components . . . . . n_c

Number of moles at the monolayer . . . . . n_m

Langmuir pressure . . . . . p_L

Capillary pressure . . . . . p_c

Capillary pressure in gas - brine . . . . . $p_{c(g/w)}$

Capillary pressure in mercury-air . . . . . $p_{c(m/a)}$

Dew point pressure . . . . . p_d

Gas pressure . . . . . p_g

Pressure of non-wetting phase . . . . . p_{nw}

Saturation vapor pressure . . . . . p_o

Pressure of wetting phase . . . . . p_w

Radius of grain . . . . . R

Gas constant . . . . . R_g

Cohesion . . . . . S_0

Oil saturation . . . . . S_o

Gas saturation . . . . . S_g

Temperature . . . . . T

Critical point temperature . . . . . T_C

Pore critical temperature . . . . . T_{CP}

Critical temperature of component m . . . . . $T_{c,m}$

Hysteresis critical temperature . . . . . T_h

Wave arrival time . . . . . $t_{arrival}$

Reduced critical temperature of component m . . . . . $T_{r,m}$

Volume of adsorbed gas . . . . . V_A

Maximum adsorption capacity . . . . . V_L

Liquid molar volume . . . . . V_{LM}

Volume of gas necessary to form a monolayer . . . . . V_M

Pore volume . . . . . V_P

Amount of adsorbed gas . . . . . V_a

Fluid velocity vector . . . . . $\mathbf{u}$

Specific volume v

Adsorption frequency of fluid . . . . . v_e

Volumetric flow rate . . . . . W

Dissipative contacts density factor X

Liquid molar composition for component m . . . . . x_m

Vapor molar composition for component m . . . . . y_m

Valence of electrolyte . . . . . Z

Gas deviation factor . . . . . z

Rackett compressibility factor for component m . . . . . $z_{R,m}$

LIST OF ABBREVIATIONS

Abu Dhabi National Oil Company	ADNOC
Advanced Surface Facies Logging	ASFL
Brunauer-Emmett-Teller	BET
Combinable Magnetic Resonance	CMR
Diagnostic Fracture Injection Testing	DFIT
Drill-Stem Test	DST
Energy Information Administration	EIA
Equation of State	EOS
Grand Canonical Monte Carlo	GCMC
Heterogeneity Rock Analysis	HRA
Hydrocarbon In Place	HCIP
International Union of Pure and Applied Chemistry	IUPAC
Mercury Injection Capillary Pressure	MICP
Mobil Composition of Matter No. 41	MCM-41
Mohr-Coulomb	MC
Non-Local Density Function Theory	NLDFT
Nuclear Magnetic Resonance	NMR
Pulsed Field Gradient Nuclear Magnetic Resonance	PFG NMR
Repeat Formation Tester	RFT
Santa Barbra Amorphous No. 15	SBA-15

Standard Temperature and Pressure . . . . . STP

Total Organic Carbon . . . . . TOC

Unconfined Compressive Strength . . . . . UCS

Unconventional Natural Gas and Oil Institute . . . . . UNGI

Vapor-Liquid Equilibria . . . . . VLE

X-ray Diffraction . . . . . XRD

X-ray Fluorescence . . . . . XRF

ACKNOWLEDGMENTS

The six years I have spent on this academic journey have been remarkable to say the least. Remarkably exciting, frustrating, empowering, trying, but most of all: fulfilling. My quest in the search for capillary condensation has been filled with plot twists when I least expected them and helpful allies when I needed them the most. None of it would have been possible without the support of my advisor, the late Dr. Azra Tutuncu, who helped me every step of the way. Thank you for believing in me and pushing me when I needed it. Most of all, thank you for being one of the kindest people I've ever met. It is because of you that I got involved in geomechanics.

I would also like to thank ADNOC for giving me this incredible opportunity to pursue my graduate studies. I wouldn't have been able to do it without their support and I look forward to continue working for them in the near future. I will also do my best to stay involved with future joint ADNOC-Mines collaborations so I can have an excuse to come back and visit a place that feels like my second home.

A very special thank you to Dr. Kazemi who has helped me unravel the many mysteries of confinement and adsorption. I would like to thank Dr. Ozkan for his his insight on phase behavior and for his contagious positivity. Thank you Dr. Sonnenberg for helping me find the right cores for my experiments. I had the most fun taking your geology classes which were a welcome change of pace from all the PE classes. I would also like to thank Dr. Tura for being the most accommodating chairman one could ask for.

I am going to miss the days of working in the UNGI office and all the familiar faces that now feel like family to me. Thank you Dr. Bui for introducing me to capillary condensation and for answering my 165322 questions I had for you. You are a UNGI cornerstone and all of us appreciate everything you've done to help us progress our research and graduate especially after the loss of Dr. Tutuncu. I would also like to thank Dr. Katsuki for his

help in the lab and for putting up with all the countless modifications and iterations to my experiments.

This journey wouldn't have been possible without the incredible friends that I met during my time here in Colorado. Thank you so much for your being there for me through it all. A most special thank you to the Griffins who became the closest thing I have to a family here. You will forever be in my heart no matter the distance and we will reunite soon enough.

Grandma Feryal. Just thinking of you right now makes my eyes water. Thank you so much for your unconditional love, kindness and for being a source of pure joy. You were always there to listen, comfort and hug me when I needed it. Finally, I would like to thank my incredible mother. A woman who has selflessly dedicated her life to raising her only child and put her dream of getting a PhD on hold. But times have changed. My mother got to pursue and achieve her dream when I left to the US for my undergraduate studies. She became the first Emirati to ever get a PhD in Pharmacoeconomics. Now, I follow her footsteps.

To my mother

To my grandmother

To single mothers. For they are gods among men.

In loving memory of Dr. Azra Tutuncu

CHAPTER 1
INTRODUCTION

Unconventional reservoirs such as tight oil and shale gas formations are defined as tight rock formations with significant quantities of hydrocarbons in place that cannot be economically produced by conventional means. Shale gas reserves and production have grown rapidly with shale reservoirs quickly becoming a major source of natural gas in the United States. The Energy Information Administration (EIA) estimates that 345 billion barrels of recoverable oil and 7,300 trillion cubic feet of recoverable gas are stored in shale formations worldwide. This makes shale oil accountable for 9% of total (proven and unproven) oil reserves and shale gas accountable for 32% of total gas reserves (EIA 2014).

1.1 Shale Properties

Nanodarcy permeabilities, fine grain sizes and complex mineral compositions impede the production of these otherwise abundant quantities. The development of unconventional resources is supported by new technology and an improved understanding of fluid transport, geomechanics, pore characterization and fluid-rock interactions. These physical characteristics complicate conventional ways of estimating hydrocarbon in place and make it difficult to predict reservoir performance. In order to properly estimate hydrocarbon recovery, petrophysical properties of the shale are combined with reservoir fluid properties to be able to interpret well logs, estimate hydrocarbon in place and drainage areas, evaluate well spacing and different production scenarios as well as predict ultimate recovery.

Shale matrix is characterized by low permeability and very tight pore space. As a result, it is often a major challenge to characterize and determine pore size distribution. Javadpour et al. (2007) demonstrated that 90% of the 152 shales sampled from nine North American reservoirs have a matrix permeability less than 150 nd. In addition to low permeability, pore

sizes are very small with pore throat diameters typically ranging from 0.5 to 100 nm (Nelson 2009; Ambrose et al. 2010; Curtis et al. 2010; Sondergeld et al. 2010).

The small pore size makes the determination of pore size distribution even more challenging. Conventional mercury injection would not be ideal since mercury may not be able to access the pores in the nanoscale range. Intrusion pressure in mercury capillary pressure experiments on Barnett samples is as high as 60,000 psi (which translates to a minimum pore size of 3.6 nm). Therefore, NMR and adsorption testing are preferable methods to study shale pore size characterization (Sigal 2013; Wang et al. 2016). However, these methods are typically expensive and require a high level of expertise during measurement. The accuracy of the NMR method is also dependent upon sample preparation. Therefore, a simpler method for pore size distribution in shales is needed which is one of the focus areas of this research study.

1.2 Capillary Pressure in Shale

Capillary pressure in shale is very high due to small pore size. Experimental data from the Bakken shale samples examined by Karimi and Kazemi (2015) show that capillary pressure in shale samples can be as high as 400-600 psi. Since pore size is very small, capillary pressure plays a significant role in governing fluid flow within the pore's confining space and its interaction with adjacent fluid and rock. This capillarity greatly impacts fluid phase behavior within the nanopores resulting in a large amount of hydrocarbon adsorption (Satik et al. 1995; Shapiro and Stenby 1997; Li et al. 2014; Li et al. 2016).

Due to high capillary pressure and confining nanopores, gas within the tighter sections of the nanopores condenses into liquid at a pressure lower than its usual dew point pressure. On the other hand, larger pores are occupied with gas. Once condensation occurs, a meniscus immediately forms between the liquid-gas interface creating an equilibrium between the two phases. The curvature of the meniscus depends on the interfacial tension and the shape of the pore. In theory, as gas condenses into liquid, the acoustic properties of the shale formation is anticipated to change as the bulk density and modulus of the fluid increase;

however, these effects have not been studied experimentally yet.

The high capillary pressure in shale significantly shifts the fluid's thermodynamic properties including its phase composition and dew point pressure (Shapiro and Stenby 1996). The confinement in nanopores changes the fluid's critical properties which affects phase equilibrium and behavior (Rowlinson and Widom 1982; Satik et al. 1995; Shapiro and Stenby 1997; Espósito et al. 2005; Sing and Williams 2012; Nojabaei et al. 2013; Tan and Piri 2015). This in turn affects the hydrocarbon-in-place evaluation of the formation and production decline of shale gas reservoirs (Nojabaei et al. 2013). Production from nanopores is further enhanced due to the decrease in bubble point pressure and dew point pressures. Didar and Akkutlu (2013) noticed that as pore size decreases, the critical temperature and pressure of methane used in their experiment reduced which in turn increased z-factor and formation volume factor resulting in the overestimation of GIP.

Since pore size is at the micrometer scale in conventional reservoirs, capillary condensation does not occur, and the shift in the fluid's thermodynamic properties does not take place. However, the nano-sized gap between grains in shale creates the ideal environment for capillary condensation to occur which further complicates the phase behavior of the pore fluid. It is important to properly understand these effects since misinterpreting them could result in an inaccurate evaluation and wrong interpretation of reserve and production forecast. Chen et al. (2013) observed that due to condensation, the amount of hydrocarbon in the reservoir is often higher than the initial estimation without accounting for capillary pressure due to capillary condensation.

1.3 Effects of Confinement and Implications

Since the physical behavior of fluids in confined space is different from that in bulk, an improved understanding of the effects of confinement is important in all aspects of exploration and production (Zarragoicoechea and Kuz 2004; Seigh et al. 2009).

When dealing with pore diameters at the nanoscale level, molecular size and mean free paths cannot be ignored. Distances between molecules are decreased resulting in larger inter-

molecular forces. As a result, phase behavior of confined fluid becomes not only a function of fluid-fluid interaction (as in bulk), but also a function of fluid-pore wall interactions. These forces will be discussed in detail in subsequent chapters of this thesis.

Theoretical studies have been developed to help improve our understanding of capillary condensation, yet many of them use theoretical models using equations of state that have been used for bulk fluids (Barsotti et al., 2016). These studies along with their limitations are discussed in the literature review section of this thesis. It is therefore important to develop a novel method to experimentally observe and understand the effects of capillary condensation in unconventional reservoirs.

Developing a new experimental procedure to observe capillary condensation by studying the changes in the mechanical and acoustic properties of samples as the confined fluids undergo phase changes is the main objective of our research study. When gas condenses into liquid, the bulk density of the fluid increases which would be represented by an increase in compressional and shear wave velocities.

1.4 Objectives

The main objective of this study is to investigate the effect of capillary condensation on the acoustic and mechanical properties of shale formations and to validate theoretical models that demonstrate these effects. The detailed objectives of this study are:

1. To design the experimental facility and procedure to investigate the changes in mechanical and acoustic properties due to capillary condensation in a wide range of pressure, stress and temperature.

2. To characterize pore size distribution by studying the adsorption potential of the core samples used.

3. To develop a model for predicting changes in mechanical and acoustic properties with changes in stress, temperature, frequency and condensation.

1.5 Scientific Contribution of Research

The main scientific contributions of this research are:

- This research provides the theoretical and experimental verification that acoustic measurements can be used as means of detecting the dew point and bubble point in the nanopores of tight formations.
- Improving our understanding on how bulk fluid properties change due to confinement and capillary condensation.
- Verifying and improving grain-contact models currently used that can predict the effects of capillary condensation on the bulk properties of the rock.
- Improving hydrocarbon in place estimation for shale gas reservoirs. Accounting for the condensed gas can significantly change hydrocarbon in place estimation. This could greatly impact the economic feasibility of project development.

Furthermore, this research sheds light on formation characterization with condensation. This could be implemented in large-scale seismic surveys to monitor the phase change of fluid in the reservoir and to detect the condensation of gas near the wellbore. The findings from this research can also be utilized to construct a phase diagram/envelope for tight formations accounting for the effect of nano-confinement by running a series of experiments at different temperatures. Finally, studying the acoustic and geomechanical signature as condensation occurs can be used in assessing the impact to gas flow and transport in the reservoir as condensation occurs.

1.6 Organization of Thesis

This thesis is organized as follows:

Chapter 1 introduces capillary condensation, confinement and unconventional reservoir properties followed by an outline of the objectives and scientific contribution of the research.

Findings from a literature review that are relevant and applicable to the scope of the research are presented in Chapter 2. Concepts such as adsorption, the Kelvin equation, fluid-rock interaction and phase behavior are discussed.

Chapter 3 details how acoustic waves propagate in nanoporous mediums as well as introduce equations and method to calculate mechanical properties from acoustic wave velocities. In this chapter, a grain contact model is developed to model the effects of mechanical and acoustic properties due to changes in stress, temperature, pressure and capillary condensation. The details of how this model was developed and used in this study are summarized in this chapter.

Chapter 4 outlines the characterization of the Diyab and Austin Chalk reservoirs and the properties of the tested samples in this study. Input parameters used in the model are determined in this chapter.

Experimental investigations are presented in Chapter 5. In this chapter, I detail the recently developed experimental facility and its capabilities. The experimental procedure used in this study is also outlined in this chapter.

Chapter 6 presents the results and discusses their implications. The chapter starts by discussing adsorption results, where pore size distribution was characterized using different methods. Then, I present the mechanical properties of the samples obtained from tri-axial experiments. The experimental data is validated with my grain-contact model results. Results from capillary condensation experiments are discussed and compared with model predictions.

Chapter 7 summarizes the findings of my research and provides recommendations for future work and practical applications.

CHAPTER 2

LITERATURE REVIEW

Proper understanding of the effects of fluid confinement is of significant importance in many disciplines ranging from catalysis chemistry, geochemistry, nano-materials, material characterization, adhesion mechanics as well as hydrocarbon production from tight formations. When working in the mesopore range, the size of molecules and mean free path cannot be ignored as is in the case with conventional reservoirs. Distances between molecules are decreased at this scale due to confinement leading to higher intermolecular forces. As a result, phase behavior becomes not only a function of fluid-fluid interactions, but also a function of fluid-pore wall interactions. The adsorptive and capillary forces alter phase compositions, boundaries, fluid densities, viscosities, saturation pressures and interfacial tensions. This literature review summarizes the recent findings from research into capillary condensation and its application in the petroleum literature.

2.1 Nanopore Confinement

Figure 2.1(a) is from a capillary condensation simulation study illustrating how fluid molecules are unevenly distributed inside a pore space due to fluid-pore wall interaction (Walton and Quirke, 1989). The density is localized in the confined space with more molecules near the pore wall. Density here refers to the confined density which is the amount of moles of fluid in the pore divided by total pore volume as shown in Figure 2.1(b). As it is evident, two different phases may exist within nanopores and are important to study the recovery process in tight formations.

The first phase is vapor-like, uncondensed gas, with an average density ρ_A. While the second phase is liquid-like, condensed liquid, with an average density ρ_L. The uncondensed vapor/adsorbed phase consists of molecules that are mostly adsorbed on the pore walls with a defined density between that of the bulk vapor phase and the condensed phase. This

adsorbed phase and the bulk vapor phase outside the pore are in thermodynamic equilibrium before capillary condensation occurs. At the point of condensation, the new equilibrium is influenced by the condensed phase as well. After transition occurs, the condensed phase replaces the adsorbed phase in equilibrium.

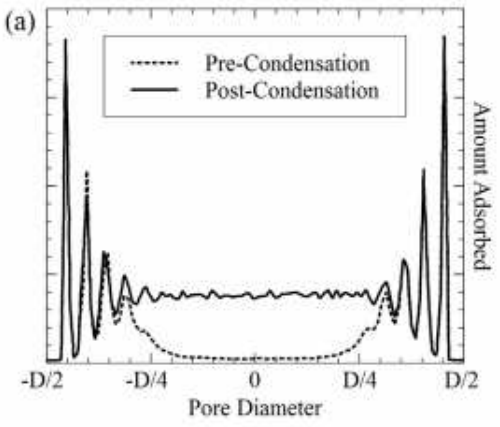

(a) Local densities within a pore

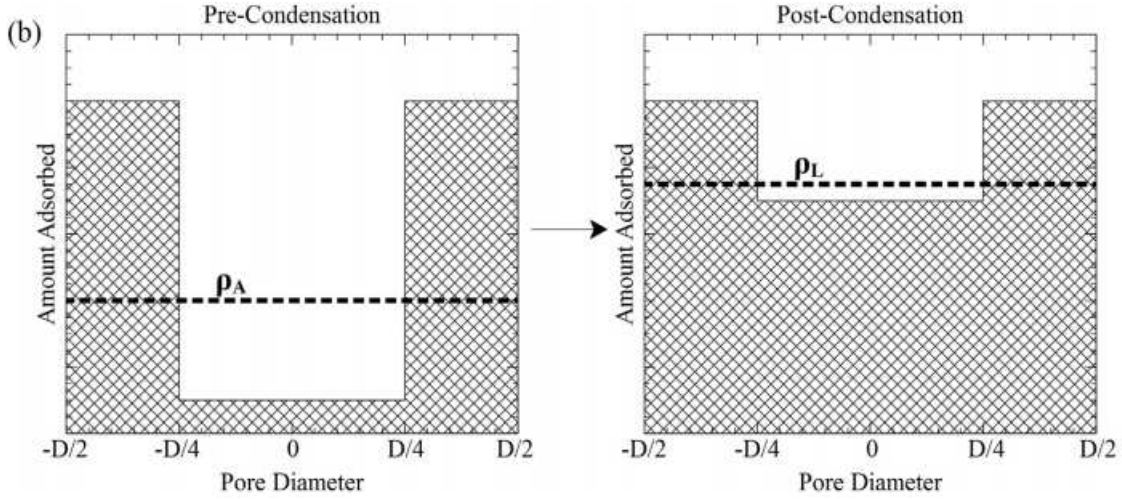

(b) Confined density represented as the number of moles of a given confined fluid phase filling a pore divided by the pore's total volume

Figure 2.1: Confined phases and densities (Walton and Quirke 1989).

2.2 Adsorption Isotherm

Adsorption is the adhesion of molecules of gas to a solid surface. When this occurs, a layer of film is formed on the surface referred to as the adsorbate as shown in Figure 2.2. The solid surface here is referred to as the adsorbent. Adsorption is almost always explained through adsorption isotherms, the amount of adsorbate on the adsorbent in terms of pressure at a constant temperature.

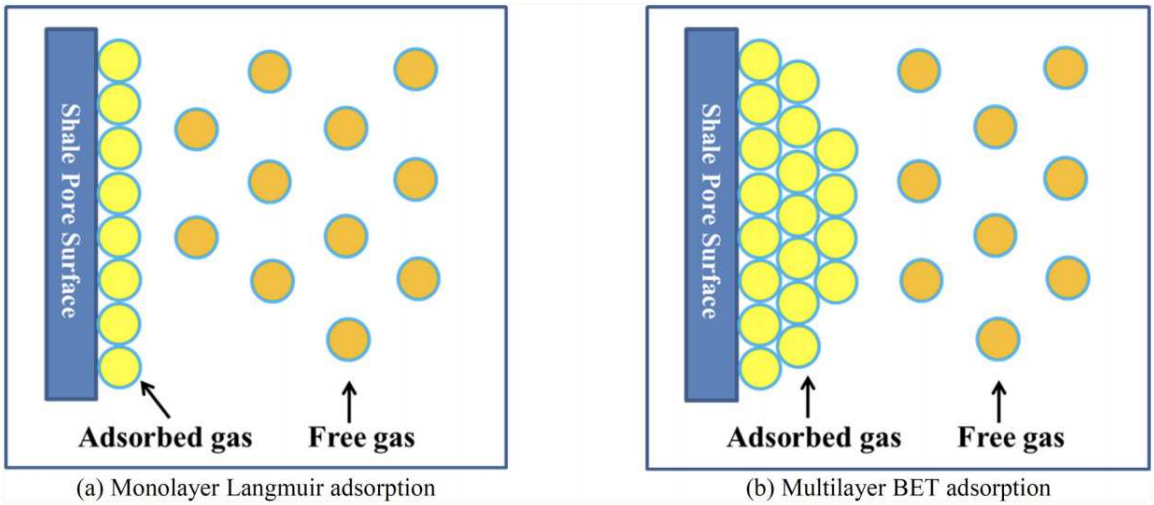

Figure 2.2: Illustration for Langmuir and BET adsorption (Sing and Williams 2012).

The most widely used isotherm used to describe adsorption is the Langmuir isotherm model which applies to gases adsorbed to solid surfaces and is derived based on statistical thermodynamics. The model assumes:

- No phase transition.
- A homogenous surface with no interaction between adsorbed molecules.
- Adsorption occurs equally throughout the surface and only one molecule can be accommodated at each adsorption site.
- Only one layer is formed.

Other isotherms such as the BET (Brunauer-Emmett-Teller) theory account for multi-layer adsorption since monolayer adsorption is a very idealized concept that does not exist in nature. BET is used in nitrogen gas adsorption studies to measure pore size distribution, pore volume and surface area of unconventional reservoir core samples. It can also be used to characterize the pore structure in conjunction with carbon dioxide adsorption. BET is essentially an enhanced version of the Langmuir model with the following additional assumptions:

- The uppermost layer is in equilibrium with the vapor phase.
- Heat adsorption occurs between the first and the overlaying layer.
- Adsorption occurs in infinite layers.

Capillary condensation data is derived from adsorption isotherms that correlate the amount of fluid adsorbed on a surface to the operating bulk pressure and temperature. In the mesopore scale, adsorption isotherms tend to be steep vertical curves signifying the rapid filling of pores associated with capillary condensation.

Using transparent nano-fluidic chips to observe the effect of pore size on vapor pressure, Parsa et al. (2015) concluded that fluid phase behavior under confinement differs greatly from that of bulk. Unlike conventional reservoirs, shale reservoirs have both free and adsorbed gas. The adsorbed gas mainly resides in small kerogen pores (lengths less than 100 nm) while free gas is mainly in inorganic matrix pores and microfractures. The Langmuir isotherms are usually used as the kinetic model to describe the adsorption/desorption of shale gas. However, these isotherms are used for single component systems and have to be modified to handle multi-components. The Langmuir isotherm for a single component is:

$$V_a = \frac{V_L p}{p_L + p} \tag{2.1}$$

where V_a denotes the amount of adsorbed gas at pressure p; V_L is the maximum adsorption capacity at a given temperature; and p_L is the Langmuir pressure at which the adsorbed gas

content is $0.5V_L$. Additionally, the Langmuir's model assumes adsorption as a single molecule layer whereas in shale, adsorption is multi-layered due to the small size and wettability of nanopores in the kerogen (Li et al. 2013).

Capillary condensation behavior is characterized when vapor condensation occurs below the vapor saturation pressure of the fluid due to confinement. Gelb et al. (1999) concluded that as pore size decreases, capillary condensation occurs at pressures lower than dew point pressure. The International Union of Pure and Applied Chemistry (IUPAC) has classified six types of adsorption isotherms. The isotherm for capillary condensation is represented by the type IV isotherm and the Langmuir isotherm is of type I as illustrated in Figure 2.3 below.

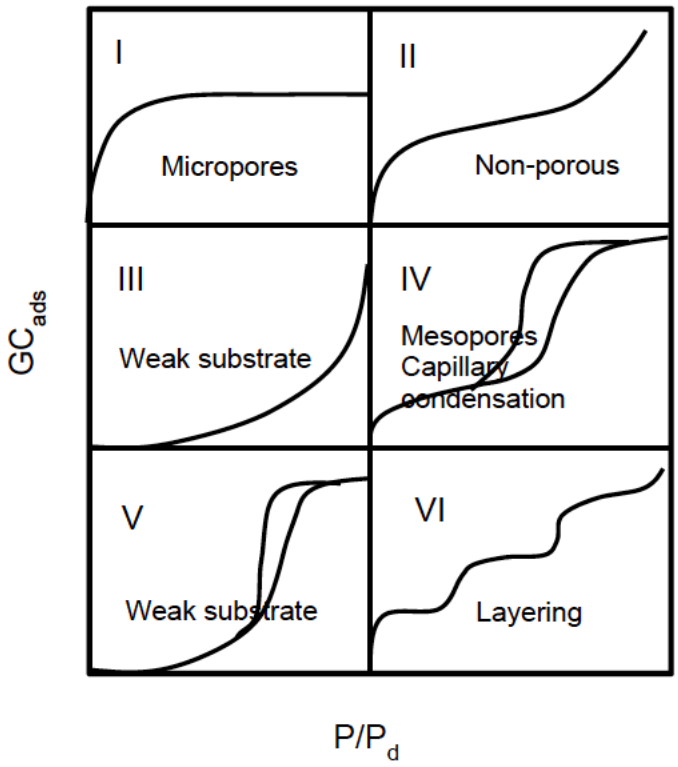

Figure 2.3: Classified sorption isotherms as defined by IUPAC (Thommes et al. 2015).

Capillary condensation behavior is characterized by the hysteresis of the adsorption-desorption isotherm due to its multilayer adsorption nature. The shape of the loop depends

on pore shape. Multilayer adsorption of the vapor phase into the rock matrix continues until the pore space is filled with condensed liquid. Chen et al. (2012) demonstrated this concept by experimentally proving the existence of capillary condensation within the nanopores of their shale samples. They concluded that capillary condensation does occur in the reservoir depending on pore size and the reservoir's thermodynamic conditions. It is important to note that both gas and liquid may co-exist in the reservoir even if only gas is produced. Acoustic properties of the same formation often change over time during the lifecycle of the reservoir. This is attributed to the change in phase behavior of the reservoir fluids. However, the effects of this phase change on the acoustic properties are not fully understood.

To reiterate, capillary condensation is the phase transition of fluid into a condensed phase due to confinement. This transition manifests itself as a multilayer adsorption in the tightest section of the nanopores. Phase transition can occur up to the critical temperature point T_C, above which only a single supercritical phase exists (assuming a pure fluid phase in bulk). When dealing with a confined fluid, the condensed phase and the lighter adsorbed phase can be distinguished only up to the pore/confined critical temperature T_{CP}, which is lower than T_C (bulk). In fluids showing hysteresis behavior in their adsorption isotherms, there exists a temperature past which no hysteresis occurs and is defined as critical hysteresis temperature T_h.

Synthetic nano-porous media are used in experimental studies to help improve the understanding of the physics governing capillary condensation. These materials are homogeneous in nature with disconnected pores and uniform pore geometry. The most commonly used synthetic nano-porous adsorbents are nano-porous silicas MCM-41 and SBA-15. They both contain hexagonally ordered cylindrical pores made of silicon dioxide and can be made with varying pore sizes. Figure 2.4 illustrates the temperature dependence on a hysteresis loop. T_h is less than T_{CP}, and a decrease in temperature below T_h results in the expansion of the hysteresis loop (Morishige and Nakamura, 2004). This is also supported by the experimental work of Morishige et al. (2014) who observed capillary condensation at a wider range of tem-

peratures from below T_h to T_{CP} for nitrogen, oxygen, argon, ethylene and carbon dioxide in MCM-41. This was also confirmed by Tanchoux et al. (2004) who observed that T_h decreases with pore size.

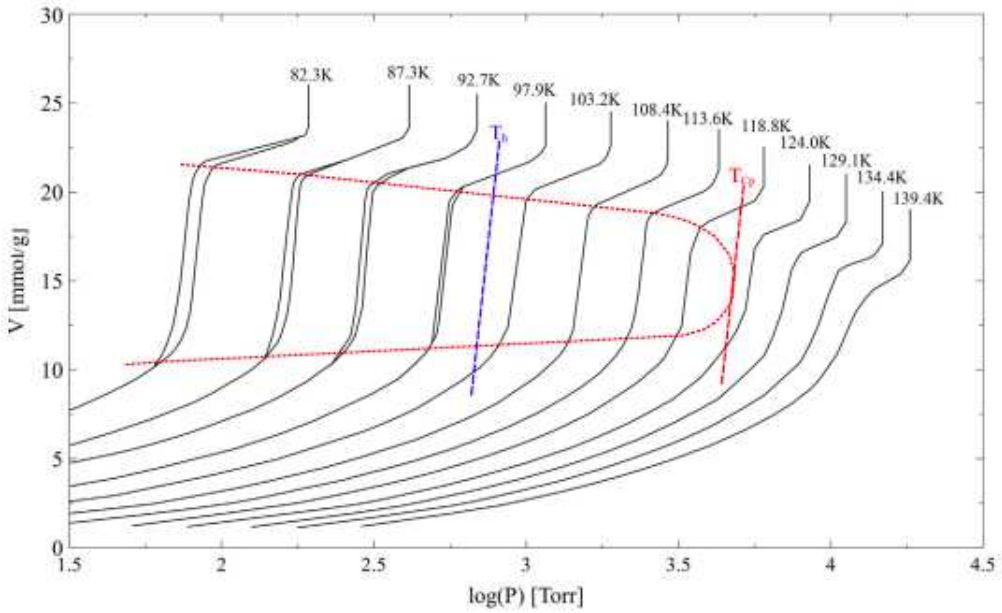

Figure 2.4: Temperature dependence on hysteresis loop (Morishige and Nakamura 2004).

Gor et al. (2013) compared capillary condensation adsorption isotherms of n-pentane in MCM-41 and SBA-15 to experimental and theoretical strain isotherms. Their strain isotherms for adsorbents during capillary condensation of (a) a wetting fluid and (b) a non-wetting fluid are shown in Figure 2.5. These isotherms are plots of relative pressure versus strain and are produced by a small angle X-ray scattering at constant temperature. After comparing theoretical and experimental isotherms and finding discrepancies, Gor et al. (2013) observed that capillary condensation changed the elastic properties of SBA-15 but not MCM-41.

They explained this difference to the presence of micropores in SBA-15 although their SBA-15 sample had more than twice the pore diameter of their MCM-41 sample. Therefore, their findings were not conclusive on exactly how pore size affects pore wall elasticity during capillary condensation. Gunther et al. (2008) shed light on this issue by using small angle X-

ray diffraction measurements to show that increased adsorption before capillary condensation causes the pores to expand while capillary condensation causes the pores to contract. This demonstrates how changes in pore diameter due to adsorption could affect the onset of capillary condensation.

These strain isotherms can also be utilized to show the pressures of the fluid within the pores since the strain of the absorbent is correlated to the pressure of the enclosed fluid. The findings by Gor et al. (2013) also demonstrate that adsorbed fluid layers before capillary condensation have a positive pressure (causing a positive strain or expansion of the adsorbent). Alternatively, the condensed phase has a negative pressure (in tension or contraction of the adsorbent). In their simulation studies, Long et al. (2013) confirmed this phenomenon and found that pressure in the condensed phase was always negative in pores with size greater than 5 molecular diameters of the confined fluid.

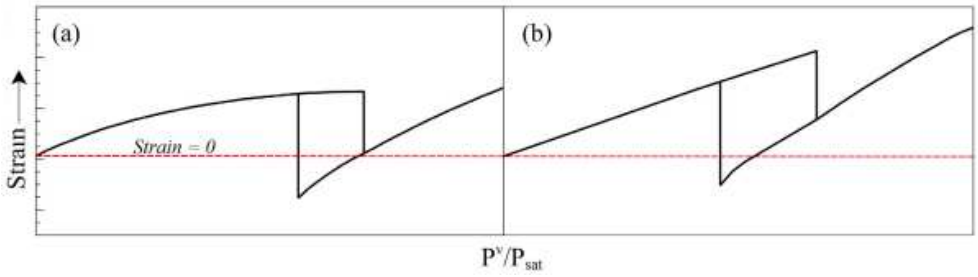

Figure 2.5: Strain isotherms for adsorbents during capillary condensation of a (a) wetting fluid and (b) a non-wetting fluid (Gor et al. 2013).

Using Pulsed Field Gradient Nuclear Magnetic Resonance (PFG NMR), Naumov et al. (2008) showed that for cyclohexane in Vycor glass, the hysteresis of the adsorption isotherm occurs in conjunction with hysteresis of the self-diffusivities. Self-diffusivity here refers to the random microscopic movement of fluid molecules as the result of their thermal energy exclusively. They attributed this self-diffusivity hysteresis to the density differential of the pore-filling fluid during adsorption and desorption. Due to the pore-blocking effects that happen when evaporation occurs through cavitation, self-diffusivity was lower during desorption. Cavitation is the formation of vapor cavities in liquid as a consequence of forces acting on the liquid and is dependent on pore geometry as well. This self-diffusivity hys-

teresis loop behavior compared to that of an adsorption isotherm hysteresis is presented in Figure 2.6.

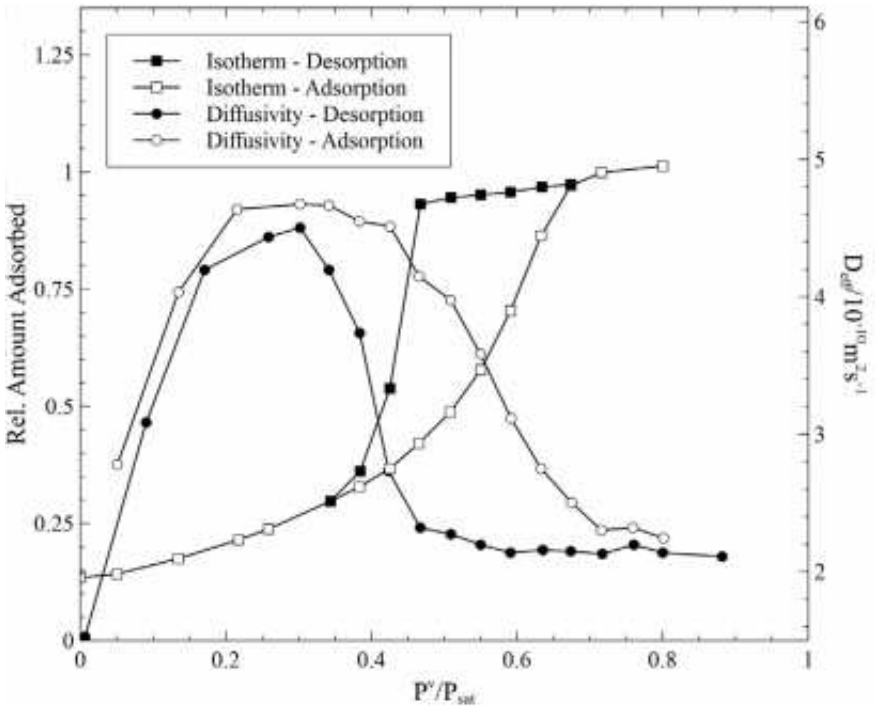

Figure 2.6: Self-diffusivity hysteresis compared to that in adsorption isotherm (Naumov et al. 2008).

Understanding capillary condensation is important for hydrocarbon-in-place estimation. Chen et al. (2013) incorporated adsorption isotherms exhibiting condensation resulting in their gas in place estimations to increase by six-folds. The impact of different compositions on increasing the total hydrocarbon in place estimation is shown in Figure 2.7. The compositions of the mixtures with their corresponding dew point are also shown. We could see for instance that the pressure needed for capillary condensation to occur for mixture M1 is more than six times higher than that of mixture M6. This means that the real pressure for M1 in the formation is also more than six times higher than that of M6 which explains the increase in total hydrocarbon estimation.

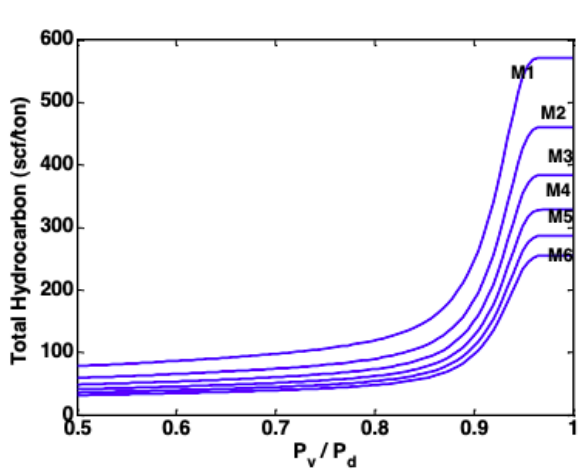

(a) Change in hydrocarbon in place depending on different compositions

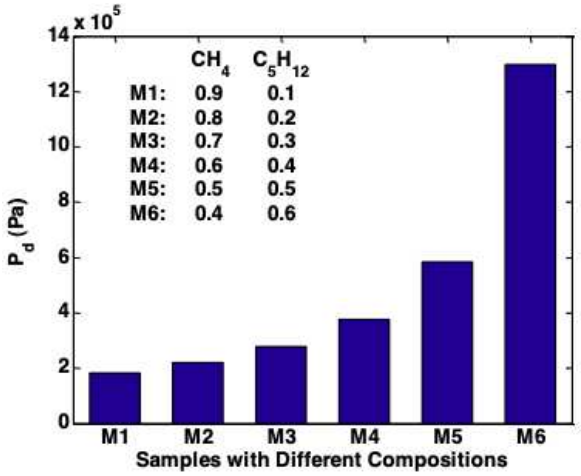

(b) Different compositions with their respective dew point pressures at 311 K

Figure 2.7: Effect of composition on reserve estimation due to capillary condensation in multiple component mixtures (Chen et al. 2013).

It is also worth noting that hydrocarbon in place estimation is very dependent on mean pore size as shown in Figure 2.8. In this case, mixture M5 was used and the different lines correspond to isotherm curves with 5, 10, 20, 40 and 100 nm pore size. We can see how capillary condensation occurs at a significantly lower pressure in smaller pores with the same composition.

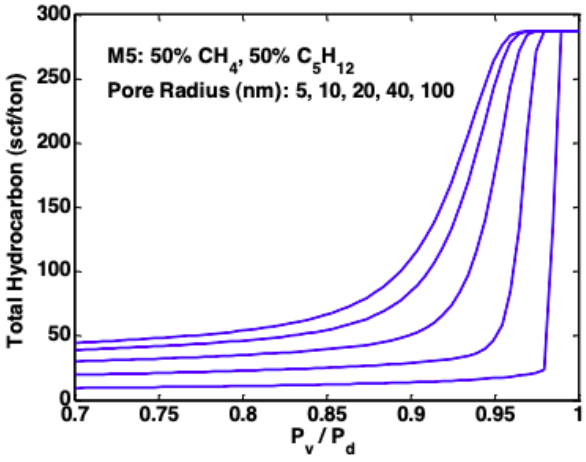

Figure 2.8: Hydrocarbon in place estimation dependence on pore size (Chen et al. 2013).

Finally, the new hydrocarbon in place estimates with those obtained using a traditional Langmuir model are compared in Figure 2.9. The blue line represents the estimation when capillary condensation is accounted for while the straight pink line represents the results from the traditional Langmuir model. It can be observed that capillary condensation occurs at a pressure lower than the dew point pressure and the hydrocarbon estimate is significantly higher.

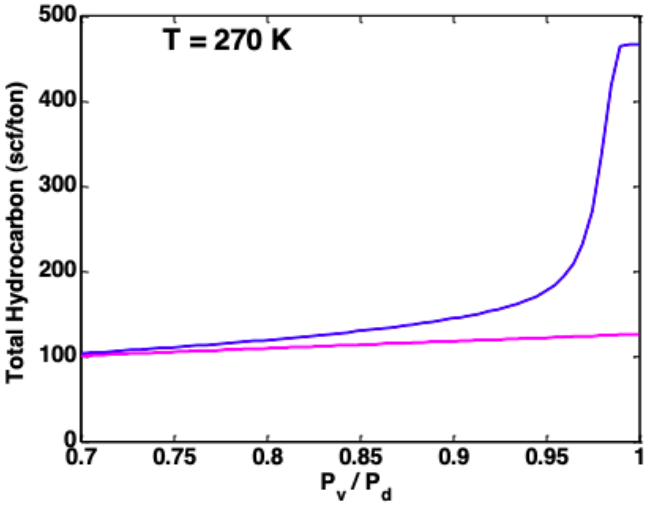

Figure 2.9: Comparing HCIP estimation of traditional Langmuir model with the new modified model accounting for capillary condensation (Chen et al. 2013).

2.3 Phase Behavior Change

The physical behavior of fluids in confined space greatly differs from that in the bulk. The difference in behavior is attributed to capillary pressure. Typically in porous medium, a non-zero curvature of the gas-liquid interface results in pressure differences between phases which shifts thermodynamic properties such as phase composition, bubble and dew point pressures (Satik et al. 1995; Shapiro and Stenby 1997; Espósito et al. 2005; Sing and Williams 2012). This shift is even more dramatic at smaller pore sizes (Alharthy et al., 2013).

Due to the tight space and decreased distance between molecules within the nanopores, intermolecular forces are high and phase behavior becomes a function of not only fluid-fluid

interactions but also a function of fluid-pore wall interaction (Sandoval et al. 2016). These findings however, have all been theoretical and have not been determined experimentally due to the challenging nature of small pore size characterization and the lack of high resolution measurement tools required. Different methodologies have been applied in order to model this phase behavior with capillary pressure in tight confining pores. These methods include using different Monte Carlo iterations, Quench molecular dynamics, histogram reweighing method, Landau free energy method, Lattice modeling and density functional theory as discussed by (Li et al. 2014; Ma et al. 2016).

Capillary and adsorptive forces affect fluid densities, critical properties, interfacial tensions, saturation pressures and therefore phase behavior (Tarazona et al. 1987; Gelb et al. 1999; Sangwichien et al. 2002; Monson 2005; Li et al. 2014). It is important to note that capillary condensation data (not adsorption data) is what is missing for EOS parameterization when modeling the effects of capillary condensation. Adsorption, without transitioning phases, is better understood than capillary condensation. Adsorption-only data neglects the effect of surface forces and therefore may not be sufficient to understand capillary condensation.

Sandoval et al. (2016) developed a multi-component algorithm that is able to calculate phase envelopes in the presence of capillary pressure. It is used as tool to study the effect of capillary pressure on the phase envelope based on composition and capillary radius. They observed changes in saturation pressure due to capillary pressure. The findings of Sandoval et al. (2016) on how capillary condensation affects phase behavior are illustrated in Figure 2.10. The dashed line represents the modified phase envelopes due to capillary pressure difference while the solid lines represent the normal envelopes in the figure. Three different C_1-C_4 composition mixtures were used in the feed. This shift is expected to be more significant when the pore size is very small. The reduced bubble point and dew point pressures often enhance hydrocarbon production from these nanopores (Ambrose et al. 2010; Didar and Akkutlu 2013; Nojabaei et al. 2013).

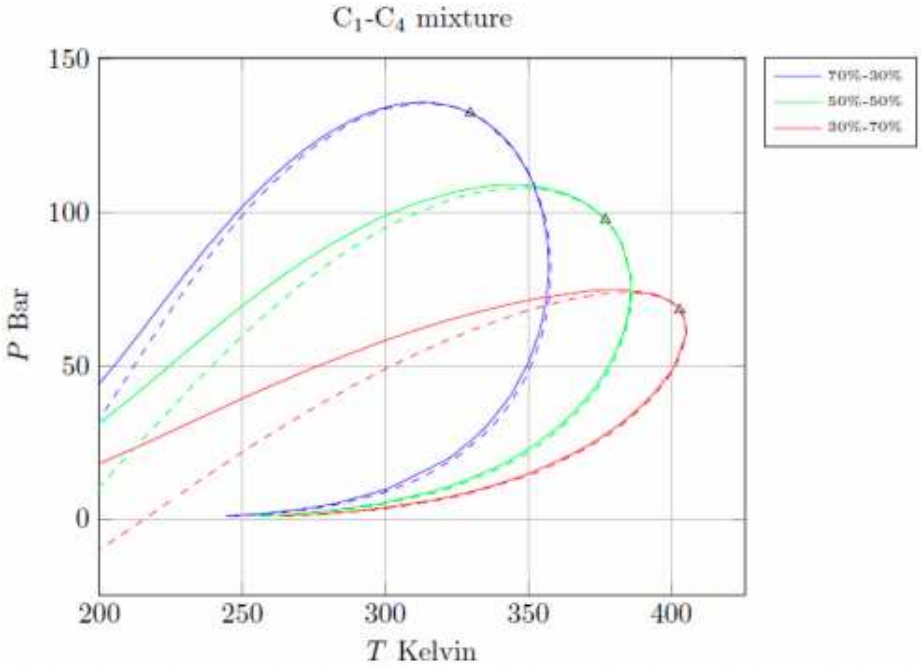

Figure 2.10: Phase envelope at different feed compositions with (dashed line) and without capillary condensation (solid line) (Sandoval et al. 2016).

Alharthy et al. (2013) constructed phase diagrams using new correlations to shift the critical properties of components in the nano scale. The difference in the confined and unconfined phase envelopes of dry gas using associated correlations is shown in Figure 2.11. They used the Peng-Robinson EOS to generate the unconfined pore phase envelope. The confined envelope used the new shifted critical properties that accounts for pore confinement effects. Once again, we see that the effect of confinement is the shrinking of the phase envelope.

Using a coupled geomechanical and pore confinement model, Xiong et al. (2014) observed that increasing effective stress further increased the effect of confinement on suppressing the bubble point pressure for Bakken oil as shown in Figure 2.12. Without accounting for confinement, bubble point pressure remains constant with changes to effective stress. Whereas when pore confinement is taken into account, the bubble point decreases with increased effective stress as a result of smaller pore throat size and larger capillary pressure.

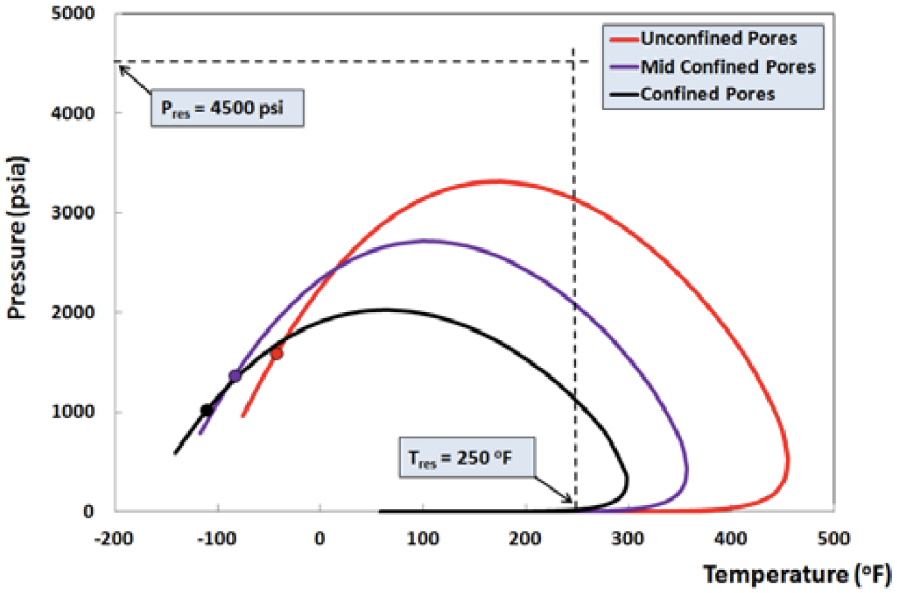

Figure 2.11: Phase envelope changes due to confinement (Alharthy et al. 2013).

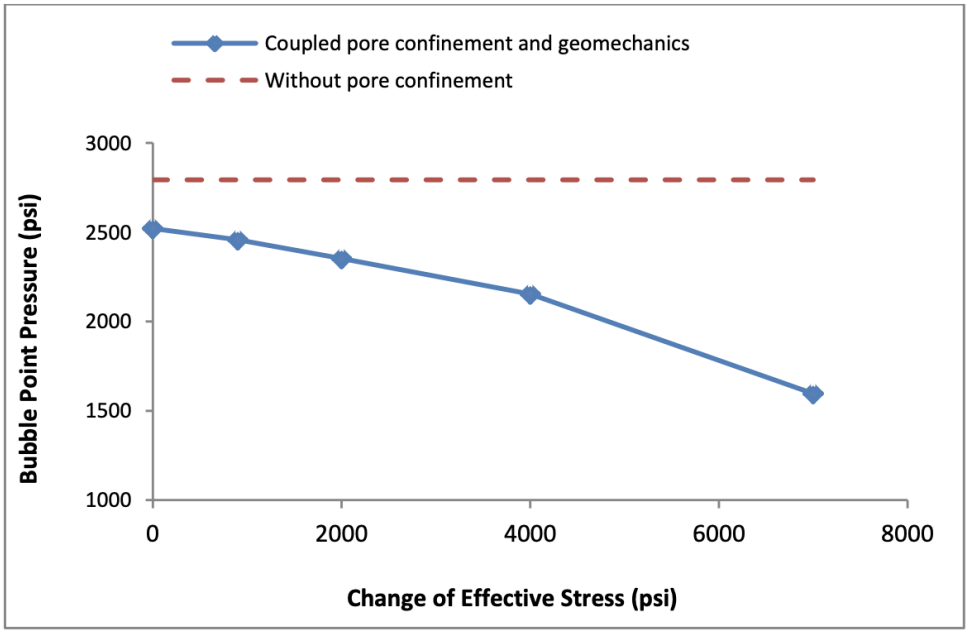

Figure 2.12: Bubble point suppression effect due to confinement (Xiong et al. 2014).

Teklu et al. (2014) modified their conventional vapor/liquid equilibrium calculations to account for capillary pressure and shift in the critical properties in nanopores to study the phase behavior in unconventional reservoirs. Figure 2.13 shows the phase envelope shift when accounting for confinement. The solid lines represent the shift when accounting for only shifts in critical properties, whereas the dashed lines represent the combined effect of critical properties shift and capillary pressure. They observed that the bubble point dramatically decreases when accounting for both capillary pressure and shifted critical properties.

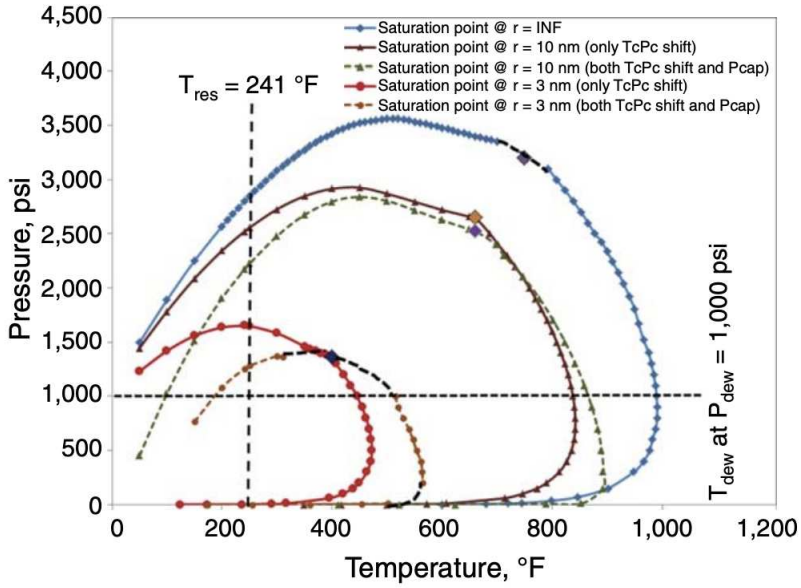

Figure 2.13: Shift in phase envelope due to confinement by accounting for capillary pressure and the shift in the fluid's critical properties (Teklu et al. 2014).

2.4 Effect of Capillary Condensation on Mass Transport

It is important to note that in reservoirs with low permeability, wells are usually in transient flow for a very long time which is another reason why getting an accurate estimate of hydrocarbon in place is important. Ambrose et al. (2010) also observed that in reservoirs where there is a significant sorbed-phase component, the hydrocarbon in place has been often over-estimated due to a lack of material and voidage replacement ratio in the gas-in-place calculations. Many studies have focused on fluid transport in nanopores and have been used

to understand the complex flow of gas in nanopores (Roy et al. 2003; Javadpour et al. 2007; Civan et al. 2011; Fathi and Akkutlu 2011; Gouth et al. 2013; Rahmanian et al. 2012; Umeda et al. 2014; Zhang et al. 2014).

As gas condenses in the tighter sections of the rock, the heavier liquid component will constrict the size of the pore throat accessible to gas flow thereby reducing the flow of gas across it. This phenomenon, however, has not been experimentally verified.

Capillary condensation in the pore throat affects fluid flow and transport at the pore scale due to the relatively low mobility of the condensed fluid. Bui et al. (2016) suggested that due to capillary condensation, the transport of the fluid in the nanopores involve the simultaneous evaporation and condensation at the gas-oil interface. Their numerical model showed that the flow of gas along the pore is significantly reduced due to capillary condensation because of the higher mobility of the liquid phase inside the pore throat.

2.5 Impact of Rock-Fluid Interaction on Acoustic Properties

The acquisition of rock mechanical properties is often achieved by seismic measurements. The interpretation of seismic data for unconventional reservoir is rather more complex than that for conventional reservoir because of the new fluids introduced to the formation during hydraulic fracturing. During hydraulic fracturing a larger volume of water is injected to formation, typically from 1000 to 5000 scf/ft. The injected fluids interact with not only formation fluids but also with the sale matrix alternating the mechanical behavior of rock affecting it deformation and failure as well as hydrocarbon recovery.

Due to the small grain size and the strong surface electrochemical properties of shale grains, the effect of fluid on mechanical properties and deformation of shales is more significant than for unconventional reservoir. This explains why these properties are significantly changed when different fluids are introduced. Acoustic logs measure the mechanical and acoustic properties of rocks at approximately 20 KHz. Most measurements are carried out at ultrasonic frequencies (>>1 MHz), while low frequency (static) properties that may be relevant to the fracturing process. An interpretation process is used to obtain static proper-

ties from dynamic log data. It is, therefore, important to extrapolate mechanical properties from sonic data. Hence, the interpretation of acoustic data needs the understanding of the factors that control the propagation of acoustic waves in shales.

Contrasted to the low strain-rate experiments of static measurement in geomechanics laboratory, dynamic data from acoustic measurement depend on several factors that affect the propagation of energy. When acoustic waves propagate through a porous medium, the high frequency vibration of the transmitter creates the oscillatory motion of solid grain and the fluid in the pore space. Under rapidly oscillating deformations, the pore fluids do not have sufficient time to flow into low pressure regions and therefore the rock will act as if it is unrelaxed or undrained. This means that the medium will behave stiffer in the unrelaxed state resulting velocity dispersion (Winkler 1983; Murphy 1984). On the other hand, if time is sufficient for fluid pressure to reach equilibrium, then the relaxed properties are measured as in with low frequency measurements. The behavior of porous media under high frequency deformation depends on not only its fluid and rock properties such as mechanical properties, porosity, permeability, saturation, mineralogy, pore structures, density and viscosity but also on external parameters such as stress, temperature, and pore pressure. More importantly for shale, the electrochemical characteristics of the fluids inside the pore space have a considerable effect.

Porosity, permeability, and fluid saturation are the most important petrophysical properties controlling the acoustic behavior of rocks. Attenuations and acoustic velocities are influenced by both porosity and permeability. Increasing porosity reduces the bulk density of rock and results in an increase in acoustic velocities. Permeability determines the mobility of the fluid in the pore space; hence it controls velocity. Permeability is often promotional to porosity and has the similar effect on velocities.

Dry velocities and attenuations are significantly different from saturated velocities in all rocks. In liquid saturated rocks, compressional and shear velocities and attenuations strongly depend on frequency. Velocities are commonly observed to be higher in dry rocks than they

are in partially-saturated rocks. With the presence of clay, the considerable variation in velocity at very low saturations was explained by Clark et al. (1980) as the result of the dehydration and stiffening of clay minerals in contact with the grains. Absorbed water reduces the surface free energy of the rock minerals and decreases the free energy resulting in lower elastic modulus and lower velocities. Heterogeneity and anisotropy of rocks also have a significant effect on the measured velocities and attenuations. The elastic anisotropy decreases with increasing stress and is dominated by the combined effects of micro-cracks and mineral grain orientation.

In shale, the bedding planes and the orientation of cracks control the anisotropy. The anisotropy of acoustic properties of rock is the result of elastic anisotropy and permeability anisotropy. In addition, pore geometry and grain size also affect attenuation and acoustic velocities. Attenuation typically increases with the decrease of grain size, especially for sand. There are two principal sources of dissipation from fluids in rocks. The first source is the hydrodynamic effect associated with bulk fluid flow depending on the crack and pore geometry. The other source is an effect associated with fluids and depends on the chemistry of the adsorbate and the host.

Along with petrophysical properties, the external parameters controlling the mechanical properties of rocks are the effective pressure, confining stress, pore pressure, temperature, strain, and strain rate. Acoustic velocities increase significantly with increasing stress because of the closure of cracks and pore space in shale. The considerable in-crease in compressional velocity in fully saturated rocks is observed, but only a small increase is observed in shear velocity. The effect of confining stress on velocities is a result the deformation of micro-cracks and loose grain contacts, which are the most compliant parts of the pore space. Hence, confining stress increases the stiffness of the rock, which influences its effective bulk and shear moduli and is responsible for the higher velocities observed. The dependence on pore pressure is due to the same reasons as the pressure dependence of velocity, which is the closure of micro-cracks in the rock. The closure of cracks reduces the permeability of the

rock and hence reducing the mobility of fluid in the medium.

For dry rocks, the rate of change with confining pressure is greater than for saturated rocks. Pore pressure prevents the closing of cracks and grain contacts, thus leading to lower effective moduli and velocities under the same confining. Peselnick and Outerbridge (1961), Winkler and Nur (1979) and Tittmann et al. (1980) showed that attenuation in rocks generally increases with increasing strains above a certain critical strain value. In addition, the effect of strain amplitude becomes less pronounced as the effective stress on the rock is increased Winkler and Nur (1979). As pressure increases, the equilibrium separation distance between the asperities decreases as a result of deformation and the fluid at the grain contacts is squeezed out to the bulk pore space (Palmer and Traviolia 1980; Mavko 1979; Murphy et al. 1986; Tutuncu and Sharma 1992). The rate of deformation, strain rate, also has a significant effect on the mechanical and acoustic response of shale. Shale behaves stiffer under higher rate of deformation.

The dependence of temperature on shale mechanical properties in saturated rocks has the contribution of the temperature dependence of viscosity. A reduction in viscosity reduces the rigidity of the rock and correspondingly its velocities. Temperature also strongly affects the electrochemical properties of the contact region between fluid and rock grains, hence, affecting the deformation and failure characteristic of shale.

The reduction of acoustic velocities when fluid is introduced to the pore space is originally explained as the result of bulk density alteration. However, when the same rock sample is saturated with fluids of similar densities and viscosities, the variations observed in velocities and attenuations can no longer be explained by the density difference (Spencer 1981; King 1965). Such velocity decreases because of the reduction in the stiffness of the rock matrix due to surface interactions between the rock and the pore fluid (Murphy et al. 1984; Tittmann et al. 1984; Tutuncu and Sharma 1992). There is a large difference in the effect of polar fluids and non-polar fluids. Tutuncu (1992) showed that fluids with the same density and viscosity have different effects on acoustic properties of rocks due to the difference in chemical,

electrochemical and dielectric properties.

Bui and Tutuncu (2015) used the grain contact model explained to model the effect of capillary condensation on the acoustic and geomechanical properties of shale. To account for the effect of stress, grain deformation and separation distance between two grains are calculated. It was observed that separation distance between grains decreased under higher external stress thereby reducing the mobility of the enclosed fluid. This results in higher gap stiffness and higher acoustic wave velocities.

CHAPTER 3

WAVE PROPAGATION IN TIGHT FORMATION AND MODEL DEVELOPMENT

In this chapter, the fundamentals of wave propagation in tight formations is discussed. A theoretical model was developed to evaluate changes in acoustic and mechanical properties of a tight sample with changes in stress, frequency, temperature, pressure and condensation. The factors that affect change in wave propagation are also discussed.

3.1 Acoustic Velocity Modeling

Acoustic waves are elastic waves that travel through a medium and are reflected or refracted at interfaces where seismic velocities or bulk densities change. These acoustic/seismic waves are affected by rock density and fluid saturation. Denser rocks typically have faster compressive velocity. When an ultrasonic wave encounters obstacles such as fractures and cracks, ultrasonic attenuation will occur which is signified by a decrease in wave velocity or amplitude. Factors such as porosity, elasticity modulus and stress affect the transmission of these waves. Acoustic wave velocity also decreases when the saturating fluid (oil or water) is replaced by gas. The two main wave types typically used in geomechanical laboratory investigations are primary (P) and secondary (S) waves.

P-waves are compressive waves that travel in a straight line through a medium and are the first to arrive. Primary wave velocity can be calculated from:

$$V_p = \sqrt{\frac{K + \frac{4}{3}G}{\rho_b}} = \sqrt{\frac{\lambda + 2G}{\rho_b}} \tag{3.1}$$

where K is the bulk modulus; ρ_b is bulk density; G is the shear modulus; and λ is Lame's coefficient.

The bulk modulus K relates volumetric strain to average stress and can be calculated from:

$$K = \lambda + \frac{2}{3}G \tag{3.2}$$

Young's Modulus (E) is another important modulus which is the ratio of applied stress to corresponding strain in same direction. Poisson's Ratio (ν) is the ratio of lateral expansion to axial strain.

S-waves are shear waves that oscillate the rock grains in the direction perpendicular to the direction of wave propagation. Secondary wave velocity can be calculated from:

$$V_s = \sqrt{\frac{G}{\rho_b}} \tag{3.3}$$

Shear waves are always slower than primary waves. Studying changes in shear wave velocities can shed light on rock properties such as fracture density and orientation. Shear wave travel time data can be used to estimate the mechanical properties of the rock using sonic and seismic logs. These compressional/acoustic waves are heavily influenced by fluid saturation. Petrophysicists often use the ratio of compressional to shear wave velocity V_p/V_s to identify fluid types. As hydrocarbon saturation increases, compressional wave velocity decreases while shear wave velocity increases which makes the V_p/V_s change even more pronounced.

Seismic methods are used in reservoir engineering to predict and evaluate fluid producing zones, map porosity and permeability, detect fractures, faults and abnormal stress zones as well as monitor the effects of production/injection operations. This can be done by relating acoustic impedance from the seismic data to petrophysical properties such as saturation, porosity and permeability. This conversion can only be made possible by establishing a methodology that enables the accurate extrapolation of acoustic and mechanical properties from one to another.

Wang et al. (2016) found that compressional velocities were greatly reduced by carbon dioxide flooding in conventional rocks. This was especially noticeable at high pore pressures. The velocity decrease was dependent mainly on temperature, effective pressure and porosity.

Shear wave velocities were less affected by carbon dioxide flooding. Their aim was to enhance EOR monitoring capabilities in carbon dioxide injection operations by mapping the changes in seismic velocities. This is explained by the fact that injected carbon dioxide increases compressibility of the rock and alters its density based on pore pressure. Increased pore pressure increases carbon dioxide density as well as keeps pores and cracks open nullifying some of the effects of confining pressure. These changes affect wave propagation through the rocks. The relationship between compressional wave velocity and pressure at different temperatures is shown in Figure 3.1.

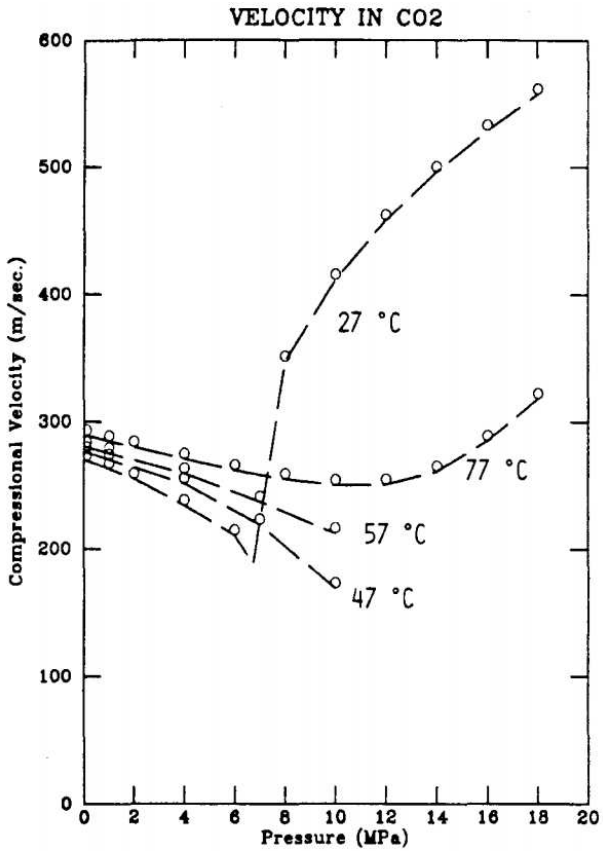

Figure 3.1: Compressional wave velocity as a function of pressure and temperature (Wang et al. 2016).

Wang et al. (2016) observed that velocity is slow and a weak function of pressure when temperature is above the critical temperature. However, velocity is very much dependent on

phase behavior at temperatures below the critical temperature. When carbon dioxide is in the liquid phase, velocity increases significantly with increased pore pressure.

Wang et al. (2016) concluded that carbon dioxide flooding reduced compressional wave velocity by 4-11% in well-consolidated sandstones and by more than 25% in unconsolidated sandstones as shown in Figure 3.2 for Berea Sandstone 6 with 21% porosity. Another important observation they made was that increased porosity decreased the carbon dioxide flooding effect in well-consolidated sandstones due to the increased fluid content and density of the rock.

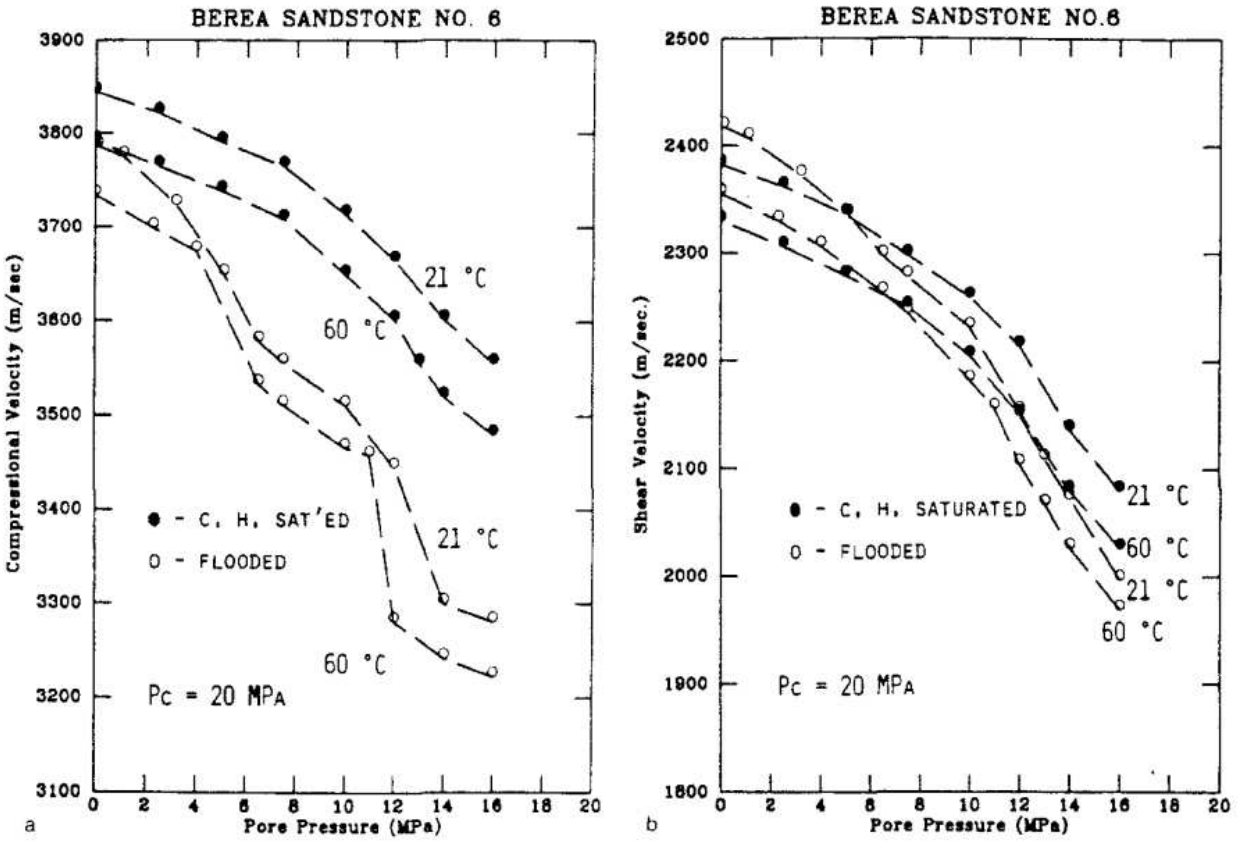

Figure 3.2: Compressional and shear wave velocity behavior of the Berea Sandstone 6 (Wang et al. 2016).

3.2 Grain Contact Model

Fluid-rock interaction at the grain contacts is an important variable that affects the thickness of the inter-granular pore and is responsible for velocity dispersion and attenuation. Interpretation of ultrasonic velocity readings ,compressional and shear, can also give us insight into the rock's mechanical properties such as dynamic Young's Modulus and Poisson's Ratio. Shear wave interpretation can also help in assessing the anisotropy of the core sample. When combined with bulk density data, acoustic velocity can provide us with the formation's dynamic moduli. However, for this to happen, it is critical to understand the relationship between dynamic and static moduli, rock strength and rock-fluid interaction. As condensation occurs, the smaller pores are filled with liquid whereas the larger pores are filled with gas. An illustration of the porous media in shales is shown in Figure 3.3.

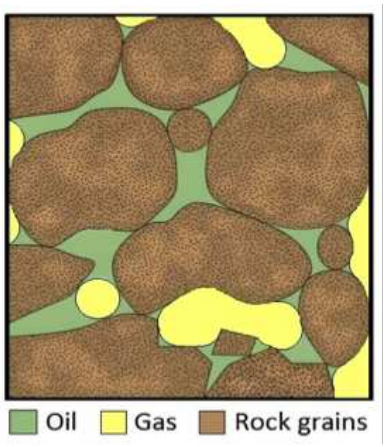

Figure 3.3: Schematic illustration of porous media in shale with condensation. Gas is condensed into liquid in the smaller pores while gas remains in the larger pores (Bui et al. 2016).

The simplified grain model helps us better understand the intermolecular surface forces at the nanoscale level, which is important to interpret the effects of these forces on the mechanical properties of the rock. Accounting these forces can help to better model the effects of stress, pressure, temperature and frequency on the acoustic properties of the rock. The effect of stress is calculated from the separation distance between two grains. This distance is decreased under higher external stress thus reducing the enclosed fluid's mobility.

This results in higher gap stiffness and higher wave velocities. These acoustic properties are frequency-dependent and are a function of the speed that the fluid can leave the contact region. It is reported that high frequency wave propagation is influenced by scattering and fluid-solid interactions at the grain contact region (Spencer 1981; Murphy 1982; Winkler 1983; Murphy 1984; Winkler 1985; Tutuncu 1992). The equilibrium separation distance between the grains decreases as more external stress applied on the grains (Mavko 1979; Palmer and Traviolia 1980; Murphy et al. 1986; Tutuncu and Sharma 1992).

In compressional waves, particle motion is in the direction of wave propagation whereas in shear waves, particle motion is perpendicular to the direction of wave propagation. The acoustic velocity of these waves is governed by stress, lithology, rock mechanics, pore fluid properties and saturation, temperature, diagenesis as well as the frequency and amplitude of the wave (Wyllie et al. 1956; Tutuncu et al. 1993; Liu et al. 1994).

Effective stress has a high impact on acoustic and mechanical properties. Eberhart-Phillips et al. (1989) investigated the effect of effective stress on acoustic velocity and developed a correlation to define effective stress as a function of velocity. They developed this equation using a number of medium to high permeability sandstone samples including tight sandstones. Bowers (1995) and Shapiro (2003) developed their own correlations. However, these equations are sometime not applicable for organic-rich shale formations since they do not take into account TOC (Total Organic Carbon), fluid composition or formation lamination orientation. Alqahtani (2015) developed a correlation describing the dependence of compressional velocity on stress, rock composition, TOC, rock lamination as well as fluid composition using the Eagle Ford Shale data.

In this study, the grain contact model is used to evaluate the effect of capillary condensation on the mechanical properties of the rock. The model helps in explaining the effect of stress, frequency, pressure and temperature on the geomechanical properties of the rock. The porous medium is modeled as a number of grains in contact with each other. These spherical grains are elastic and exhibit deformation at their contact areas. At reservoir conditions,

the gaps between the grains are filled with fluid (gas or oil depending on the thickness of the pore throat and the fluid properties). As shown in Figure 3.4, a small portion of the gap is filled with liquid for a small contact distance while the rest is filled with gas.

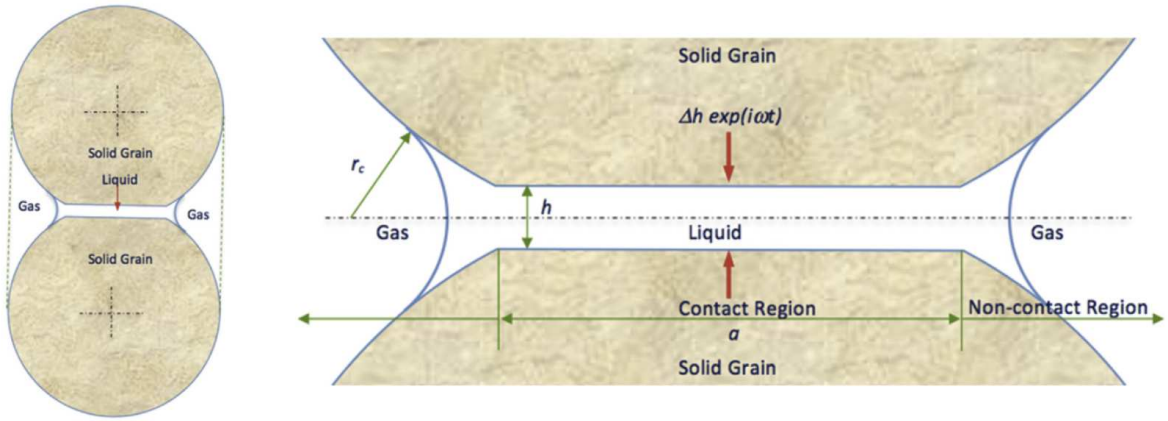

Figure 3.4: Oil and gas distribution at grain contact (Bui et al. 2016).

The effect of stress is incorporated by the calculation of grain deformation and the separation distance between two grains. The separation distance between grains is reduced under increased external stress, thereby reducing the mobility of the fluid in the gap. This results in higher gap stiffness and acoustic wave velocities. The speed at which the fluid can escape from the contact region dictates the frequency dependence of the acoustic properties of the formation (Spencer 1981; Murphy 1982, 1984; Winkler 1983, 1985; Tutuncu 1992; Tutuncu and Sharma 1992; Bui and Tutuncu 2014).

When subjected to high-frequency rapidly oscillating loads, the fluid does not have enough time to flow into low-pressure regions and the rock will act as if it is unrelaxed yielding in higher gap stiffness. Alternatively, if sufficient time is allowed for the fluid pressure to reach equilibrium, the rock is relaxed and behaves softer. The grain contact model uses separation distance to account for the effect of fluid type on the acoustic response of the fluid-grain system. When the same rock sample is saturated with a fluid of similar density and properties, significant variations are observed with velocity readings and attenuations

(King 1966; Spencer 1981; Tutuncu 1992). These variations are due to the change in surface forces and fluid-grain interactions (Tittmann et al. 1980; Murphy 1984; Tutuncu and Sharma 1992).

Before elaborating further on fluid-pore wall interactions, it is first important to introduce some surface chemistry fundamentals that will be used in explaining contact behavior.

- Disjoining pressure is the pressure dependence of the interaction between two surfaces. Furthermore, it is the pressure due to the attractive forces between two surfaces divided by the area of the surfaces. It is seen as the sum of multiple intermolecular interactions including dispersion forces, electrostatic forces, structural effects of the fluid and adsorption. In the case of two parallel flat surfaces, the disjoining pressure can be calculated as the derivative of the Gibbs energy divided by the surface area.

- Gibbs free energy is a thermodynamic potential that is used to calculate the maximum reversible amount of work that can be performed by an isobaric/isothermal thermodynamic system.

In order to account for fluid-pore interactions, the pressure difference between the confined and bulk phases has to be taken into consideration in the form of capillary pressure or disjoining pressure. Prior to the occurrence of capillary condensation, disjoining pressure is the sole form of interfacial pressure between the adsorbed layers and the vapor phase occupying the pore. The multilayers of adsorbed fluid will eventually converge indicating the occurrence of capillary condensation once the adsorbed film reaches its limit of stability. This will cause the center of the pore to be filled with the condensed phase separating it from the bulk vapor at the pore throat with a meniscus.

Once an equilibrium is reached between the bulk vapor and the condensed fluid, capillary pressure can be defined as the difference in pressure across the separating meniscus. Even after capillary condensation takes place, there will still be layers of fluid adsorbed on the pore wall signifying that a disjoining pressure still exists. However, it now represents the pressure

difference between the condensed phase and the adsorbed layers. It is usually assumed to be negligible in comparison to capillary pressure in contact mechanics modeling.

The equation for capillary pressure is derived from the Young-Laplace equation and is shown in Equation 3.4 in the case of a cylindrical pore.

$$p_c = p_{nw} - p_w = \frac{2\gamma}{r_p}\cos\theta_c \tag{3.4}$$

where p_{nw} is the pressure of the non-wetting phase; p_w is the pressure of the wetting phase; γ is the interfacial tension between the two phases; θ_c is the contact angle of the meniscus with the pore wall and r_p is the pore radius.

3.3 Critical Radius Determination

Gas generally condenses into liquid if gas pressure is equal to or greater than its dew point pressure (which is lower than that of unconfined liquid as discussed above). The Kelvin equation, first derived in 1871, is used to determine if gas in the pores with a radius r will condense to liquid based on its pressure (Thomson 1871). To account for the effects on nanopores in the case of capillary condensation, the Young-Laplace equation is used in the vapor-liquid equilibria (VLE). Equation 3.5 is rearranged to obtain an equation for the critical pore radius at which condensation will occur.

$$r_c = -\frac{2\gamma V_L \cos\theta_c}{R_g T \ln(\frac{p_g}{p_d})} \tag{3.5}$$

where R_g is the universal gas constant; p_g is gas pressure; p_d is dew point/saturation pressure and V_{LM} is the liquid molar volume.

It can be concluded from the Equation 3.5 that at pressure p_g, smaller gaps with interfacial radii smaller than the critical radius are filled with liquid while the larger ones are filled with gas. Hence, by changing the pressure of the fluid, we can cause certain pore sizes to condense. The diameter of the condensed pore can be determined form the equation above while the volume of the condensed pore can be determined by using acoustic correlations developed by Bui and Tutuncu (2015). Using this concept, pore size characterization of the sample can

be made possible.

This equation has been extensively used in both theoretical and experimental modeling to be able to describe capillary condensation mathematically. In addition to predicting the occurrence of capillary condensation, it can also be used in the evaluation of pore size, pore size distribution, the thickness of the adsorbed layers and to analyze the forces that are exerted on the adsorbent by condensates. However, there are some limitations with the Kelvin equation:

- The Kelvin equation is recommended for single component systems.
- It assumes an incompressible liquid phase and an ideal vapor phase in large pore spaces.
- The equation is used with the assumption that surface tension and molar density are not dependent on pore radius.
- It does not account for adsorbed phases or the fluid-pore wall forces that causes them.
- It has also been determined that the accuracy of the Kelvin equation is reduced when the interfacial radius is smaller than 7.5 nm (Walton and Quirke, 1989). The discrepancy between capillary pressure obtained from GCMC (Grand Canonical Monte Carlo) simulation results, experimental data. These limitations are shown in Figure 3.5.
- The accuracy of the equation when used in hysteresis isotherms is based on whether the true equilibrium branch is selected in the calculations.

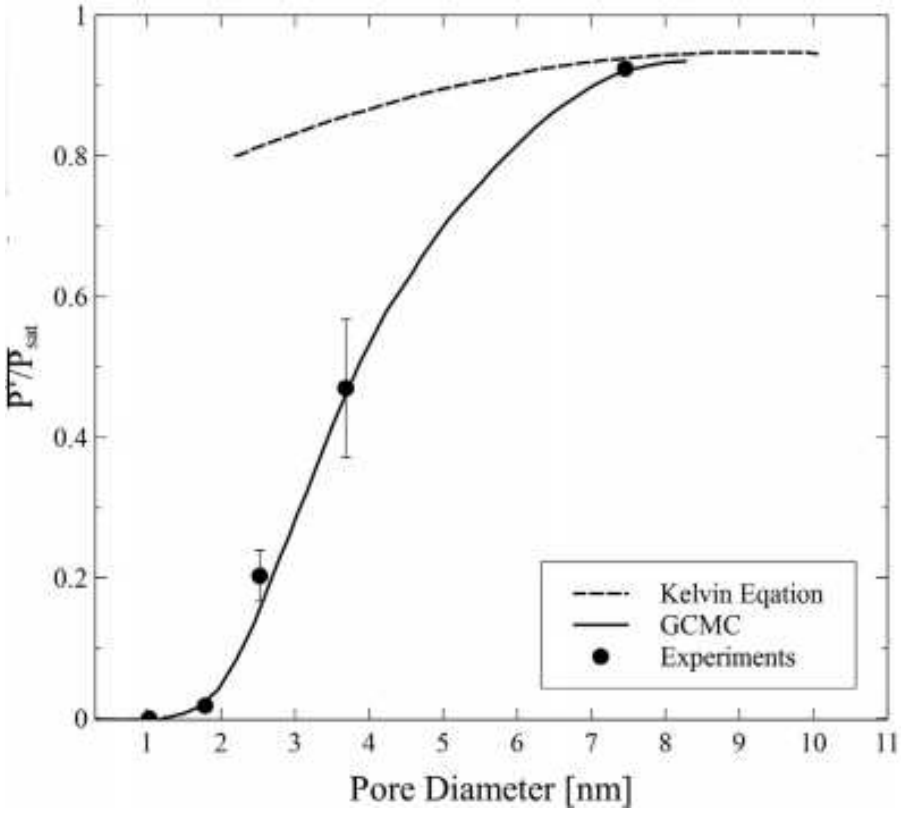

Figure 3.5: Limitation of Kelvin equation below 7.5 nm compared to experimental and simulation results (Walton and Quirke 1989).

Despite the limitations of the Kelvin equation, Chen et al. (2013) were able to incorporate a multicomponent version on the equation using gas composition from a Marcellus well and pore size distribution in a hypothetical shale to estimate the gas in place. To first validate their modified multicomponent equation, they used their equation to a single-component fluid (hexane) and compared it with results obtained using the traditional Kelvin equation. This comparison and the minor discrepancy observed is due to the fact that the Kelvin equation used the ideal gas law while their modified equation used real gas EOS to predict pressure more accurately at higher pressures as shown in Figure 3.6.

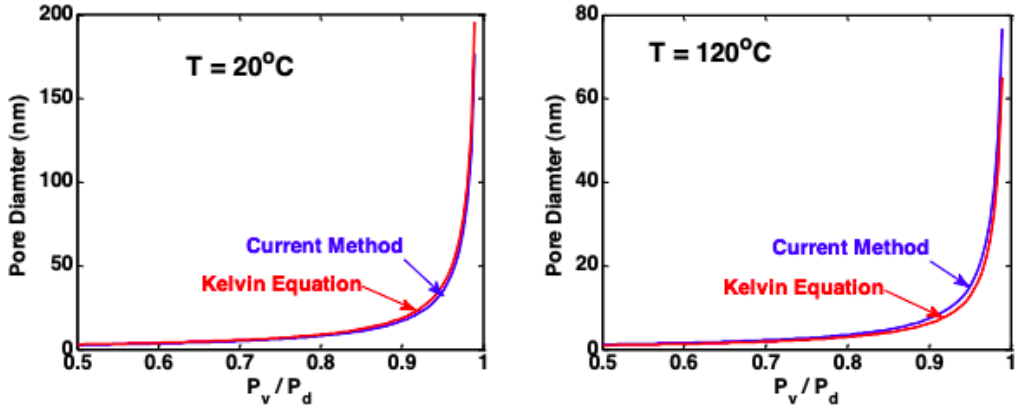

Figure 3.6: Pore size dependence on pressure validation (Chen et al. 2013).

3.4 Mathematical Formulation

Acoustic logs and seismic data are used to characterize the formation's geomechanical properties, porosity, permeability to further improve field development. Time-dependent measurements (4D seismic) can capture changes that occur during the lifetime of the reservoir. Wave propagation in shales with complex structures provide detailed information on geomechanical properties, anisotropy as well as rock-fluid interaction. Geomechanical properties are strongly dependent on pore pressure and the reservoir's thermodynamic conditions as well as the presence of natural fractures.

Acoustic waves traveling through a rock-fluid system generates an oscillatory squeezing action on the pore fluid between the grains. The fluid within the pore space introduces viscoelasticity into the system (Murphy et al. 1986). Murphy also deduced that tangential stiffness is not affected by the existence of fluid in the pore space and therefore introduced gap stiffness to account for it. This gap stiffness is responsible for the saturation and frequency dependence of the wave velocities and attenuations in the formation. The normal gap stiffness is the summation of dry matrix stiffness and the gap stiffness. In order to model this, the bulk material is assumed to be a Zener viscoelastic material. The effective normal stiffness and tangential stiffness of the rock are represented by:

$$k_{n,eff} = k_{n,m} + X k_{gap}(\omega) \tag{3.6}$$

$$k_{t,eff} = k_{t,m} \tag{3.7}$$

where $k_{n,m}$ and $k_{t,m}$ are the normal and tangential stiffness of the dry matrix; k_{gap} is the gap stiffness and X is a factor representing the density number of dissipative contacts (estimated to be 0.001) (O'Connell and Budiansky 1974; Murphy et al. 1986; Tutuncu 1992).

Through contact deformation, matrix tangential normal and tangential stiffness are calculated as

$$k_{n,m} = \frac{12\pi\rho_m R}{C_n}\left[V_p^2 - \frac{4}{3}V_s^2\right] \tag{3.8}$$

$$k_{t,m} = \frac{24\pi\rho_m R}{C_n}\left[V_p^2 - \frac{1}{3}V_s^2\right] \tag{3.9}$$

where R is the radius of the grains; ρ_m is the matrix density and C_n is the coordination number (number of grains contacting a single grain).

In order to determine gap stiffness as a function of frequency, the equation of squirt flow between two sinusoidal moving disks (as shown in Figure 3.7) with an angular frequency of $\omega = 2\pi f$ has to be solved (Murphy et al. 1986; Tutuncu 1992; Gurevich et al. 2010).

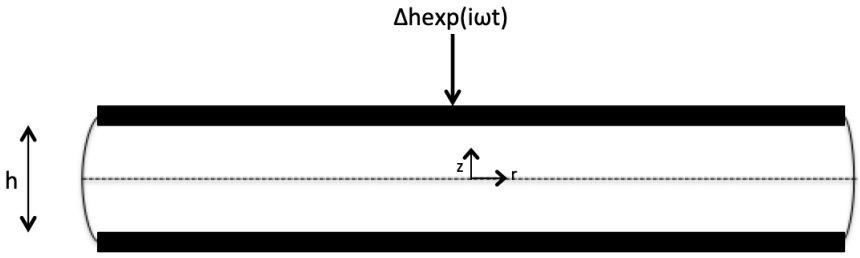

Figure 3.7: Squirt flow between two sinusoidal moving disks.

The equation of pressure can be obtained by solving the Navier-Stokes equation in cylindrical coordinates. For the squirt flow between parallel plates:

Continuity equation:

$$\nabla \cdot [\rho \mathbf{u}] = 0 \tag{3.10}$$

Navier-Stokes equation:

$$\rho \frac{D\mathbf{u}}{Dt} = -\nabla p + \rho \mathbf{g} - \mu \nabla^2 \mathbf{u} \tag{3.11}$$

where $\frac{D\mathbf{u}}{Dt}$ is material derivative of fluid velocity vector $\mathbf{u}$; p is fluid pressure; μ is fluid viscosity; ρ is fluid density.

In cylindrical coordinates, the continuity equation and Navier-Stokes equation can be written as

Continuity equation:

$$\frac{1}{r}\frac{\partial}{\partial r}(r u_r) + \frac{1}{r}\frac{\partial u_\theta}{\partial \theta} + \frac{\partial u_z}{\partial z} = 0 \tag{3.12}$$

r-component:

$$\rho\left(\frac{\partial u_r}{\partial t} + u_r\frac{\partial u_r}{\partial r} + \frac{u_\theta}{r}\frac{\partial u_r}{\partial \theta} - \frac{u_\theta^2}{r} + u_z\frac{\partial u_r}{\partial z}\right) = -\frac{\partial p}{\partial r} + \rho g_r + \mu\left[\frac{1}{r}\frac{\partial}{\partial r}\left(r\frac{\partial u_r}{\partial r}\right) - \frac{u_r}{r^2} + \frac{1}{r^2}\frac{\partial^2 u_r}{\partial \theta^2} - \frac{2}{r^2}\frac{\partial u_\theta}{\partial \theta} + \frac{\partial^2 u_r}{\partial z^2}\right] \tag{3.13}$$

θ-component:

$$\rho\left(\frac{\partial u_\theta}{\partial t} + u_r\frac{\partial u_\theta}{\partial r} + \frac{u_\theta}{r}\frac{\partial u_\theta}{\partial \theta} - \frac{u_r u_\theta}{r} + u_z\frac{\partial u_\theta}{\partial z}\right) = -\frac{1}{r}\frac{\partial p}{\partial \theta} + \rho g_\theta + \mu\left[\frac{1}{r}\frac{\partial}{\partial r}\left(r\frac{\partial u_\theta}{\partial r}\right) - \frac{u_\theta}{r^2} + \frac{1}{r^2}\frac{\partial^2 u_\theta}{\partial \theta^2} + \frac{2}{r^2}\frac{\partial u_r}{\partial \theta} + \frac{\partial^2 u_\theta}{\partial z^2}\right] \tag{3.14}$$

z-component:

$$\rho\left(\frac{\partial u_z}{\partial t}+u_r\frac{\partial u_z}{\partial r}+\frac{u_\theta}{r}\frac{\partial u_z}{\partial \theta}+u_z\frac{\partial u_z}{\partial z}\right)=-\frac{\partial p}{\partial z}+\rho g_z+ \\ \mu\left[\frac{1}{r}\frac{\partial}{\partial r}\left(r\frac{\partial u_z}{\partial r}\right)-\frac{u_r}{r^2}+\frac{1}{r^2}\frac{\partial^2 u_z}{\partial \theta^2}+\frac{\partial^2 u_z}{\partial z^2}\right] \quad (3.15)$$

Since the displacement amplitude is small and the gap between the grains is very narrow compared to the contact width, Murphy et al. (1986) linearized sectional volume to a 1-D equation as

$$\frac{\partial W}{\partial t}=-\frac{1}{L_o}\left(\frac{\partial p}{\partial r}+D_oW\right) \quad (3.16)$$

and

$$\frac{\partial h}{\partial t}+\frac{h_o}{K_w}\frac{\partial p}{\partial t}+\frac{\partial W}{\partial r}=-\frac{W}{r} \quad (3.17)$$

where $W=h_or$ is volumetric flow rate; $D_o=\dfrac{12\mu}{h_o^3}$ is viscous resistance; $L_o=\dfrac{2\rho}{h_o}$ is inertia.

Differentiating both sides of Equation 3.17 with respect to t yields

$$\frac{\partial^2 h}{\partial t^2}+\frac{h_o}{K_w}\frac{\partial^2 p}{\partial t^2}+\frac{\partial}{\partial r}\left(\frac{\partial W}{\partial t}\right)=-\frac{\partial}{\partial t}\left(\frac{W}{r}\right)=-\frac{1}{r}\frac{\partial W}{\partial t} \quad (3.18)$$

Substituting $\dfrac{\partial W}{\partial t}$ from Equation 3.16 into Equation 3.18 yields

$$\frac{\partial^2 h}{\partial t^2}+\frac{h_o}{K_w}\frac{\partial^2 p}{\partial t^2}-\frac{\partial}{\partial r}\left(\frac{1}{L_o}\frac{\partial p}{\partial r}+\frac{1}{L_o}D_oW\right)=-\frac{1}{r}\left[-\frac{1}{L_o}\left(\frac{\partial p}{\partial r}+D_oW\right)\right] \quad (3.19)$$

Multiplying both size of Equation 3.19 by L_o yields

$$L_o\frac{\partial^2 h}{\partial t^2}+L_o\frac{h_o}{K_w}\frac{\partial^2 p}{\partial t^2}-\frac{\partial}{\partial r}\left(\frac{\partial p}{\partial r}+D_oW\right)=\frac{L_o}{r}\left[\frac{1}{L_o}\left(\frac{\partial p}{\partial r}+D_oW\right)\right] \quad (3.20)$$

$$L_o\frac{\partial^2 h}{\partial t^2}+L_o\frac{h_o}{K_w}\frac{\partial^2 p}{\partial t^2}-\frac{\partial^2 p}{\partial r^2}-D_o\frac{\partial W}{\partial r}=\frac{1}{r}\frac{\partial p}{\partial r}+\frac{D_o}{r}W \quad (3.21)$$

$$L_o\frac{\partial^2 h}{\partial t^2}+L_o\frac{h_o}{K_w}\frac{\partial^2 p}{\partial t^2}-\frac{\partial^2 p}{\partial r^2}-\frac{1}{r}\frac{\partial p}{\partial r}=D_o\left(\frac{W}{r}+\frac{\partial W}{\partial r}\right) \quad (3.22)$$

From Equation 3.17, we obtain $\dfrac{\partial W}{\partial r}+\dfrac{W}{r}=-\left(\dfrac{\partial h}{\partial t}+\dfrac{h_o}{K_w}\dfrac{\partial p}{\partial t}\right)$, hence

$$L_o\frac{\partial^2 h}{\partial t^2}+L_o\frac{h_o}{K_w}\frac{\partial^2 p}{\partial t^2}-\frac{\partial^2 p}{\partial r^2}-\frac{1}{r}\frac{\partial p}{\partial r}=-D_o\left(\frac{\partial h}{\partial t}+\frac{h_o}{K_w}\frac{\partial p}{\partial t}\right) \tag{3.23}$$

$$\frac{\partial^2 p}{\partial t^2}-\frac{K_w}{h_oL_o}\frac{\partial^2 p}{\partial r^2}+\frac{D_o}{L_o}\frac{\partial p}{\partial t}-\frac{K_w}{rh_oL_o}\frac{\partial p}{\partial r}=-\frac{K_w}{h_oL_o}\left(L_o\frac{\partial^2 h}{\partial t^2}+D_o\frac{\partial h}{\partial t}\right) \tag{3.24}$$

When an acoustic wave propagates through rock and fluid in the contact region, the pressure $p(r,t)$ and the separation $h(r)$ in sinusoidal loading have the form

$$\begin{cases} p(r,t)=p\mathrm{e}^{i\omega t} \\ h(r)=\Delta h\mathrm{e}^{i\omega t} \end{cases} \tag{3.25}$$

The first and second derivatives of pressure $p(r,t)$ and separation distance $h(r)$ are calculated as

$$\begin{cases} \dfrac{\partial}{\partial t}p(r,t)=i\omega p \\ \dfrac{\partial^2}{\partial t^2}p(r,t)=-\omega^2 p \\ \dfrac{\partial}{\partial t}h(r)=i\omega\Delta h \\ \dfrac{\partial^2}{\partial t^2}h(r)=-\omega^2\Delta h \end{cases} \tag{3.26}$$

Substituting this into Equation 3.24, we obtain

$$\frac{\partial^2 p}{\partial r^2}+\frac{1}{r}\frac{\partial p}{\partial r}-i\omega\frac{12\mu}{K_{fluid}h_o^2}p=i\omega\frac{12\mu}{h_o^3}\Delta h \tag{3.27}$$

where μ is the viscosity of the gap fluid; r is the radial position; Δh is the amplitude of oscillation; K_{fluid} is the bulk modulus of saturated fluid and h_o is the initial separation distance.

In order to calculate this initial separation distance, we have to solve the equation of balance of surface forces as

$$p\mid_{r=a}=p_l=p_g-p_c \tag{3.28}$$

where p_g is the gas pressure; p_c is the capillary pressure which is calculated from the contact radius r_c:

$$p_c = \frac{2\gamma \cos\theta_c}{r_c} \tag{3.29}$$

The Navier-Stokes equation is then converted into a homogeneous Bessel equation of zero order by introducing a new variable $\xi = p - \frac{K_{fluid}\Delta h}{h_o}$. The conversion yields the solution $\xi = CJ_o(\zeta r)$ (Bui and Tutuncu 2014). The solution of Equation 3.27 is:

$$p = CJ_o(\zeta r) + \frac{K_{fluid}\Delta h}{h_o} \tag{3.30}$$

where J_o is the zeroth order Bessel function and $\zeta^2 = i\omega\frac{12\mu}{K_{fluid}h_o^2}$ is the wavenumber. C, the integral constant can be calculated from the boundary condition:

$$C = \frac{p_g - p_c - \frac{K_{fluid}\Delta h}{h_o}}{J_o(\zeta a)} = \frac{p_g - p_c}{J_o(\zeta r)} - \frac{K_{fluid}\Delta h}{h_o J_o)\zeta a)} \tag{3.31}$$

Pressure in the gap is obtained as

$$p = (p_g - p_c)\frac{J_o(\zeta r)}{J_o(\zeta a)} + \frac{K_{fluid}\Delta h}{h_o}[1 - \frac{J_o(\zeta r)}{J_o(\zeta a)}] \tag{3.32}$$

The acoustic force applied on the solid particle corresponding to the displacement (Δh) by the fluid is obtained by:

$$\Delta F = \int_0^a pdA = \int_0^a \left\{ (p_g - p_c)\frac{J_o(kr)}{J_o(ka)} + \frac{K_{fluid}\Delta h}{h_o}\left[1 - \frac{J_o(\zeta r)}{J_o(\zeta a)}\right]\right\} 2\pi r dr \tag{3.33}$$

This can be simplified to obtain:

$$\Delta F = -\pi a^2 \left\{ (p_g - p_c)\frac{J_o(\zeta a)}{J_o(\zeta a)} + \frac{K_{fluid}\Delta h}{h_o}\left[1 - \frac{J_o(\zeta a)}{J_o(\zeta a)}\right]\right\} \tag{3.34}$$

Gap stiffness can then be calculated using:

$$k_{gap(\omega)} = \frac{\Delta F}{-\Delta h} = \pi a^2 \left\{ \frac{(p_g - p_c)}{\Delta h} J(\zeta a) + \frac{K_{fluid}\Delta h}{h_o}\left[1 - \frac{J_o(\zeta a)}{J_o(\zeta a)}\right]\right\} \tag{3.35}$$

If the sample is saturated with a single fluid only, the capillary pressure is reduced to 0. Pressure of the saturated sample can be used. Effective compressional (M) and shear (G) moduli are obtained from Winkler (1983) as follows

$$M = \rho V_p^2 = \frac{3(1-\phi)C_n}{20\pi R}\left[k_n + \frac{2}{3}k_t\right] \tag{3.36}$$

$$G = \rho V_s^2 = \frac{(1-\phi)C_n}{20\pi R}\left[k_n + \frac{3}{2}k_t\right] \tag{3.37}$$

3.5 Determination of Contact Radius and Separation Distance

Grains are assumed to be in direct contact in the original Hertz contact theory and therefore it does not take surface forces into account. Murphy (1982) concluded that a gap exists between the grains. The determination of separation distance and deformation based on thermodynamic balance are of crucial importance and should be incorporated in the grain contact model. Tutuncu (1992) developed a method to calculate this separation distance using a balance of surface and external forces that exhibited a good match to experimental data. This allows modeling the effects of fluid type and electrochemical properties on the geomechanical properties of the rock.

Since two phases are present in different parts of the gap, this further complicates the calculation of surface forces and surface energy. Surface forces include electrostatic, structural and Born repulsive forces and Van der Waals attractive forces. All external forces should be balanced by the total internal force when the system is in equilibrium. Equilibrium separation distance is defined as the distance between two spherical grain surfaces when the total surface force is equal to the external force. This balance of surface forces is represented by Equation 3.38

$$\Delta H = \Delta U_s + \Delta U_E + \Delta pV = \Delta U_s + \Delta U_E + F_o\delta \tag{3.38}$$

where ΔH is the change in enthalpy; ΔU_s is the change in surface energy between two spheres; ΔU_E is the change in elastic energy of two spheres in contact.

The change in internal energy is the result of changes in both state of strain of the grains and the compression of the fluid between he two grains. The product of F_o (external force) and δ (distance moved) represents volumetric work. Enthalpy is minimized at equilibrium:

$$\frac{\partial \Delta H}{\partial h} = \frac{\partial}{\partial h}(\Delta U_s) + \frac{\partial}{\partial h}(\Delta U_E) + \frac{\partial}{\partial h}(F_o \delta) = 0 \tag{3.39}$$

The first term represents total surface force, the second term represents the applied force, and the third term becomes zero since both F_o and δ are independent from h. This simplifies the Equation 3.34 to

$$F_o = F_{ts}(h_o, \alpha) \tag{3.40}$$

where F_o is the applied force; F_{ts} is total surface force which is evaluated at the equilibrium distance of separation h_o and a deformation of α. In order to calculate the total surface force, we need to evaluate the total disjoining pressure at each separation distance (within contact region and in non-contact region) by summing Van der Waals attraction, electrostatic repulsion, structural and Born forces which is represented in Equation 3.41.

$$F_t(h_o) = -\frac{A}{6\pi h_o^3} + \frac{64nkT}{\kappa}\beta^2 e^{-\kappa h_o} + K_1 e^{\frac{-h_o}{l}} + \frac{1}{45}\frac{A\sigma_{cp}^6}{h_o^9} \tag{3.41}$$

where A is the Hamaker constant; n is the ion concentration; K_1 and l are the structural constants; σ_{cp} is the collision parameter and κ is the inverse Debye-Huckel length parameter and is obtained from Equation 3.42.

$$\begin{cases} \kappa = \sqrt{\dfrac{8\pi n e^2 Z^2}{\varepsilon kT}} & (a) \\ y = \dfrac{\Psi e Z}{kT} & (b) \\ \beta = \dfrac{e\dfrac{y}{2} - 1}{e\dfrac{y}{2} + 1} & (c) \\ A = \dfrac{3}{4}k_{BM}T\left(\dfrac{\varepsilon_1 - \varepsilon_3}{\varepsilon_{1+\varepsilon_3}}\right)^2 + \dfrac{3hv_e}{16\sqrt{2}}\dfrac{(n_1^2 - n_3^2)^2}{(n_1^2 + n_3^2)^{1.5}} & (d) \end{cases} \tag{3.42}$$

where e is the electronic charge; Z is the valence of the electrolyte; k_{BM} is the Boltzman constant; T is the absolute temperature; h is the Plank's constant; v_e is the absorption frequency of the fluid; n_1 is the refraction index for the solid spheres; n_3 is the refraction index for the fluid between the spheres; ε_1 is the dielectric constant of the spheres; ε_3 is the dielectric constant of the fluid and ψ is the zeta potential of the grains.

Total surface force on grains can be calculated by adding the forces in the contact and non-contact regions:

$$F_{ts}(h_o) = \pi a^2 F_t(h_o) + \int_a^R 2\pi F_t(h_o) r dr \tag{3.43}$$

This calculation should be simple in the case of a single phase existing within the pore space. However, the calculation is complicated in the case with capillary condensation. We therefore need to numerically evaluate the integral in two parts for gas and liquid in the contact and non-contact regions.

3.6 Determination of Fluid Properties

Since the fluid inside the pore has to be in thermal equilibrium at a given temperature and pressure, fluid properties have to be determined theoretically from the equation of state. In order to calculate the fluid properties, the Peng-Robinson EOS was used. Two forms of the equation were used (in terms of specific volume and gas deviation factor) (Whitson and Brulé 2000):

$$v^3 - \left(\frac{RT}{p} - b\right) v^2 - \left(\frac{a}{p} - \frac{2bRT}{p} - 3b^2\right) v - b\left(\frac{a}{p} - \frac{bRT}{p} - b^2\right) = 0 \tag{3.44}$$

$$z^3 - \left(\frac{RT}{p} - b\right)) z - \left(\frac{a}{p} - \frac{2bRT}{p} - 3b^2\right) z - b\left(\frac{a}{p} - \frac{bRT}{p} - b^2\right) = 0 \tag{3.45}$$

where $z = \dfrac{PV}{RT}$; v is the specific volume and z is the gas deviation factor.

Equation 3.45 can be represented as:

$$z^3 - (1 - B)z^2 + (A - 2B^2 - 2B)z - (AB - B^2 - B^3) = 0 \tag{3.46}$$

where a, b, A and B are represented as

$$a = \sum_{m=1}^{n_c} \sum_{n=1}^{n_c} a_{mn} x_m x_n \tag{3.47}$$

$$b = \sum_{n=1}^{n_c} b_n x_n \tag{3.48}$$

$$A = a\frac{p}{(RT)^2} = \frac{p}{(RT)^2}\sum_{m=1}^{n_c}\sum_{n=1}^{n_c} a_{mn}x_m x_n \tag{3.49}$$

$$B = b\frac{p}{RT} = \frac{p}{RT}\sum_{n=1}^{n_c} b_n x_n \tag{3.50}$$

The coefficients a_m and a_{mn} are calculated as

$$\sqrt{a_m} = 0.45724\frac{R^2 T_{c,m}}{p_{c,m}}\left[1 + k_c(1 + k_c(1 - \sqrt{T_{r,m}})\right]^2 \tag{3.51}$$

$$a_{mn} = (1 - \delta_{mn})\sqrt{a_n a_m} \tag{3.52}$$

The coefficient k_c is obtained from Equation 3.53

$$k_c = \begin{cases} 0.37464 + 1.34226\omega_m - 0.26992\omega_m^2, \text{ if } \omega_m{<}0.49 \\ 0.3796 + 1.485\omega_m - 0.1644\omega_m^2 + 0.01667\omega_m^3, \text{ if } \omega_m{>}0.49 \end{cases} \tag{3.53}$$

where $T_{c,m}$ and $T_{r,m}$ are the critical and reduced critical temperature of component m respectively; n_c is the number of components; δ_{mn} is the binary interaction coefficient between two components m and n; k_c is a coefficient and ω_m is the acentric factor. The acentric factor for CO_2 is 0.225.

The specific volume correction value is obtained using Equation 3.54 (Whitson and Brulé 2000).

$$\begin{cases} v_L = v_L^{EOS} - \sum_{m=1}^{n_c} c_m x_m \\ v_V = v_V^{EOS} - \sum_{m=1}^{n_c} c_m y_m \end{cases} \tag{3.54}$$

where v_L^{EOS} and v_V^{EOS} are the EOS-calculated liquid and vapor molar volumes respectively; x_m and y_m are the liquid and vapor composition respectively and c_m is the Peneloux volume correction factor calculated from critical pressure and temperature using Equation 3.55 (Pendersen et al. 2007).

$$c_m = \frac{0.40768RT_{c,m}(0.29441 - z_{A,m})}{p_{c,m}} \tag{3.55}$$

where $z_{R,m}$ is the Rackett compressibility factor for component m and is calculated by using Equation 3.56.

$$z_{R,m} = 0.29056 - 0.08775\omega_m \tag{3.56}$$

Equation 3.44 can be numerically solved (for a specific volume, v and a gas deviation factor, z) when the components properties are available. Once the gas deviation factor is obtained, gas compressibility can be calculated using Equation 3.57.

$$c_g = \frac{1}{\rho_g}\frac{\partial \rho_g}{\partial p_g} = \frac{1}{p_g} - \frac{1}{z}\frac{\partial z}{\partial p_g} \tag{3.57}$$

where $\dfrac{\partial z}{\partial p_g}$ can be determined using Equation 3.58.

$$\frac{\partial z}{\partial p_g} = \begin{bmatrix} \dfrac{B - z}{3z - 2(1-B)z + (A - 3B^2 - 2B)R^2T^2} \\ -\dfrac{z^2 - 6Bz - 2z - A + 2B + 3B^2}{3z - 2(1-B)z + (A - 3B^2 - 2B)}\dfrac{b}{RT} \end{bmatrix} \tag{3.58}$$

The first and second derivative of oil density with respect to pressure can be obtained using Equations 3.59 and 3.60.

$$\frac{\partial \rho_o}{\partial p_o} = \frac{\rho_o}{p_o} - \frac{\rho_o}{z}\frac{\partial z}{\partial p_o} \tag{3.59}$$

$$\frac{\partial^{2\rho_o}}{\partial p_o^2} = \frac{1}{p_o}\frac{\partial \rho_o}{\partial p_o} - \frac{\rho_o}{p_o^2} - \frac{1}{z}\frac{\partial \rho_o}{\partial p_o} + \frac{\rho_o}{z^2}\frac{\partial z}{\partial p_o} - \frac{\rho_o}{z}\frac{\partial^2 z}{\partial p_o^2} \tag{3.60}$$

The last term can be obtained using Equation 3.61.

$$\frac{\partial^2 z}{\partial p_o^2} = \left\{ \begin{array}{c} \dfrac{-A + B + z + B^2}{[3z - 2(1-B)z + (A - 3B^2 - 2B)]^2}\dfrac{1}{R^2T^2}\dfrac{\partial z}{\partial p_o} - \\ \dfrac{(-15zB - 4z - 12B^2z) + (A - 3B^2 - 2B)(2z - 8B - 3)}{[3z - 2(1-B)z + (A - 3B^2 - 2B)]^2}\dfrac{b}{RT}\dfrac{\partial z}{\partial p_o} \end{array} \right\} \tag{3.61}$$

where $\dfrac{\partial z}{\partial p_o}$ can be calculated from the EOS for oil.

To summarize, the model developed provides a theoretical way to determine V_p and V_s changes due to capillary condensation by calculating gap stiffness (which is the stiffness component affected by saturation). In order to calculate the gap stiffness, the separation distance between grains had to be determined which in turn was calculated by an iterative process.

CHAPTER 4

RESERVOIR CHARACTERIZATION

This chapter summarizes the reservoir characterization of formations from which the cores in this study originated. After evaluating available core samples and formations, we decided to test core samples from the Austin Chalk and the Diyab formations. The focus of this chapter is to provide an overview of the geological and petrophysical background of the formations as well as the samples collected.

4.1 Austin Chalk Reservoir

The Austin Chalk was deposited in Late Cretaceous seas that covered the Gulf Coast basin in Texas. The map below shows the US part of the Austin Chalk trend between the black lines. Sediments consists of fine-grained limestone with interbedded streaks of shale. Figure 4.1 shows the areal extent of the Austin Chalk trend. It overlays the Eagle Ford shale with a formation consisting of interbedded chalks, volcanic ash and marls. It is classified as a biomicrite and is primarily composed of coccoliths. The Upper Cretaceous stratigraphic column of the Eagle Ford shale is shown in Figure 4.2.

The Austin Chalk has three main members namely the lower chalk, middle marl and the upper chalk. The upper and lower members contain significantly less clay meaning they are more brittle with higher fracture densities and are therefore of better reservoir quality Hovorka and Nance (1994) characterized the three members in great detail. The lower and upper members consists of chalk intervals mainly interbedded with marl. These member contains thin dark chalks and laminated marls that contain as much as 3.5 percent TOC as well as disseminated pyrite. The middle member consists of alternating chalk and light-colored marl and has a higher clay content than the other layers. These distinct three members are illustrated in Figure 4.3. The cores used in this research were acquired from Eagleville field in Gonzalez County, Texas.

Figure 4.1: The Austin Chalk trend (Hovorka and Nance 1994).

The Austin Chalk in Texas is a low porosity, low permeability, heavily-fractured reservoir that has been producing since the mid-1980s with the aid of horizontal drilling. Matrix permeability ranges between 0.03 to 1.27 md and overall formation thickness ranges between 150 to 800 ft. The Eagle Ford shale is classified as a self-sourced reservoir with seals. Outcrop analysis identified kerogen types II, II/III and III. The maturation process (migration, expulsion and migration) through three maturation windows (oil, gas condensate and dry gas) are shown in Figure 4.4.

Hydrocarbon migration occurred mainly along bedding planes during expulsion. Due to the lack of traps along its path, hydrocarbons migrated up-dip where vertical fractures were encountered. These fractures are associated with regional fault trends and aided the migration to the heavily-fractured Austin Chalk (Martin et al. 2011).

The underlaying Eagle Ford formation has negligible vertical permeability but some hydrocarbon migration occurred along bedding planes after expulsion. The organic matter that travels through the maturation window is able to travel up-dip the Eagle Ford formation where it could encounter natural fractures and faults. These fractures either allow for vertical flow or restrict future migration thereby controlling the ultimate accumulation of hydrocarbon as illustrated in Figure 4.5.

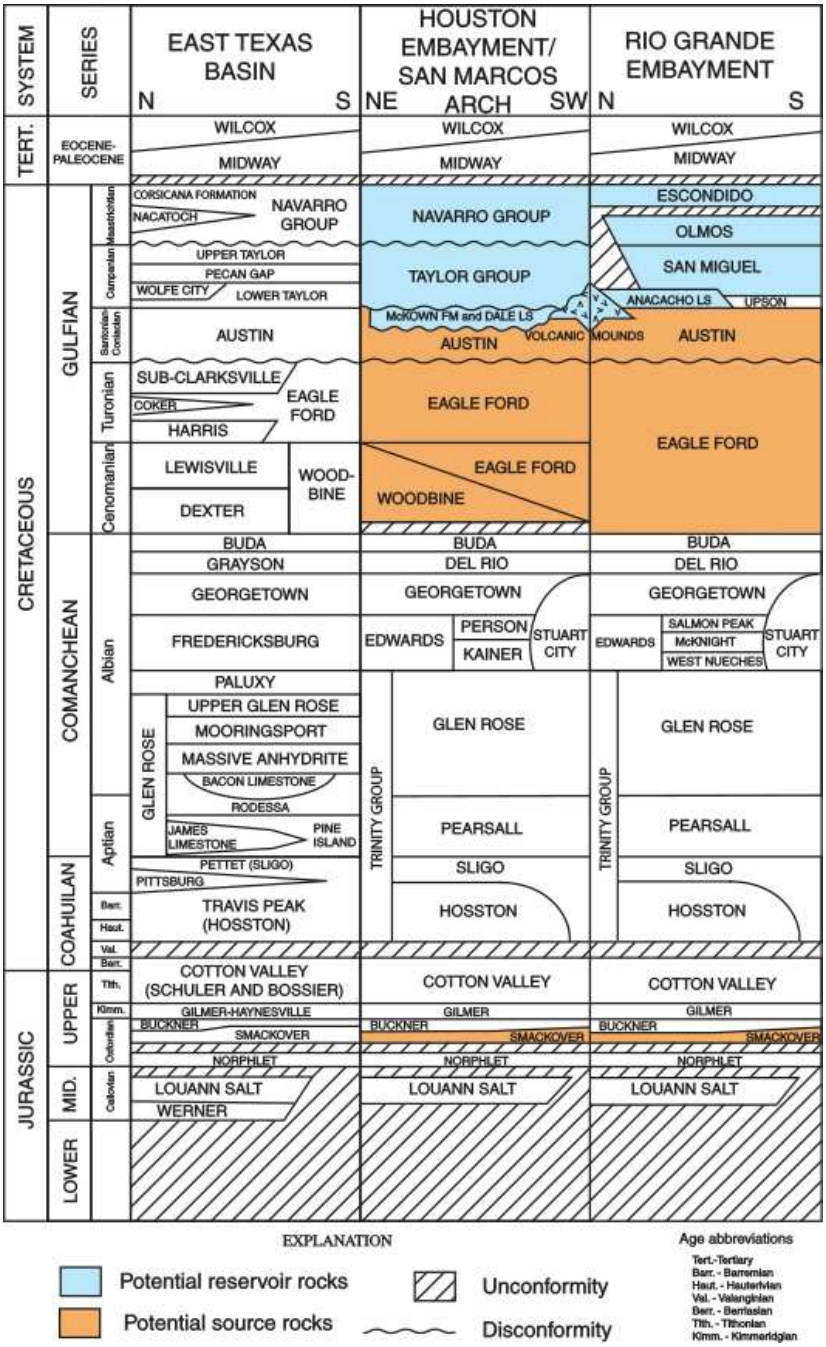

Figure 4.2: Stratigraphic column of Eagle Ford (Hovorka and Nance 1994).

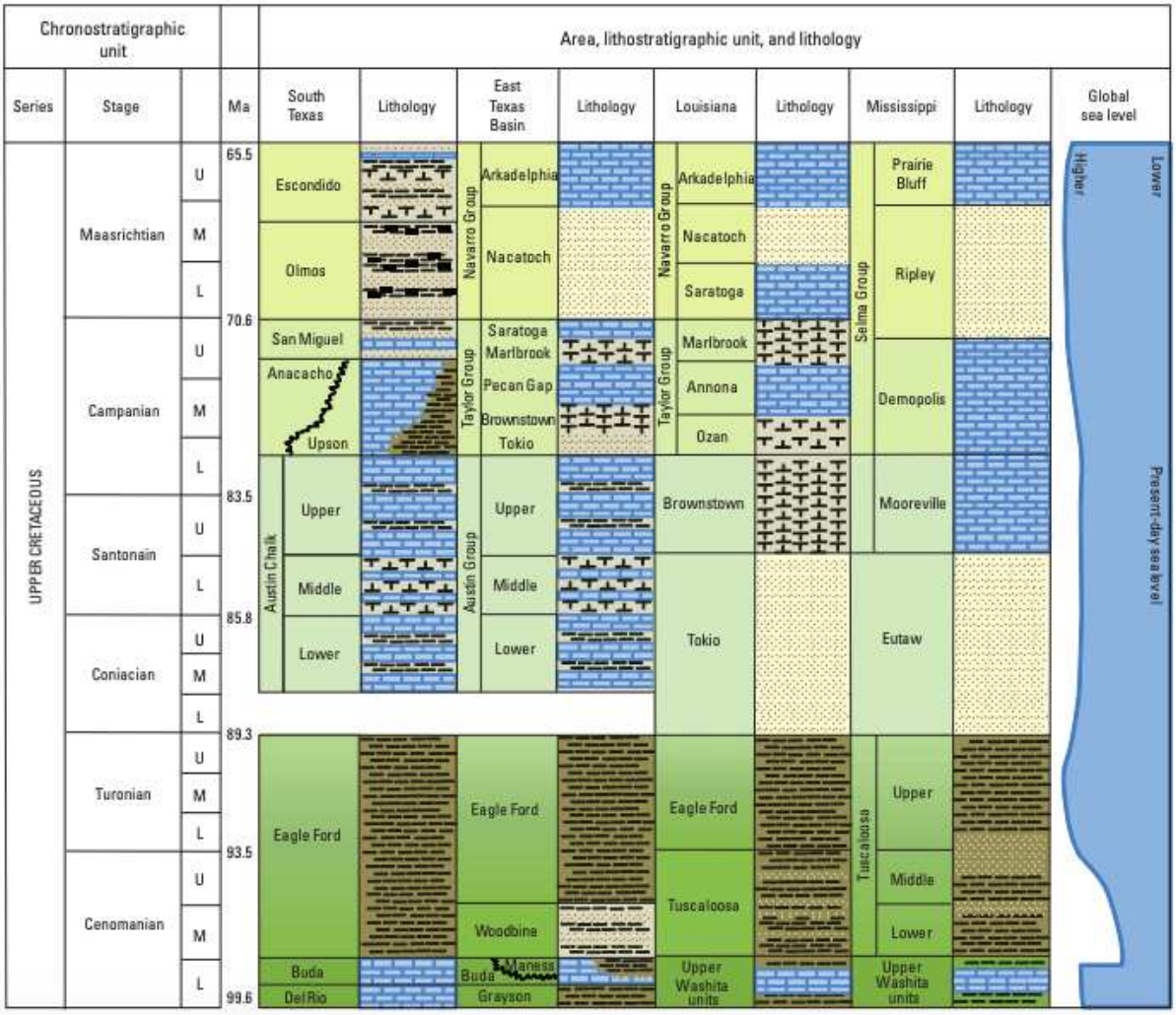

Figure 4.3: Detailed stratigraphic column showing Austin Chalk members (Hovorka and Nance 1994).

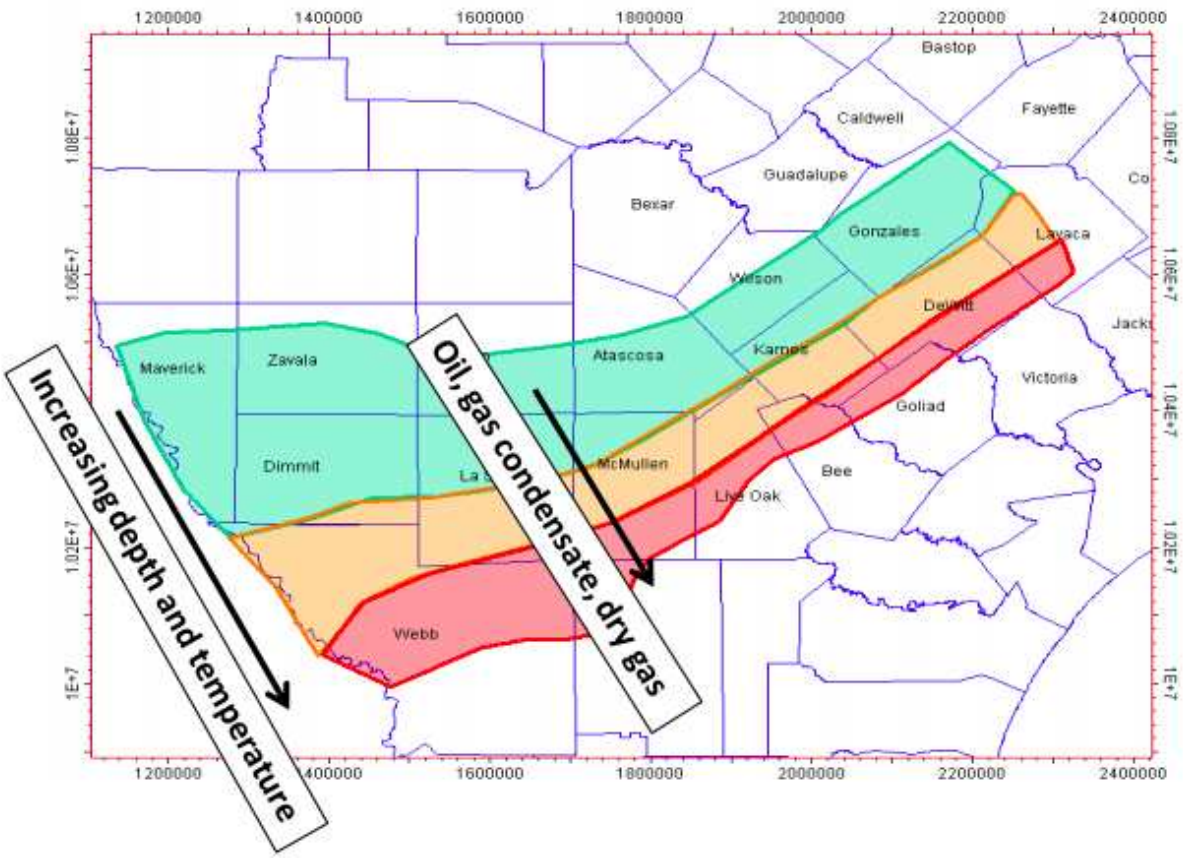

Figure 4.4: Eagle Ford maturation window (Martin et al. 2011).

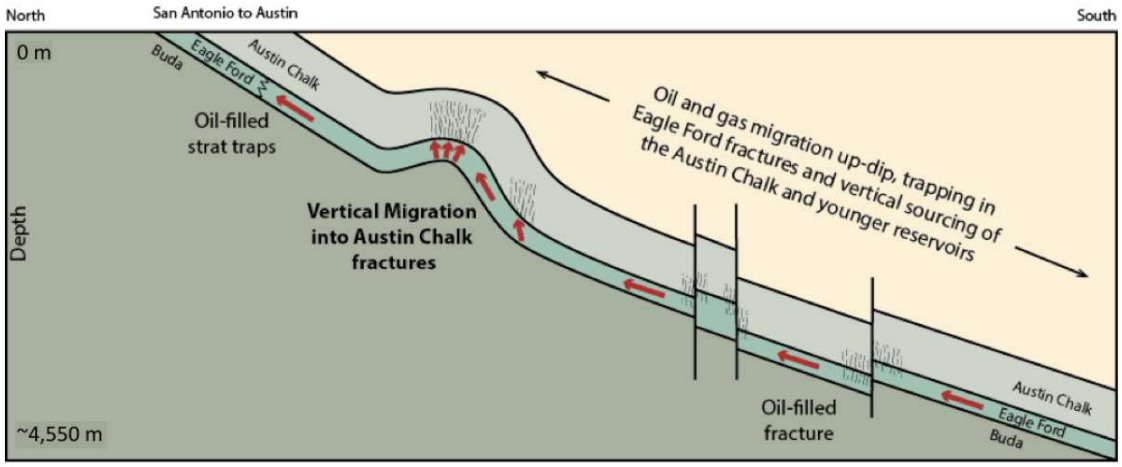

Figure 4.5: Hydrocarbon migration paths in the Eagle Ford and Austin Chalk petroleum systems (Martin et al. 2011).

4.2 Diyab Unconventional Reservoir

The Diyab source rock, located in the United Arab Emirates (UAE), represents ADNOC's latest endeavor to explore and develop its unconventional resources. It was evaluated over the last several years to assess its potential for development as an unconventional shale formation. The Diyab formation has historically been viewed as the source rock for major oil and gas formations in the Middle East. After recent studies, it was decided to explore Diyab further as an unconventional gas reservoir. This was evaluated based on the source rock's thermal maturity, rock properties, lithology, facies and stimulation studies.

Initial studies have shown that the Diyab formation has three distinct zones with good potential for shale gas. Those zones were identified based on porosity, saturation and total organic content. Figure 4.6 shows the vitrinite maturity at the base of the Diyab formation. Vitrinite maturity is caused by thermal stress to generate oil and gas in the Jurassic and Cretaceous petroleum systems.

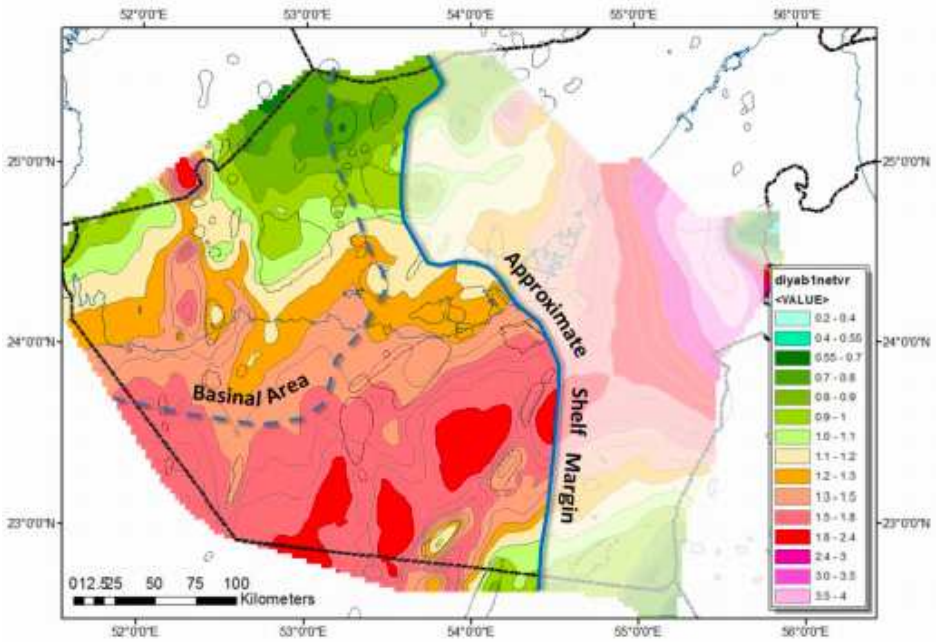

Figure 4.6: Vitrinite maturity from 3D basin modeling of the Diyab Unit (Baig et al. 2017).

The Diyab formation is a lithology-based term used in the UAE to represent sediments of Oxfordian to Kimmeridgian age. It is the Saudi equivalent of the Tuwaiq, Hanifa and Jubaila formations combined as a single unit as shown in Figure 4.7. The three main units are distinguished in Figure 4.8 After a major unconformity between the Middle and Late Jurassic, an intra-shelf basin formed in the Late Jurassic period between the uplifted Eastern Plate margin and the Qatar Arch. The major sequences (Hanifa, Tuwaiq and Hadria) demonstrate westward progradation with forced regression of shallow water carbonate intervals into the basins (Vahrenkamp et al. 2015).

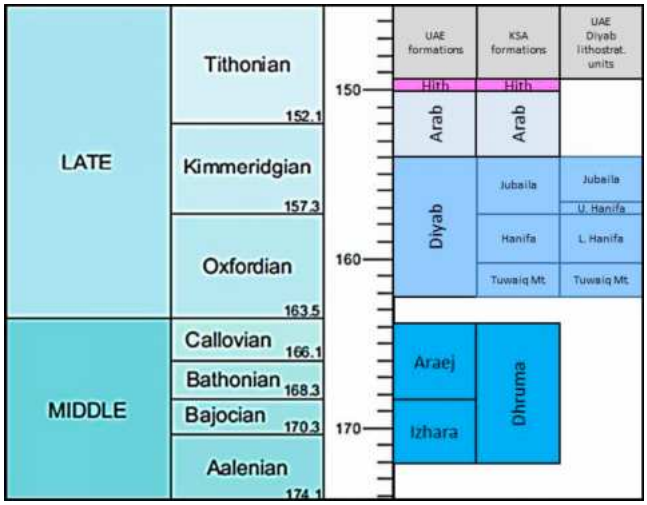

Figure 4.7: Middle and Late Jurassic Diyab unit lithology (Baig et al. 2017).

The lower part of the Diyab unit (Tuwaiq and Lower Hanifa) demonstrates observable thickness variations from shelf areas made up of shoals and grainy deposits up to 1000 ft thickness to less than 100 ft in intra-shelf basinal settings which dominate depositional patterns up in the western UAE as shown in Figure 4.9. These sediments contain Oxfordian and Kimmeridgian source rock sequences (Baig et al. 2017). The upper part of the Diyab unit (Jubaila and Upper Hanifa) is mostly comprised of basin-filled sequences with partial source rock developments. These rocks were subjected to thermal stress resulting in the generation of oil and gas and are the major source rocks to the Jurassic/Cretaceous petroleum systems in the region. After evaluating pilot results, it was found that the Jubaila and Hanifa

formations have a good potential for shale gas development with the lower sections showing more promise than the upper sections.

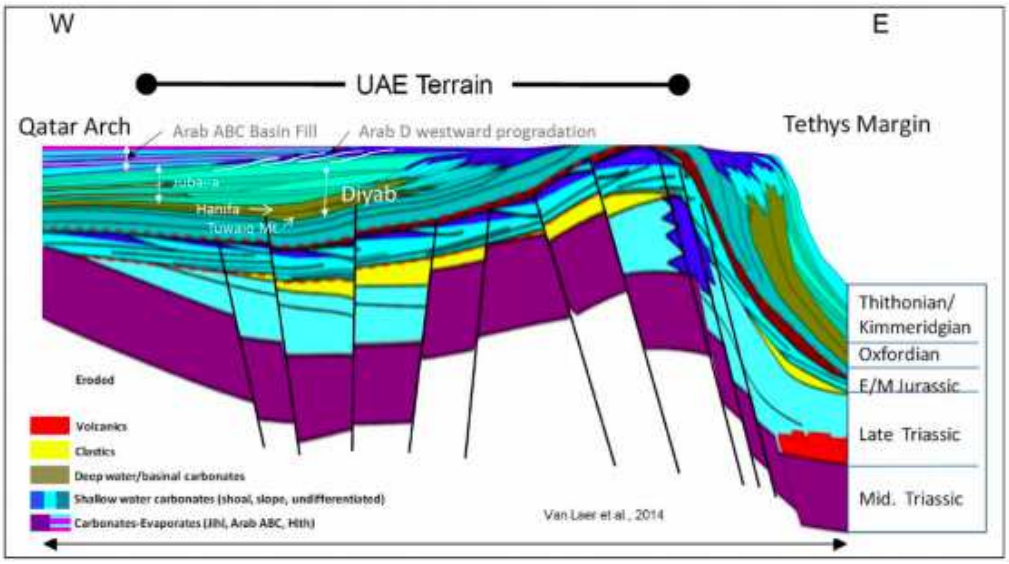

Figure 4.8: Cross sectional stratigraphy of the Diyab unit. Late Jurassic intra-shelf basin development (Baig et al. 2017).

State of the art elemental spectroscopy measurements were conducted to determine the elemental compositions to estimate the rock's mineralogy including carbon. This is important in quantifying the unconventional resource and estimating reservoir quality. Total carbon content was split into organic and inorganic carbon. Track 3 indicate methane presence while tracks 4 and 5 indicate liquid hydrocarbon presence ($C_2 - C_5$). Light hydrocarbon composition was observed in the Hanifa and Jubaila formations signifying higher maturity. Based on fluid log signatures, three zones were characterized as shown in the composite log in Figure 4.10. Zone 1 demonstrated high methane composition (99% dry gas) while Zone 2 indicated trace liquid hydrocarbon components (<5% $C_2 - C_5$). Zone 3 (Hanifa) also has a primarily dry gas log signature. These logs were obtained using ASFL (Advanced Surface Facies Logging) technology which analyzes hydrocarbon present in drilling mud. As drilling fluid is brought to the surface, it is analyzed to provide $C_1 - C_8$, toluene, carbon dioxide, helium, benzene and alkane content. This allows the identification of sweet spots and is valuable when evaluating reservoir potential.

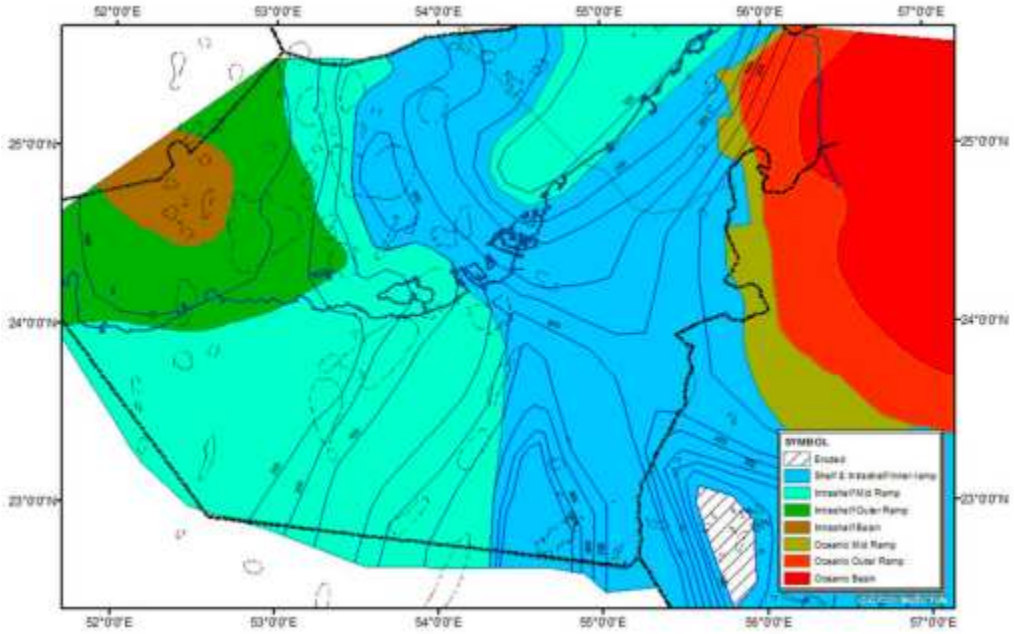

Figure 4.9: Cross sectional depositional area of Lower Diyab (Baig et al. 2017).

Heterogeneous Rock Analysis (HRA) was then performed on selected core samples over the cored interval. HRA is a comprehensive rock classification tool based on well log responses which matches rock patterns with similar material properties in an interval. Five rock intervals were identified as shown in Figure 4.11. One foot of core was preserved for every 9 ft for core analysis and saturation measurements. Out of the 39 samples used in HRA, 16 samples were located in non-reservoir sections and were re-allocated to reservoir intervals. Figure 4.11 shows the depths at which those core samples were selected.

XRD (X-ray Diffraction) analysis were performed with good comparison between log and core derived mineralogy. Significant mineralogy changes were observed as we move from the Hanifa to Jubaila formations (above and below evaporates). The Hanifa reservoir is mainly comprised of calcite with traces of clay, whereas Jubaila has an increased level of clastic material especially in lower section of the Jubaila formation. That is manifested by the laminations ore calcareous layers interbedded by more carbonate-rich and clay-rich intervals. The XRD analysis composite log of this formation is shown in Figure 4.12. It

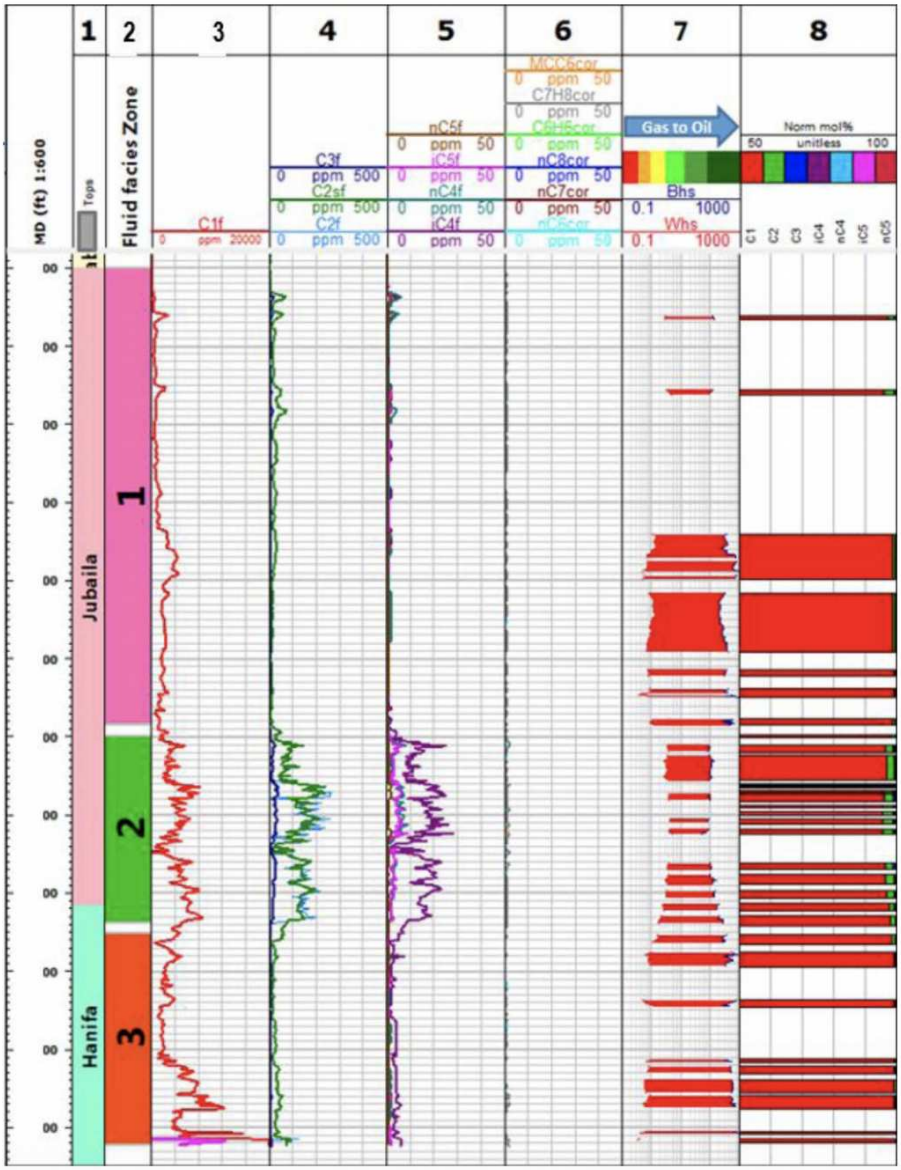

Figure 4.10: Composite log showing the different zones of interest in the Diyab formation. Zones 1 and 3 show a dry gas composition while zone 2 shows the presence of liquid hydrocarbon components (Baig et al. 2017).

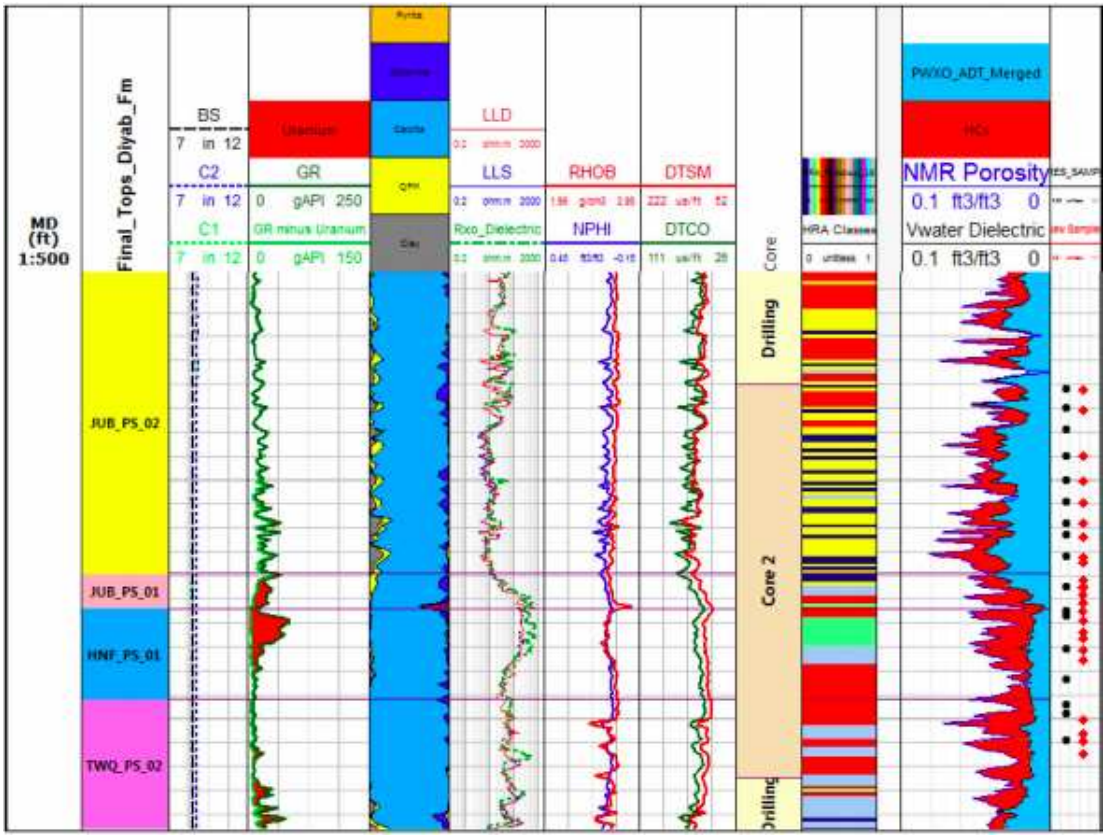

Figure 4.11: HRA identification (Baig et al. 2017).

is observed that there is a slight increase in clay content in the bottom of the Jubaila and Hanifa formations which coincides with an increase in TOC.

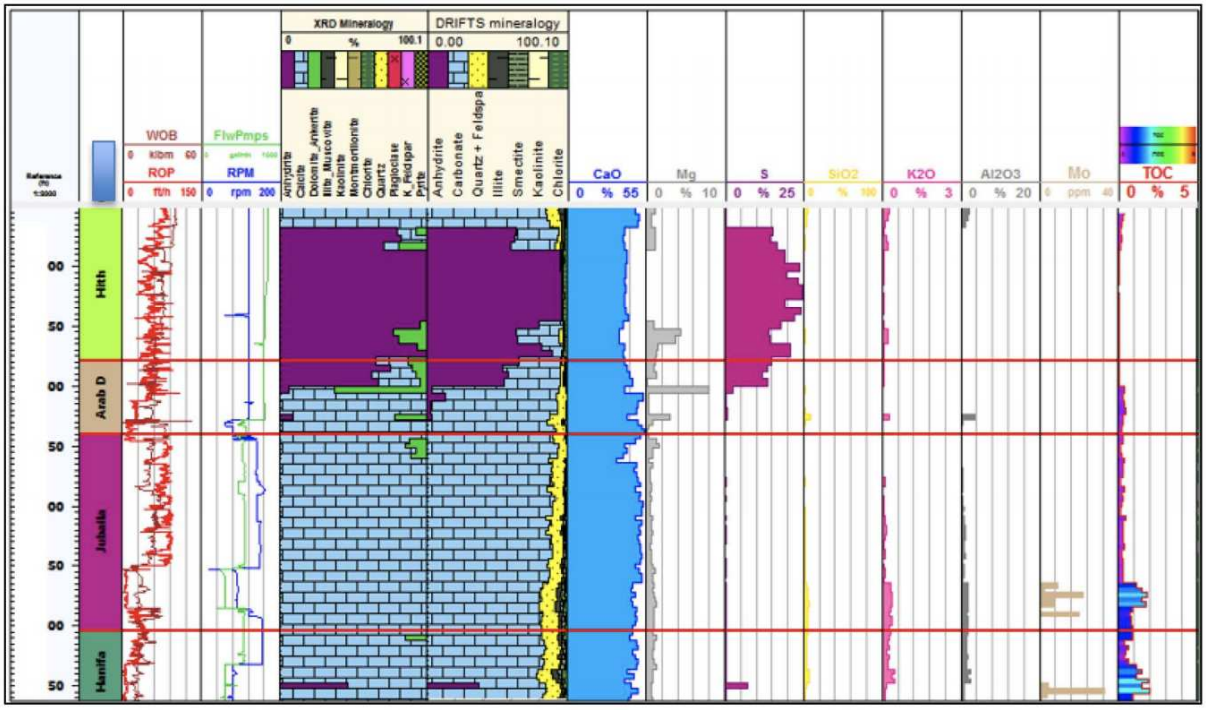

Figure 4.12: Composite log utilizing cutting analysis to identify lithology (Vahrenkamp et al. 2015).

4.2.1 Comparison to US Shale Reservoirs

In the early stages of exploration, ADNOC was interested in looking at analogues in the US with similar mineralogy. Ternary plots were used to characterize samples from the Hanifa and Jubaila formations and compared to the composition of the Marcellus, Eagle Ford and Barnett formations as shown in Figure 4.13. The Hanifa and Jubaila formations are both predominantly comprised of carbonate (>90%) even if the TOC rich zones contain small amounts of clays. On the other hand, the Eagle Ford formation, which has the highest carbonate concentration of around 60% and contains high amounts of clay (20%). It can therefore be concluded that facies from the Hanifa and Jubaila formations are unique and require a customized completion workflow.

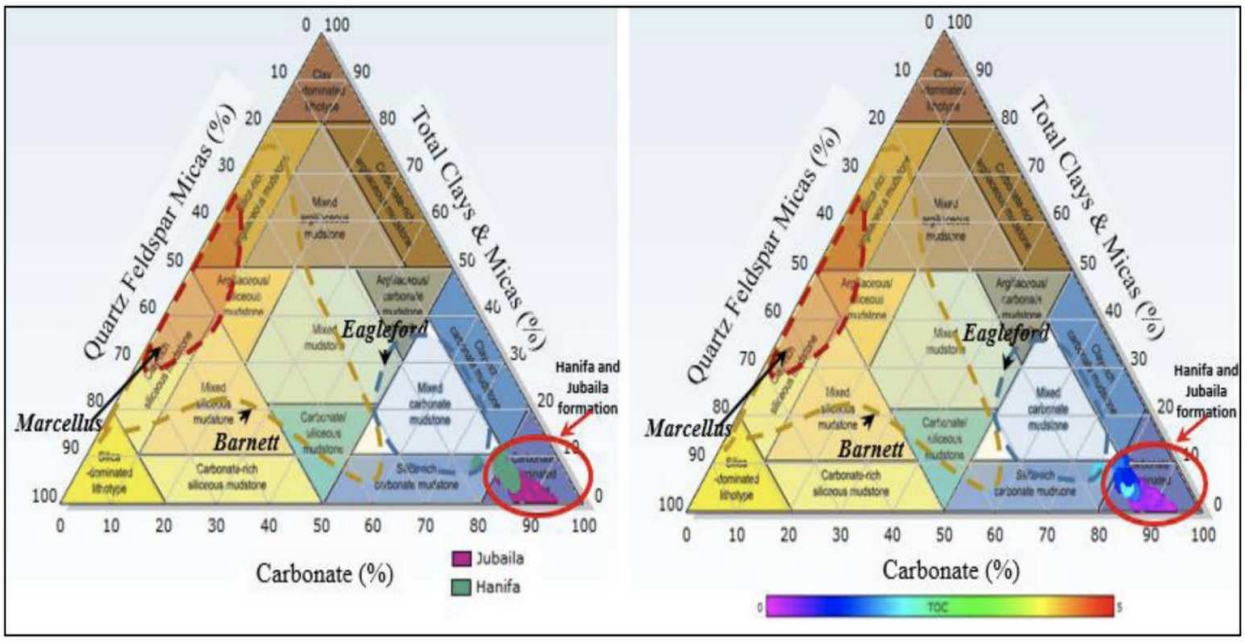

Figure 4.13: Ternary plots comparing the lithofacies of Hanifa and Jubaila to U.S. shale reservoirs (Marcellus, Eagle Ford and Barnett) (Vahrenkamp et al. 2015).

4.2.2 Crushed Core Analysis of Diyab Reservoir

Conventional methods to analyze core porosity and permeability cannot be applied here due to the challenging nature of tight rocks. Instead, crushed rock analysis is used to obtain bulk density, gas-filled porosity, core saturation and matrix gas permeability. The cores (conventional or sidewall) are to be first preserved until the time of rock analysis. The bulk densities are measured by mercury immersion before the sample is crushed. Water and oil are then extracted from weighed sample by using the Dean-Stark extraction method of boiling toluene and collecting condensed fluids. The samples are then dried in an oven while the volume of extracted oil is calculated from the sample weight loss and amount of water collected. A vacuum oven is used to ensure that the kerogen in the sample does not oxidize during the drying and extraction process which can alter the weight of the sample. Using a Boyle's law device, the grain volume of a dried shale sample can be measured with helium. Porosity, pore volume and saturation measurements are then derived from the bulk and grain volume. Gas permeability is obtained using unsteady state gas pressure decay method

due to significant Klinkenberg effect in tight rocks. Summary of crushed rock analysis is shown below. As-received (A-R) bulk volumes and densities were determined from intact core samples before the samples were crushed for the rest of the analysis.

Table 4.1: Summary of crushed rock analysis results

Sample	M. Depth ft	$\rho_{B_{A-R}}$ g/cm^3	$S_{g_{A-R}}$ %	$k_{decay_{A-R}}$ md	$\rho_{B_{Dry}}$ g/cm^3	$\rho_{grain_{Dry}}$ g/cm^3	$\phi_{Helium_{Dry}}$ %	$k_{decay_{Dry}}$ md
1-1	12337.2	2.64	1.9	6.89E-4	2.62	2.71	3.3	1.05E-3
2-2	12681.0	2.66	21.6	2.56E-4	2.65	2.73	3.2	3.02E-4
1-11	12442.6	2.54	5.1	2.55E-3	2.52	2.70	6.7	3.11E-3
1-28	12461.4	2.57	3.8	1.48E-3	2.55	2.70	5.7	2.55E-3
2-19	12512.2	2.57	4.1	1.06E-3	2.53	2.73	7.2	5.93E-3
3-9	12815.5	2.66	1.5	7.33E-5	2.65	2.71	2.6	6.14E-4
3-23	12830.4	2.43	8.7	1.58E-3	2.41	2.68	10.1	3.75E-3
3-42	12852.1	2.37	10.3	5.14E-3	2.35	2.67	11.8	7.47E-3
3-53	12864.4	2.57	4.7	1.28E-3	2.55	2.71	5.6	4.34E-3
3-55	12868.2	2.46	4.2	1.04E-4	2.44	2.59	5.9	1.78E-3
3-62	12874.5	2.64	1.9	2.12E-4	2.62	2.73	4.0	5.35E-4
3-66	12879.4	2.64	2.0	5.06E-4	2.62	2.72	3.8	5.38E-4
3-74	12888.4	2.66	0.2	1.97E-6	2.64	2.70	2.3	1.78E-4
Average		2.57	3.8	1.15E-3	2.55	2.70	5.6	2.47E-3

The relationship between permeability and gas saturation/porosity is shown in Figure 4.14. The blue line represents the "as received" values whereas the red line denotes the dried samples.

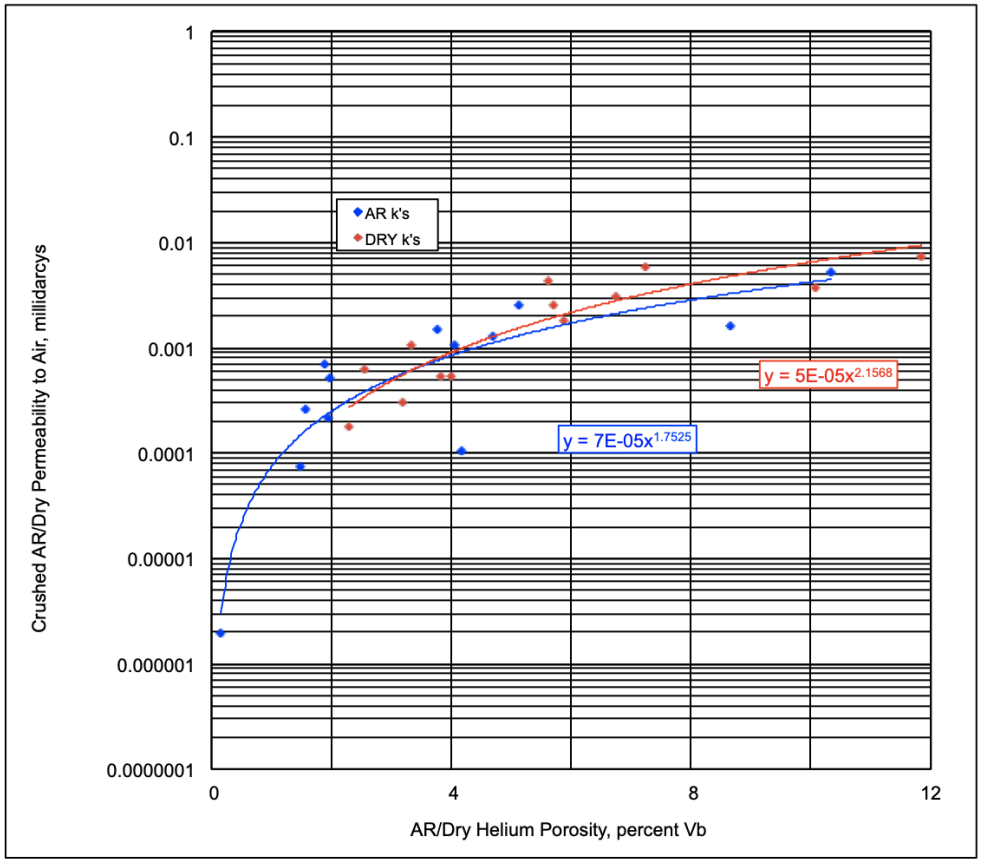

Figure 4.14: Permeability versus porosity.

Lithoscanner and GEOFLEX data has been obtained to analyze the mineralogical composition of the formation. The Tuwaiq interval is characterized of having high TOC values (5-6%) compared to Hanifa (average 1.4%). This also coincides with higher uranium content on spectroscopy logs and acoustically higher resistivity readings. A representation of the mineral composition of the samples is shown in Figure 4.15.

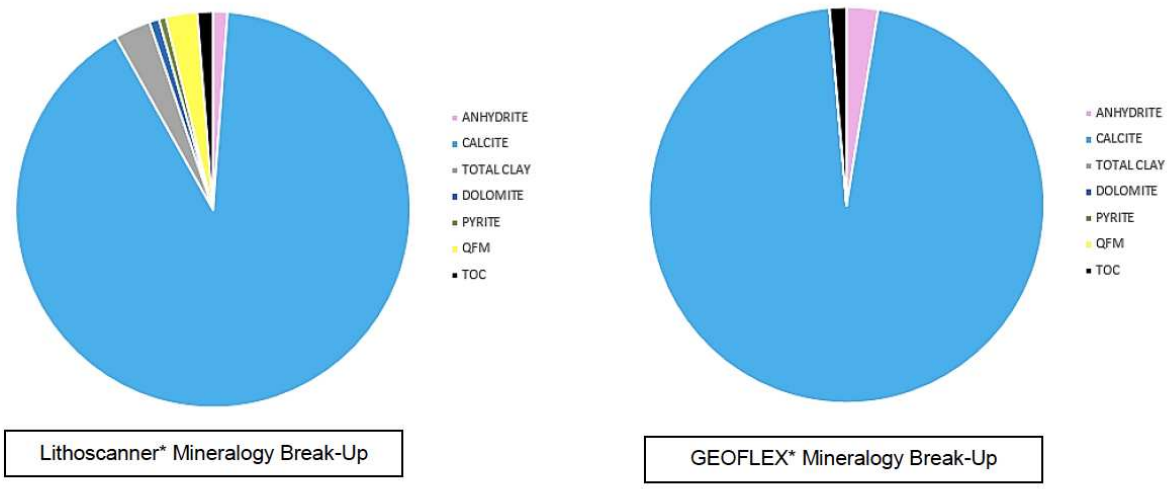

Figure 4.15: Mineral composition.

Total Organic Carbon is a critical parameter when evaluating the potential of a sources rock. As the name suggests, it is the total carbon present comprising of organic matter that includes kerogen and hydrocarbons. TOC is obtained from interpreting logs (spectral gamma ray, direct Lithoscanner carbon measurements, NMR). It is important to make the distinction between inorganic carbon and organic carbon when determining TOC as shown in Figure 4.16. Total inorganic carbon is calculated from other elements. The best method for inferring TOC from logs is usually determined once the values are compared to core measured TOC.

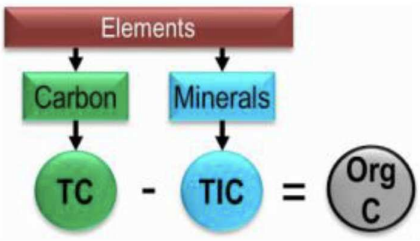

Figure 4.16: TOC breakdown.

The NMR method uses density logs to calculate kerogen volume and CMR to measure total porosity which provides distinction between bound and free fluid porosities. CMR porosity is sensitive to the volume of hydrogen in the fluids of the pore space but not the hydrogen in the kerogen. Since matrix density is known, density measurement is used to calculate pore volume. It is important to note that kerogen has a lower density than other mineral components in the source rock. This means the density measurements is sensitive to the amount of kerogen present (while CMR does not). This can be then used to calculate the volume of kerogen by using an estimated kerogen density of 1.4 g/cm^3. Equations 4.1 and 4.2 are used to calculate kerogen volume

$$V_{kerogen} = \frac{\rho_G - \rho_b}{\rho_G - \rho_K} - \frac{\phi_{NMR}}{HI_{PF}} \frac{\rho_G - \rho_F}{\rho_G - \rho_K} \tag{4.1}$$

$$TOC = V_{kerogen} \frac{\rho_K}{\rho_b CF} \tag{4.2}$$

where ρ_G is the matrix density without kerogen; ρ_b is the bulk density; ρ_K is the kerogen density; ρ_F is the density of the fluid; ϕ_{NMR} is NMR total porosity; HI_{PF} is the hydrogen index of the pore fluid (set to 1) and CF is the conversion factor (0.83) to account for the different elements (hydrogen, sulfur, oxygen and nitrogen) found in kerogen that are not carbon.

The log in Figure 4.17 shows the computed TOC of the interval. These calculations are then compared to logs derived from XRF (X-Ray Fluorescence) as shown in Figure 4.18. TOC values higher than 1% were flagged (good source rock potential) and two zones with a thickness of 140 ft were identified. One zone is in the lower section of the Jubaila formation and the second one in the upper section of the Hanifa formation. Both zones are correlated with enrichment of copper, sulfur, nickel and molybdenum indicating anoxic environmental deposition. The TOC is comprised of a carbon non-volatile component signifying kerogen presence and carbon volatile indicating presence of light oil.

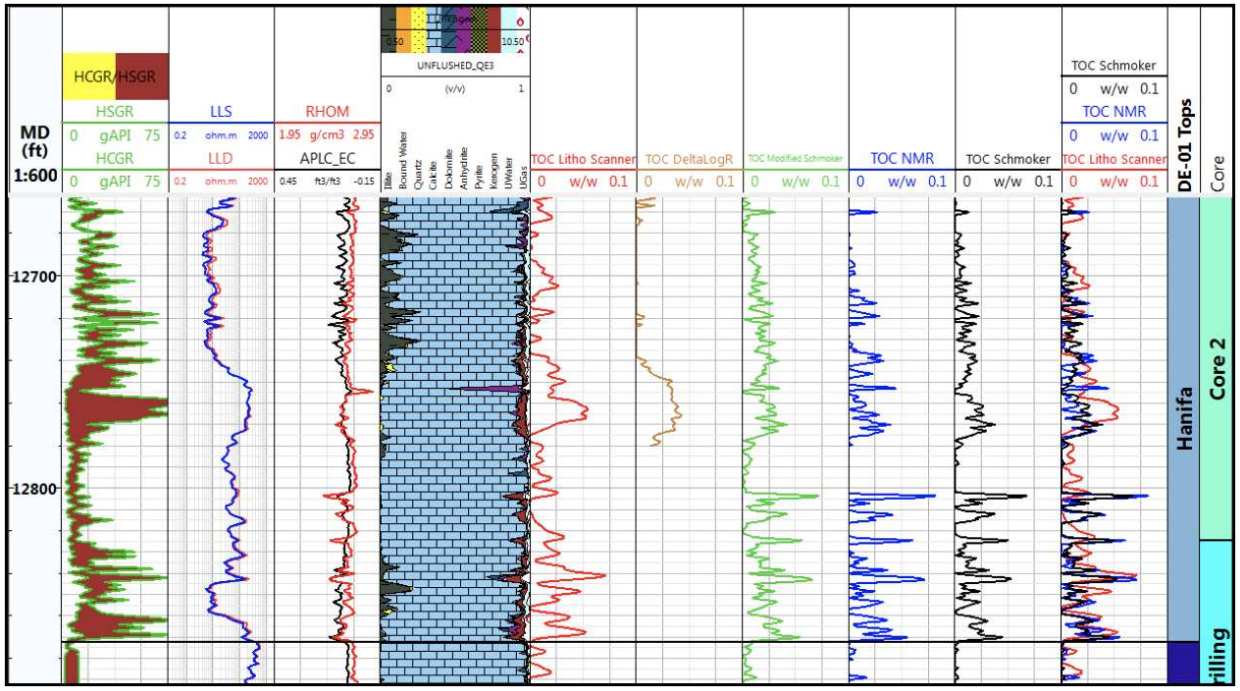

Figure 4.17: TOC calculation log.

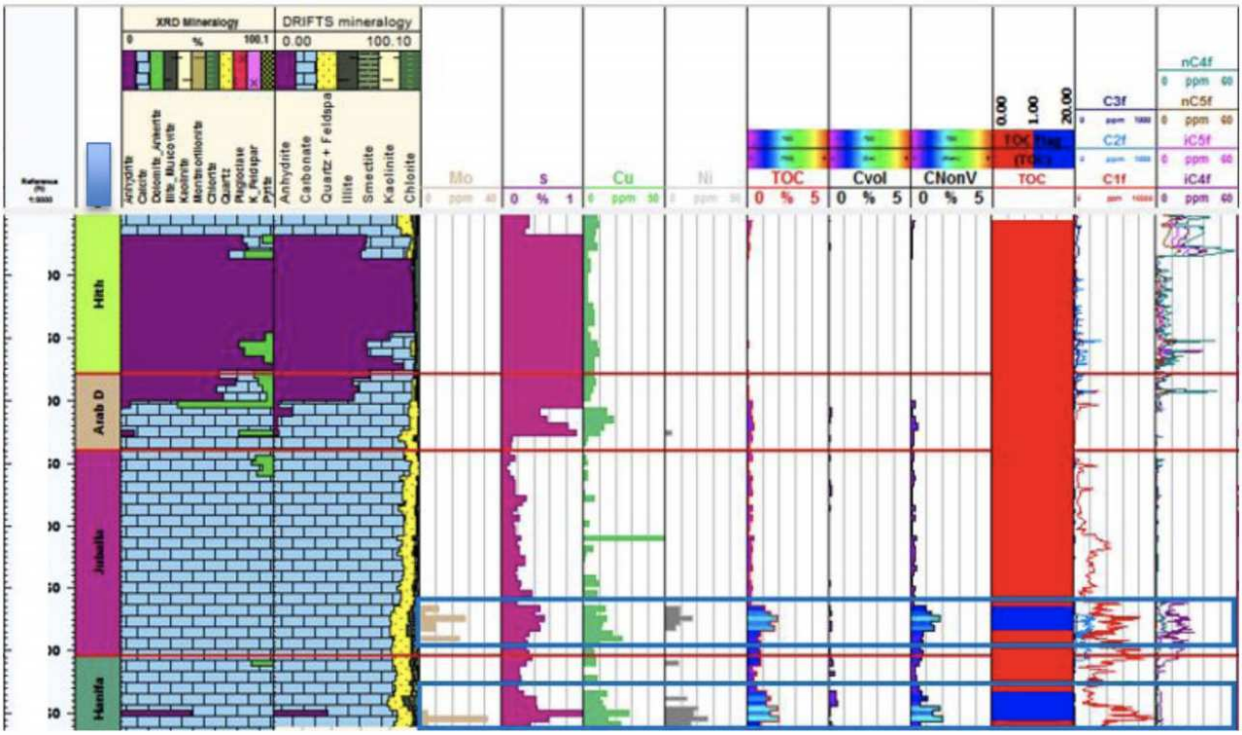

Figure 4.18: Geochemical composite log used to identify the main source rock intervals of the Diyab Formation (Vahrenkamp et al. 2015).

As previously discussed, determining porosity and pore fluids is a challenging task when dealing with unconventional formations. This is especially true in liquid-bearing shale formations. Since kerogen has a nuclear log similar to conventional pore fluids, erroneous quantification of TOC can lead to hugely inaccurate porosity estimates. Clay and bitumen presence can deteriorate reservoir quality especially in less mature reservoirs. The figure below illustrates the different formation components of a typical unconventional reservoir and the required tools/measurements to quantify them.

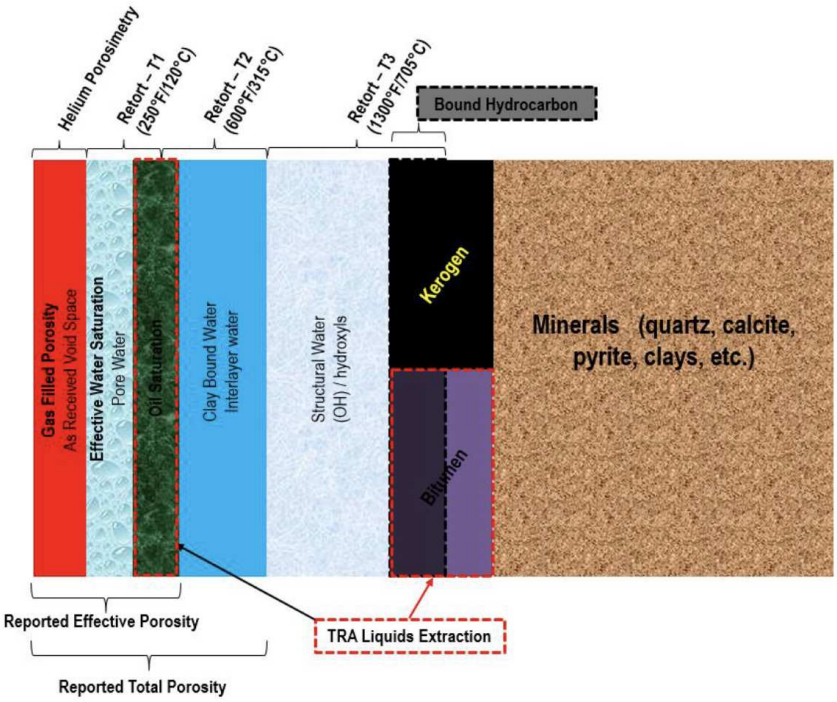

Figure 4.19: Typical formation components of an unconventional formation.

4.2.3 Gas-in-Place Estimation for Diyab Reservoir

Gas in source rocks occurs in a free and adsorbed state on the surface of organic matter. Both those values are important to quantify when estimating gas in place. Free gas and adsorbed gas exist in equilibrium at reservoir conditions. The Langmuir isotherm is used to

describe the state of equilibrium and can calculate the adsorbed gas in place for each reservoir section. The relationship between adsorbed gas and pore pressure is shown in Figure 4.20.

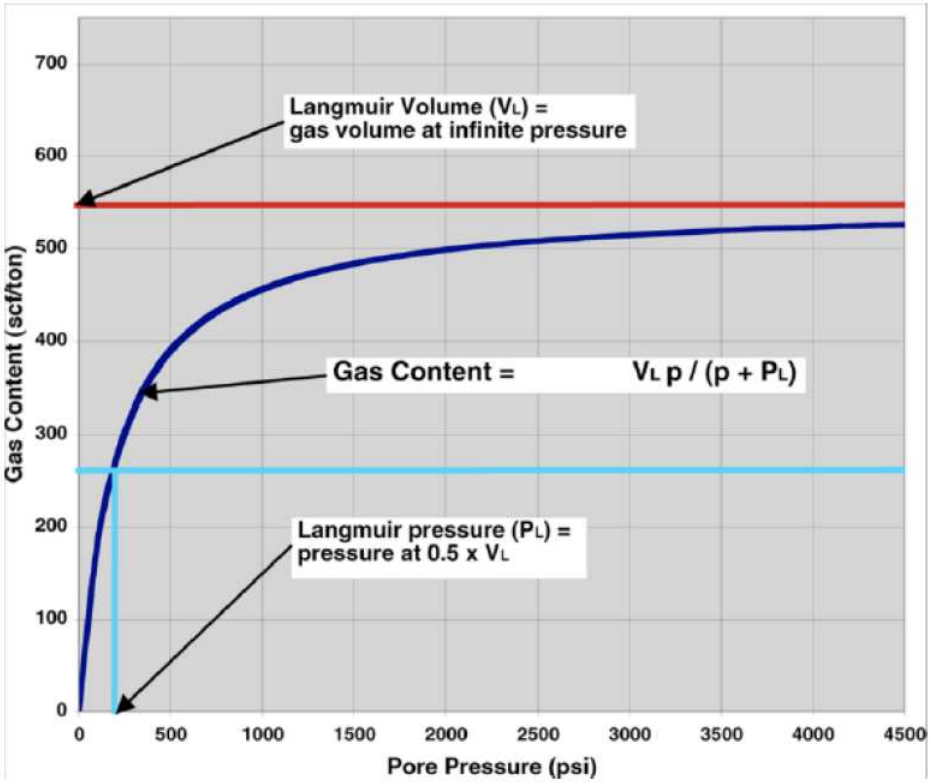

Figure 4.20: Langmuir isotherm for predicting adsorbed gas .

Gas-filled pore volume can be calculated from effective porosity and gas saturation data which is then converted to Standard Temperature and Pressure (STP). This is combined with the adsorbed gas estimates from about to calculate GIP as shown in Figure 4.21.

4.2.4 Geomechanical Characterization

A 1D Mechanical Earth Model (MEM) was created for the Arab D, Jubaila, Hanifa and Tuwaiq formations. MEM is a numerical representation of the stresses, pore pressure and the

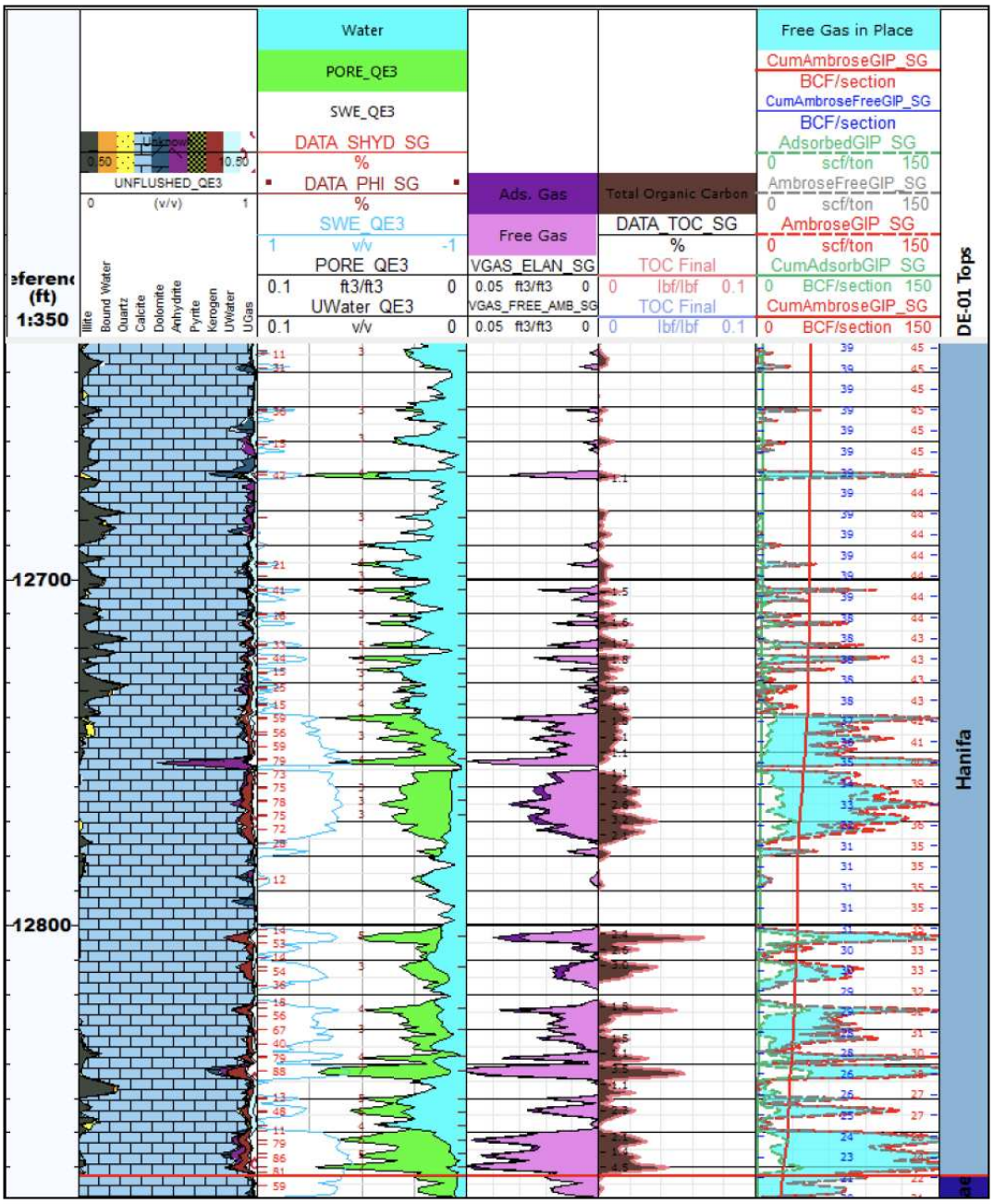

Figure 4.21: GIP estimation.

rock's mechanical properties for a reservoir. It basically contains all the geomechanical data analyzed that can be used for further geomechanical analysis and predictions such as hydraulic fracture design, wellbore stability analysis, sand production, compaction/subsidence evaluation and 3D stress modeling. Figure 4.22 illustrates the workflow used in creating the 1D MEM in order to ensure consistency and proper interpretation of the data. Compressional and shear velocity and bulk density data are the foundational inputs needed in constructing a 1D MEM. By studying the geomechanical data throughout the life of the field, we can better understand issues related to drilling, testing and production.

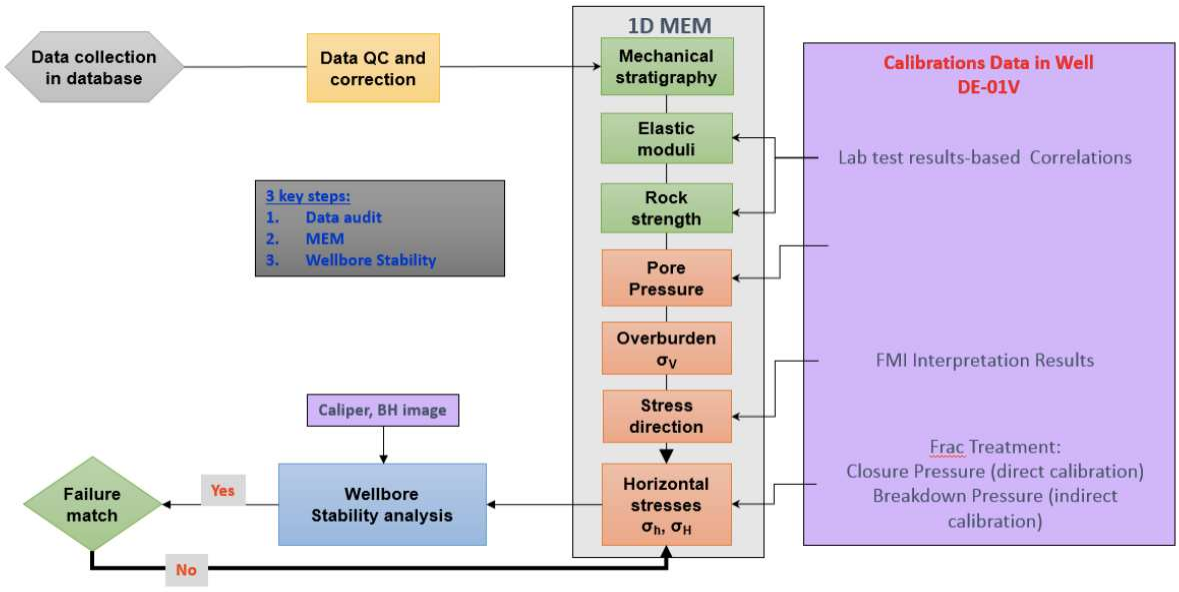

Figure 4.22: 1D MEM workflow.

Before direct geomechanical core testing, sonic log measurements are of critical importance since studying the compressional and shear logs allow the estimation of the rock's mechanical properties. Mechanical moduli can be calculated using the equation discussed in the geomechanics chapter. It is worth noting that since the process of wellbore deformation/failure is relatively much slower than the process of high frequency wave propagation

used in logs, it is imperative to get static (in-situ) measurements for wellbore stability analysis.

In lieu of core data, the static mechanical properties, Unconfined Compressive Strength (UCS), tensile strength and internal friction angle were estimated using correlations ADNOC developed for a neighboring unconventional field despite the fact that the Diyab formation is deeper than the Shilaif formation. These values were later determined and validated from our tri-axial experiments using the provided core samples. It was observed that rocks up to 12,300 ft depth were strong (dynamic Young's Modulus is in the 9-20 Mpsi range with rock strength above 18,000 psi). The rocks however became weaker below 12,300 ft (dynamic Young's Modulus is in the 5-8 Mpsi range with UCS around 13,000-16,000 psi). The can be observed in Figure 4.23.

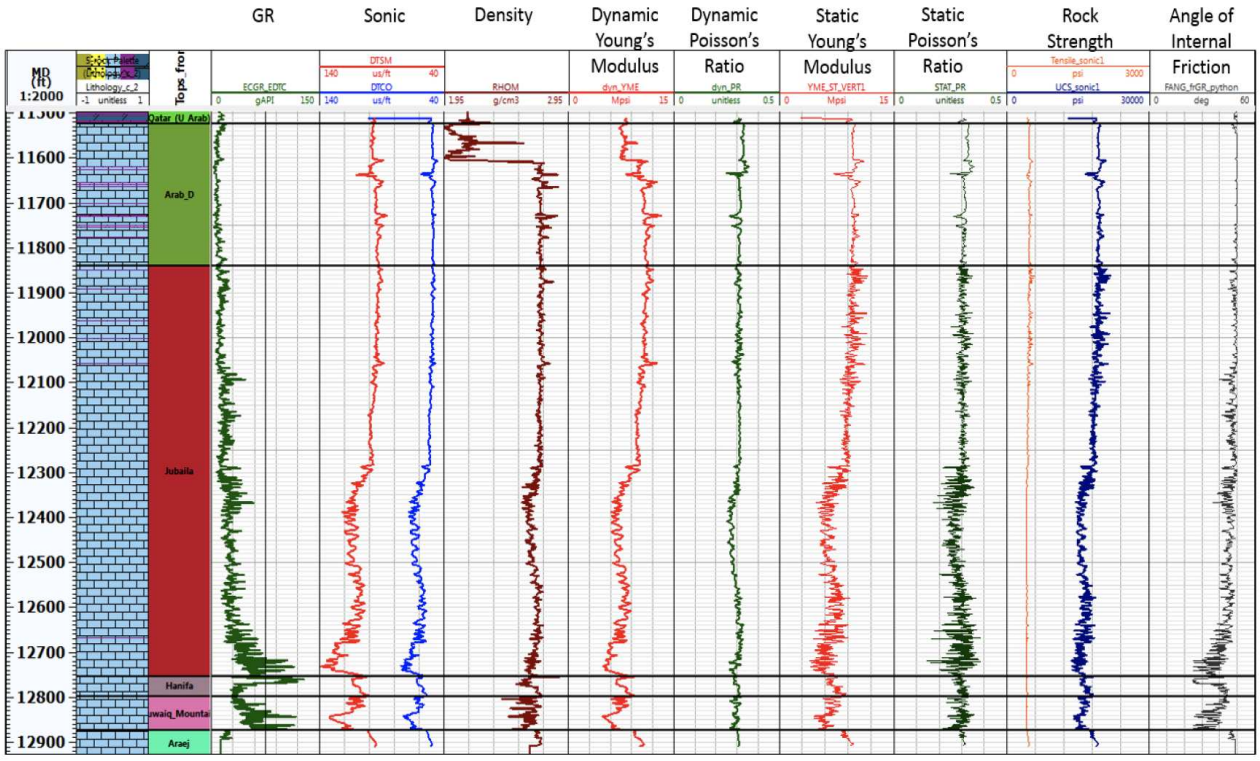

Figure 4.23: Elastic and geomechanical properties.

CHAPTER 5
EXPERIMENTAL INVESTIGATION

This chapter summarizes the experimental facility design and development. Details of core preparation, experimental procedure, data acquisition and interpretation are presented in this chapter.

5.1 Experimental Facility Design

The first experimental objective is to measure ultrasonic compressional and shear wave velocities of the shale sample and observe changes to the wave signature as capillary condensation occurs. This can be tested using a high-pressure triaxial compression cell. Bui and Tutuncu (2015) noted that acoustic velocities and elastic moduli of the pore fluid are higher when capillary condensation occurs. This change should be observed as increase in compressional wave velocity. The core samples will be tested will increasing pore pressure until capillary condensation is observed.

High capillary pressure within the nanopores in partially saturated shale samples strengthens rock grain contacts thereby increasing both shear and compressional wave velocities. This is triggered when we observe an excess adsorption of pore fluid by acquiring the syringe volume change. Figure 5.1 illustrate the triaxial testing system available at Unconventional Natural Gas and Oil Institute (UNGI) Coupled Geomechanics Laboratory at Colorado School of Mines. The facility can handle stress and pore pressure up to 10,000 psi with temperature up to 100°C. The facility allows precision control of temperature.

The experimental set-up used for this study is capable of the simultaneous acquisition of coupled stress, strain, resistivity, acoustic and flow data using LabView. The main components of the set-up are triaxial load cell, pore fluid injection system, back pressure system, vacuum system, axial and confining pressure system and a temperature control system. The tri-axial load cell holds the 1.5 inch diameter core sample within a rubber sleeve. The axial

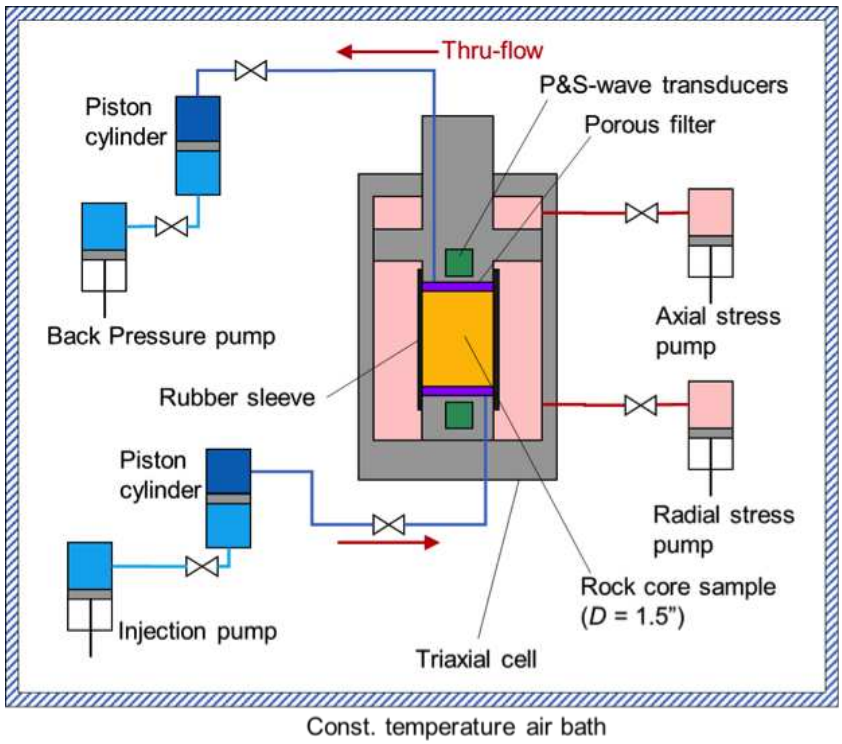

Figure 5.1: Schematic of the tri-axial system designed in this study.

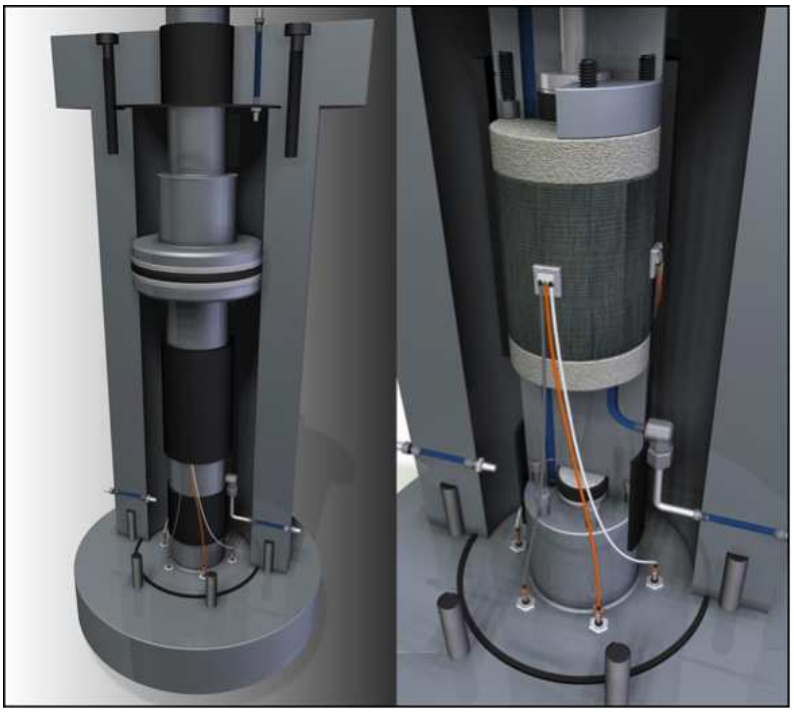

Figure 5.2: Internal view of tri-axial compression cell.

and confining pressure system is capable of simultaneously applying overburden pressure (axial) and isotropic radial stress (confining pressure).

The apparatus also encloses feed-through holes that allow electronic instrumentation and hydraulic lines to pass through its walls while maintaining its pressure integrity. The top cap houses a symmetric porous filter followed by a single hydraulic line connected to a pressure transducer, which allows continuous measurement of pore pressure at the sample top while fluids are circulated. A more detailed diagram of the apparatus and its assembly is shown below with blue solid lines denoting stainless steel pressure pipes, dashed green line denoting non-conductive high pressure pipe and purple dashed line denoting low pressure pipe used for the vacuuming.

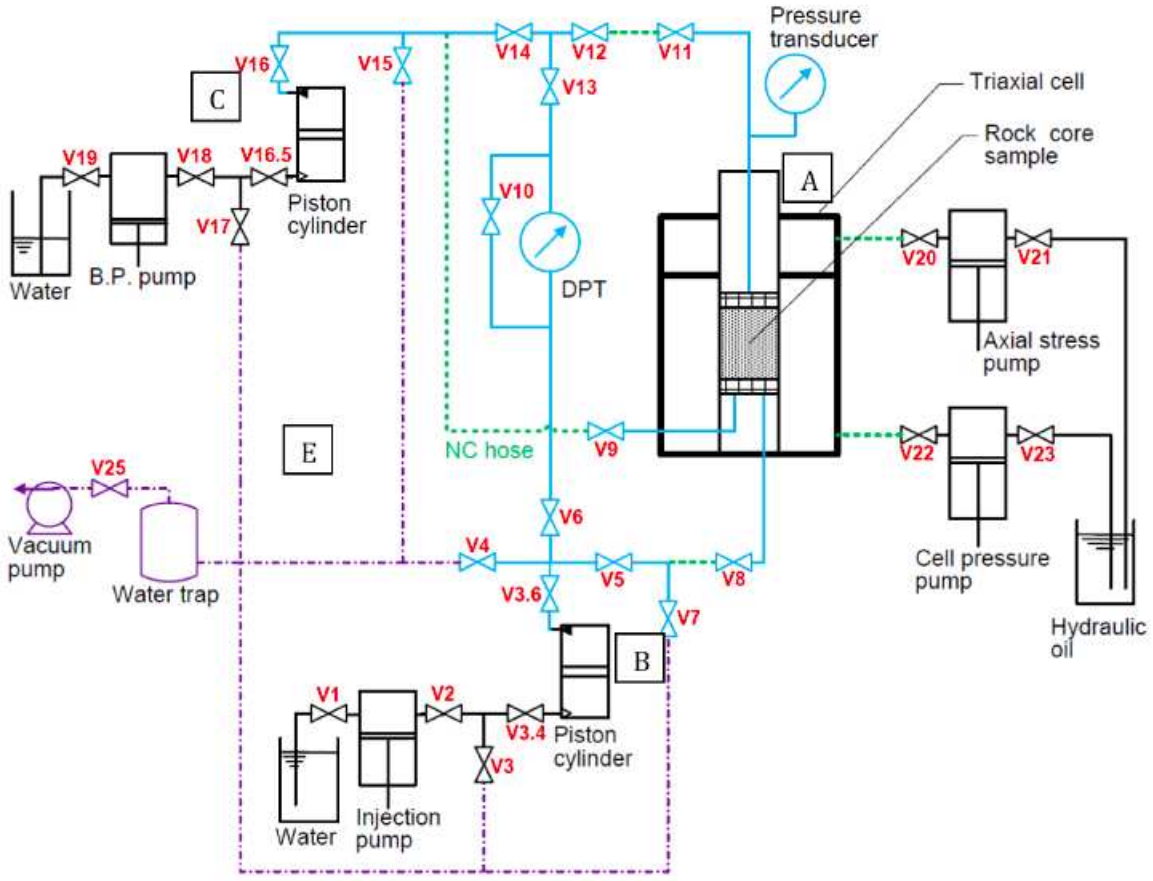

Figure 5.3: Schematic diagram of the experimental facility.

5.2 Core and Sample Preparation

The core samples had to be meticulously treated before they could be loaded up into the cell. It is important to point out that both sides of the cylindrical cores used in this study were parallel, smooth and flat to 0.001 inch tolerance for any given length measurement across the core. This set up is to ensure that the core can lie perfectly flat against the cell's piston to ensure effective ultrasonic wave propagation without interference. Otherwise, the wave will not conduct effectively through the sample and not yield a clear waveform. This was done manually by sanding the cores down since the use of equipment like a lathe would create fractures on the surface.

Tight sidewall core samples from the Austin Chalk and Diyab formations were used for tri-axial testing. However, the tighter the sample, the longer the saturation time period that is required to reach equilibrium. Our experiments typically run for 1000 hours per experiment including cell assembly. Table 5.1 summarizes the dimensions and general information on the cores successfully tested in this study.

The TQ-01 and TQ-02 core samples are from the Tuwaiq formation of the Diyab unit. It is a tight limestone, mudstone mainly, that is dark grey to black in color. It is highly carbonaceous with no visible natural fractures. Figure 5.4 and Figure 5.5 are pictures of the core samples obtained from the Tuwaiq formation and the slab it was cored from.

The AC-01 sample is from the Austin Chalk is from Crabb Ranch in Gonzales county, Texas. It is light grey in appearance and visibly laminated (layered with marls). Some microfractures are present with anhydrite filling them.

Table 5.1: Overview of cores prepared for experiment

Sample	Unit	Mass (g)	Depth (ft)	Length (in.)	Width (in.)	V_{Bulk} ($in.^3$)	ϕ (%)	k (nd)
TQ-01	Diyab	201.52	12866	2.910	1.476	4.979	3-5	1-5
TQ-02	Diyab	109.7	12847	1.456	1.480	2.506		
AC-01	Austin Chalk	90.27	8996	1.223	1.474	2.090	5	5-20

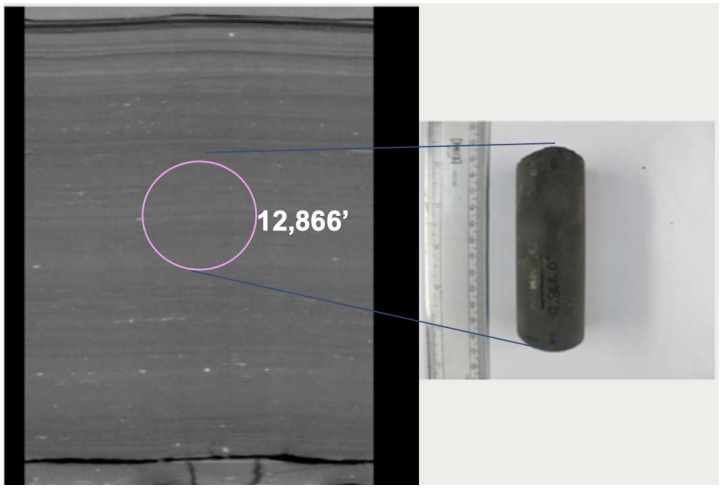

Figure 5.4: Tuwaiq core sample, TQ-01 at 12,866 ft.

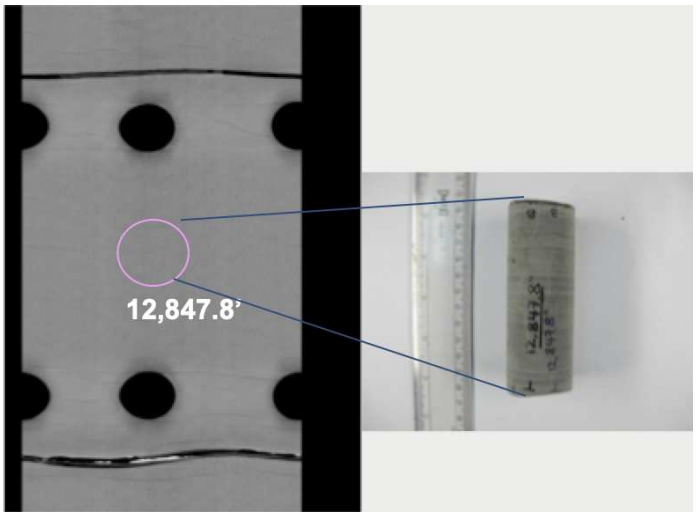

Figure 5.5: Tuwaiq core sample, TQ-01 at 12,847 ft.

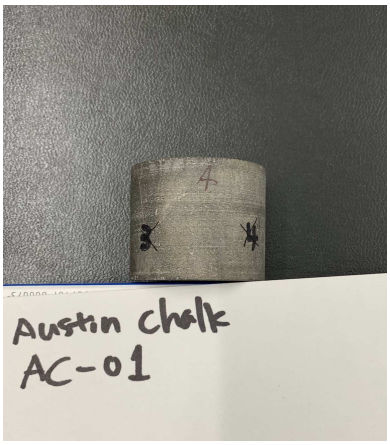

Figure 5.6: Austin Chalk core sample.

A Soxhlet extractor is used to decontaminate the cores in case they got in contact with any organic matter during the preparation process. A schematic of the Soxhlet set-up is shown in Figure 5.7. The bottom round flask is filled with toluene which is heated util it evaporates. The evaporated toluene rises to the top of the set up through a distillation arm where cool water is circulated (condenser). The cool water causes the toluene to condense and precipitate into the chamber that houses the core sample. This chamber slowly fills up over time as more toluene is condensed into it. When the chamber is full, it is emptied by siphon to the lower round flask that is being heated. This cycle is repeated for a few hours to a day. The sample is then dried in an oven to completely remove the excess toluene.

5.3 Evolution of Experimental Process

Various experimental set-ups were tested before a final set-up was finalized based on the following criteria:

- Clear waveform propagation across the core and entire tri-axial set-up.
- Ensuring the core does not get contaminated with confining or coupling fluids.
- Preventing any gas or mineral oil leaks in the pore pressure network, confining pressure system or the tri-axial cell.

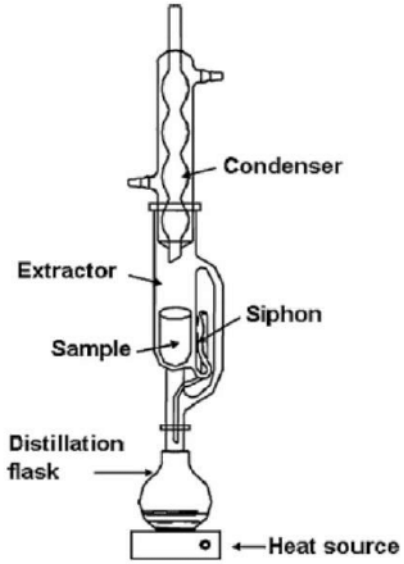

Figure 5.7: Soxhlet extractor schematic (Nojabaei et al. 2013).

The tri-axial set-up was modified to accommodate both 1 and 1.5 inch core plugs. The cell's pistons are 1.5 inch in diameter so 1.5 in core samples could be readily used. However, for 1 inch samples, two brass connectors were lathed so that they can be attached to the piston head. The base of the connecter is a 1.5 in disk (to be set to the piston) with a 1 inch diameter cylinder on top of it (that can accommodate the smaller cores). These disks had to be perfectly flattened and smoothed to prevent any disturbance to the acoustic waves passing through. We previously worked on 1 inch tight sandstone samples from the Codell formation (Dome Franks). Those results are not included since we had difficulty in wave propagation calibration.

The effectiveness of the coupling fluid is another important parameter that affects wave propagation . In order to guarantee no gap exists between the core and the cell's pistons, a coupling fluid was used. This will ensure wave propagation throughout the set-up (piston to piston). However, it is also important for the coupling fluid not to get in contact with the core sample which would result in its contamination. Several coupling fluids such as honey, glue and different types of epoxy were used and wave conductivity across the core was tested. After finding the most optimal fluid (water-proof epoxy), we ensured the coupling fluid does

not get in contact with the core. The answer to this problem was to apply conductive copper tape to the sides of the core before applying the epoxy which secures it to the piston.

Several assembly methods were investigated with the aim to improve the epoxy application/bonding. Although the epoxy has to be left for 24 hours to set, the first 10 minutes of mixing the resin with the hardener are the most critical. Epoxy is first applied to the interface between the bottom piston and the core. The cell is then assembled with the top piston finally vertically-lowered into the cell with the epoxy to set on the top part of the core. It is important to note that weight/pressure has to be added when epoxy is applied to ensure it pushes out any air bubbles/gap between the piston surface and core to ensure wave propagation.

We initially tried flattening stainless porous disk filters that would be placed above and below the core to distribute gas flow. However, the disks interfered with wave propagation and another solution had to be found. In order to facilitate gas flow and maximize adsorption, a 1/16" hole is drilled at the bottom of each core and another hole is drilled from the lower side to connect to the first hole. This creates a corridor for the gas to flow through. It is important to ensure the core's surface is still perfectly flat and smooth after the drilling process and that the hole is free of any debris that restricts the flow of gas. The bottom hole is aligned with the pore pressure tube. Once this is done, the core is wrapped up in a porous blanket before being taped. The porous blanket is to allow the gas to move freely on the core's outer surface and maximize adsorption area. The outer tape is used to ensure the blanket is held tightly against the pore and it is isolated from possible contamination. Figure 5.8 illustrates the final experimental set-up.

5.4 Experimental Procedure

A core sample is encased within a neoprene rubber sleeve and then confined axially and radially using metal pistons and cell fluid pressure. High-pressure syringe pumps control the axial and radial confining stresses. Both top and bottom axial pistons are equipped with 1 MHz frequency compressional (P) and shear (S) wave transducers. Pore pressure at both

end surfaces are individually regulated by two syringe pumps. The injected pore volume is measured from the change in syringe volume of individual pore pressure pumps.

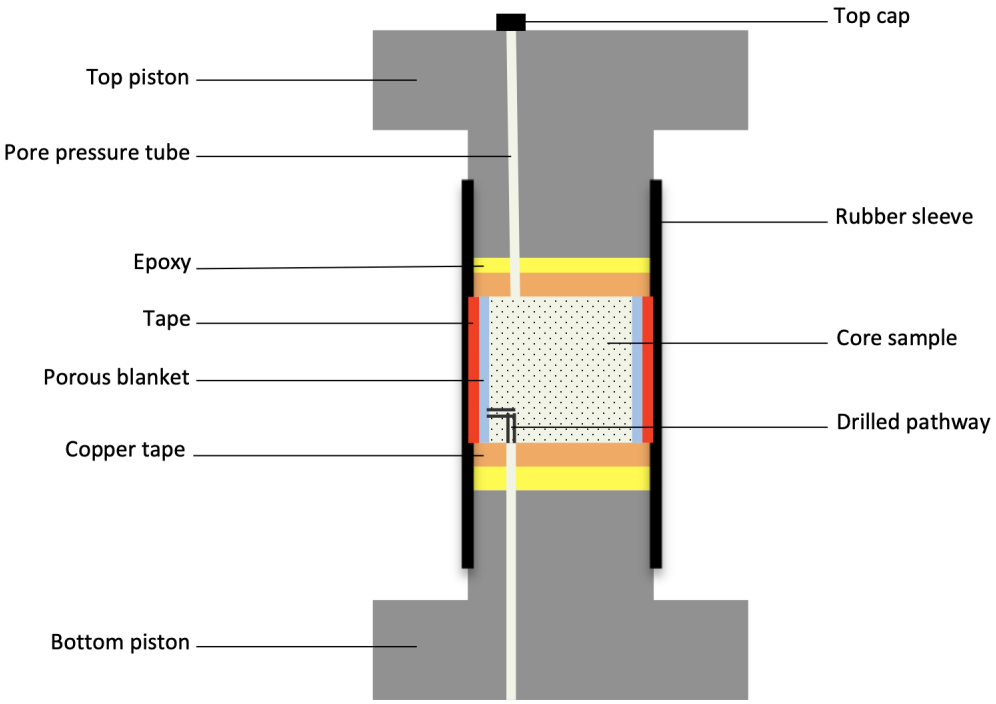

Figure 5.8: Tri-axial cell schematic.

A serial digital communication protocol acquires and transfers pressure and syringe volume data from pump controllers. The system temperature fluctuation is 0.1°C at a given experimental temperature which ensures reliable high-quality data due to minimal temperature disturbance since pore volume change due to capillary condensation is sensitive to temperature changes.

Figure 5.9 shows the critical radius at which pores condense at a given saturation pressure for CO_2 using the Kelvin equation. The smaller pores requires a lower saturation pressure to condense since the surface forces acting on the nanopore's surface are higher. Whereas, pores that are 20-40 nm in size, require 750-820 psi saturation pressure for the pore to condense. Bulk saturation pressure for CO_2 at 27°C is 977 psi. These values are important

when designing our experimental set-up to give us an idea on the pressure range that CO_2 will condense given a sample's pore size.

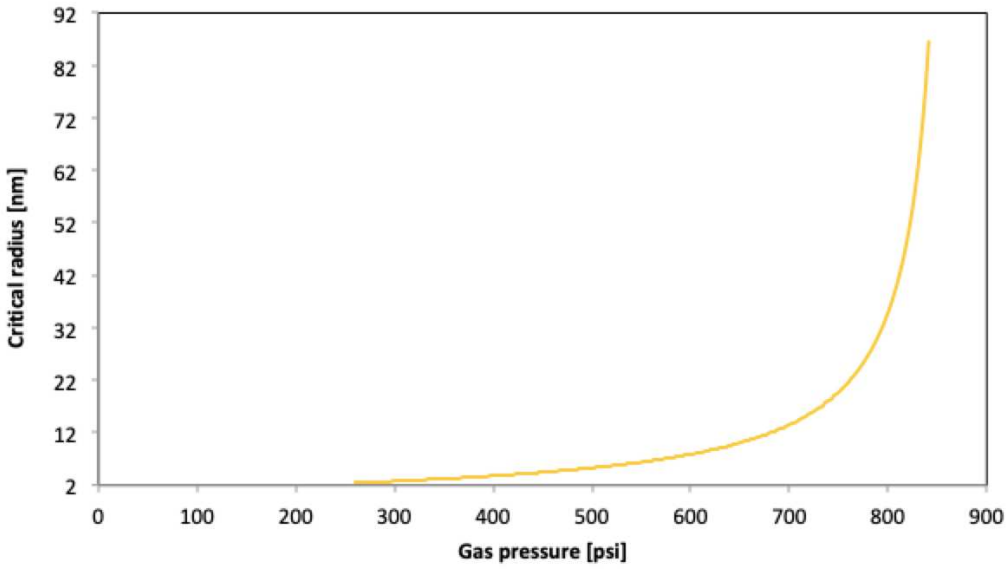

Figure 5.9: Critical radius versus pressure of carbon dioxide at 27°C.

Once a core sample is loaded into the tri-axial cell, the arrival times of compressional and shear waves across the core with increasing pore pressure (by injecting CO_2) are recorded and analyzed. In theory, acoustic evidence of CO_2 capillary condensation should occur at a pressure lower that bulk saturation pressure (977 psi at 27°C). Velocity is then calculated by coupling arrival analysis with strain gauge data that measures deformation across the core. The pore pressure is then increased at steady intervals while maintaining an effective stress of 100 psi at each step. Stress and strain data are also simultaneously recorded and analyzed to study the mechanical changes in the core.

5.5 Calibration

Before testing the core samples, we first had to calibrate the equipment using an aluminum reference sample. This sample was treated similarly to the cores described above (cut, lathed, leveled, smoothened) before being loaded up in the cell. The purpose of this

calibration is to measure the wave arrival time as it travels through the equipment. To visualize, the wave is emitted from a transducer and goes through the pistons, epoxy, copper tape before reaching the core first. It then has to go through another layer of copper tape, epoxy and piston before reaching the second transducer.

When measuring the arrival times of core samples, we will deduct this calibration value from our readings so we can accurately obtain arrival time of the core samples. The first step is to put the transducers against each other and record the arrival time between them. The next step is to put the dummy aluminum core sample alone between the transducers and record the arrival time. Finally, we load up the aluminum core as we would a core and then record the arrival times.

Table 5.2: Calibration data required to correct for actual wave travel time through the core

	P-wave velocity	S-wave velocity
t_{arr} Aluminum	12.07 μs	25.08 μs
t_{arr} transducer	440 ns	1.0 μs

The arrival times are calculated using Equations 5.1 and 5.2.

$$t_{arrival}(core) = t_{arrival}(recorded) - t_{arrival}(equipment) - t_{arrival}(tranducer) \tag{5.1}$$

$$t_{arrival}(equipment) = t_{arrival}(calibration) - t_{arrival}(aluminum) \tag{5.2}$$

CHAPTER 6

RESULTS AND DISCUSSION

"Whatever it is you're seeking won't come in the form you're expecting."

— Haruki Murakami, Kafka on the Shore —

The results of our findings are presented in this chapter. The results from nitrogen adsorption testing to characterize pore size distribution of our samples is discussed first. The summary of the theoretical model validation with the tri-axial experimental data and model prediction are presented next. Finally, I present the results showing the effect of capillary condensation on the mechanical and acoustic properties observed in our experiments.

6.1 Pore Size Characterization

Since pore size in conventional reservoirs is large, the volume of adsorbed gas is usually ignored since it is negligible compared to the larger portion of the bulk fluid. Unconventional reservoirs, on the other hand, have very small pore sizes leading to a high surface area to volume ratio. Therefore, the amount of adsorbed gas has to be accounted for since it is significant. The aim of this Chapter is to understand the adsorption behavior of the tested samples to quantify the pore size distribution and to understand the precursor conditions that lead to capillary condensation.

6.1.1 Nitrogen Gas Adsorption

In order to quantitatively measure pore volume and pore size distribution, nitrogen gas adsorption testing was conducted on crushed samples. Nitrogen is an inert gas that can be adsorbed, desorbed and condensed in both hydrophilic and hydrophobic pores. This makes it ideal for pore volume distribution purposes. The BET methodology described in the previous section is used. This procedure quantifies the molecular physical adsorption of gas

molecules on the sample's surface. The adsorption process is only influenced by pore size distribution while the desorption process is affected by connectivity as well (Mehmani et al. 2013). Therefore, the desorption isotherm is considered to be sometimes better at describing pore size distribution since it accounts for the pore throat structure. Table 6.1 summarizes the gas sorption data and the core depth intervals.

Table 6.1: Summary of nitrogen adsorption data

Sample ID	M. Depth (ft)	N_2 gas adsorption	
		Isotherm and Hysteresis Type	Mesopore BET Area $A_s(m^3/g)$
1-11	12442.45	II - H3	5.33
2-19	12512.55	II - H3	5.22
3-42	12852.45	II - H3	6.08
3-55A	12868.10	II - H3	28.36

It is important to first ensure the proper de-gassing of the adsorbent by exposing the sample to high pressure/high temperature vacuum to remove any water and other contaminants so that surface area can be accurately measured. The cell was also calibrated first by using a dummy non-reactive sample (aluminum sample) to account for the compressibility effect of the gas.

The sample is then placed in a glass cell with other glass rods to occupy the dead space in the cell. After degassing, the cell is moved to the analysis port. Liquid nitrogen is used to cool the sample and keep it at a constant temperature. The low constant temperature is to ensure that interaction between gas molecules and the surface of the sample are strong enough for measurable adsorption to be recorded. Nitrogen is then injected into the cell using a calibrated piston.

Since adsorption and capillary condensation are sensitive to temperature, the experiment is performed at constant temperature. Equation 6.1 is used to calculate the volume of sorbed gas:

$$\frac{1}{V_A\left(\frac{p_o}{p}-1\right)} = \frac{1}{V_M} + \left(\frac{C-1}{V_M C}\right)\frac{p}{p_o} \tag{6.1}$$

where V_A is the volume of the adsorbed gas, p is the pressure, p_o is the saturation vapor pressure, V_M is the volume of gas needed to cover the solid surface with a monolayer and C is the BET constant.

The IUPAC pore size classification that is used in this analysis to identify the different pore size classification is shown in Table 6.2. The standard isotherms for model materials with unique micro-structural characteristics is shown in Figure 6.1. Each isotherm displays observably different features that relate to the morphology of the micro-structures. This classification is later used in our pore size characterization.

Table 6.2: IUPAC pore size classification

Pore width	Description	MICP (MPa)
< 2 nm	Micropore	624
2 nm - 50 nm	Mesopore	> 25
> 50 nm	Macropore	< 25

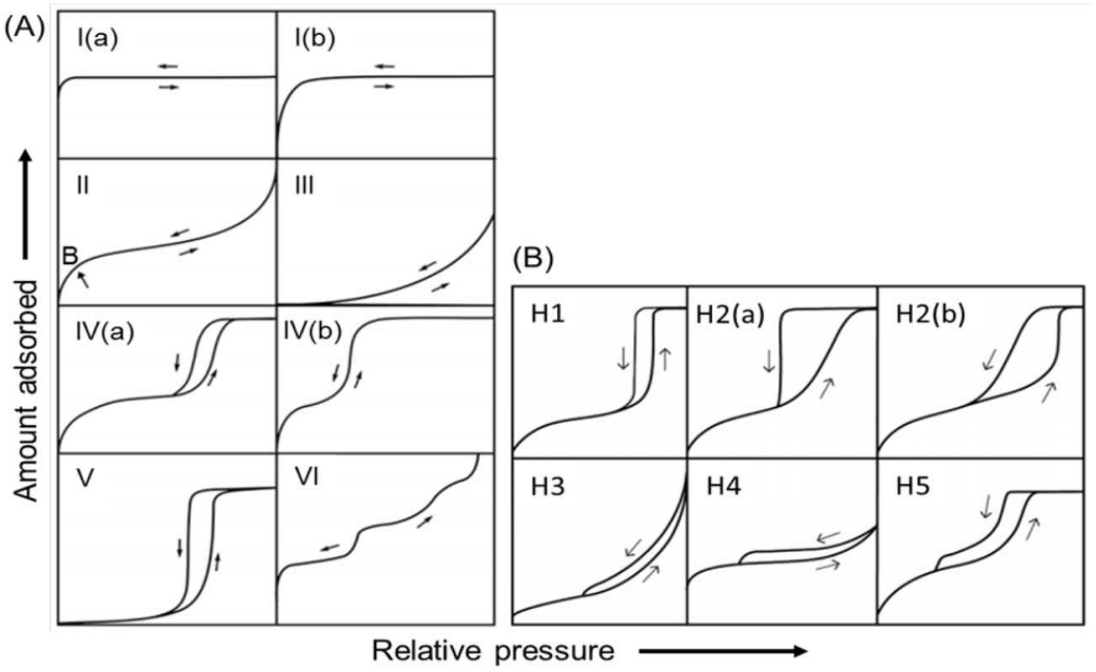

Figure 6.1: Classification of adsorption isotherm hysteresis (Gregg and Sing 1982).

At low pressure ($p < 0.3p_o$), a fraction of the analysis gas demonstrates increased residence time on the solid adsorbent. At this range, plotting the left hand side of the equation yields a straight line with intercept of $1/V_M C$ and a slope of $(C-1)/V_M C$. We can solve for C and V_M.

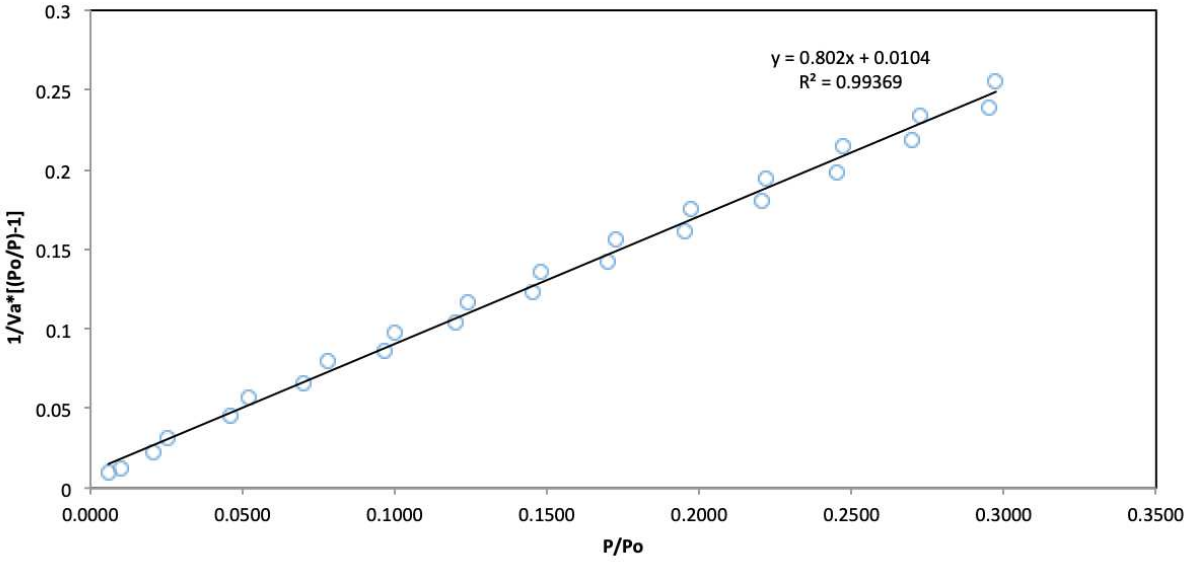

Figure 6.2: Straight line analysis for sample 1-11.

When the system reaches equilibrium, the adsorbed molecules form multilayers on the adsorbent. At around $\frac{p}{p_o} > 0.3$, the process of capillary condensation occurs. The conditions for this to occurs is defined by the Kelvin equation as previously discussed. It assumes the formation of a hemispherical meniscus in a cylindrical pore with radius r_p. Meniscus radius $r_m = \frac{2}{r_p}$.

Figure 6.3 to Figure 6.6 show the relation between volume of sorbed nitrogen and relative pressure for the four samples. The hysteresis observed in these figures show that during desorption, not all the nitrogen adsorbed can be released from the pores. It also shows the existence of a vast network of mesopores in the samples.

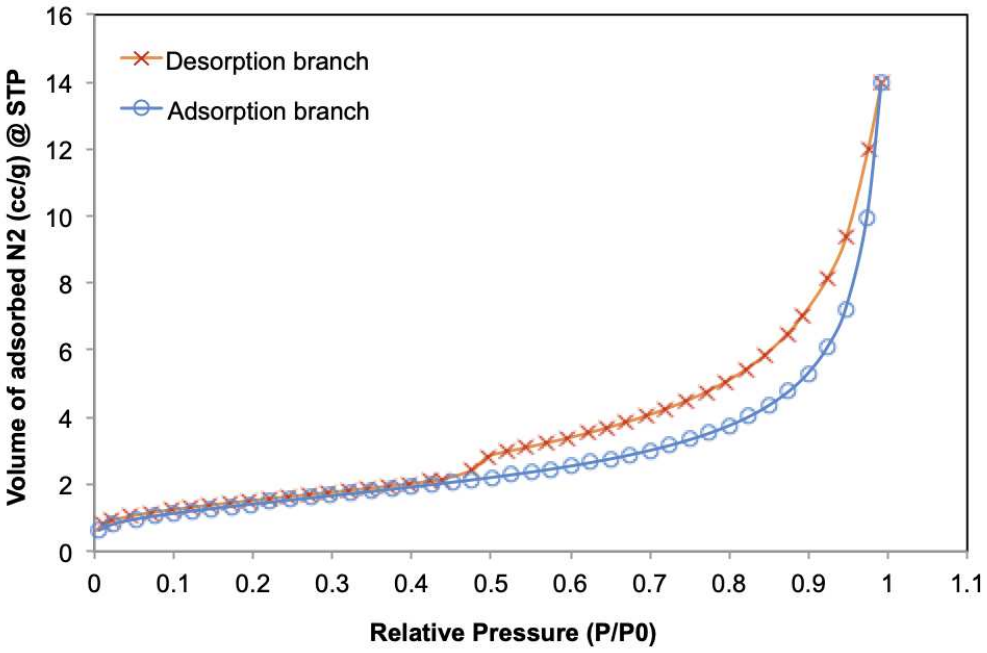

Figure 6.3: Nitrogen gas sorption for sample 1-11.

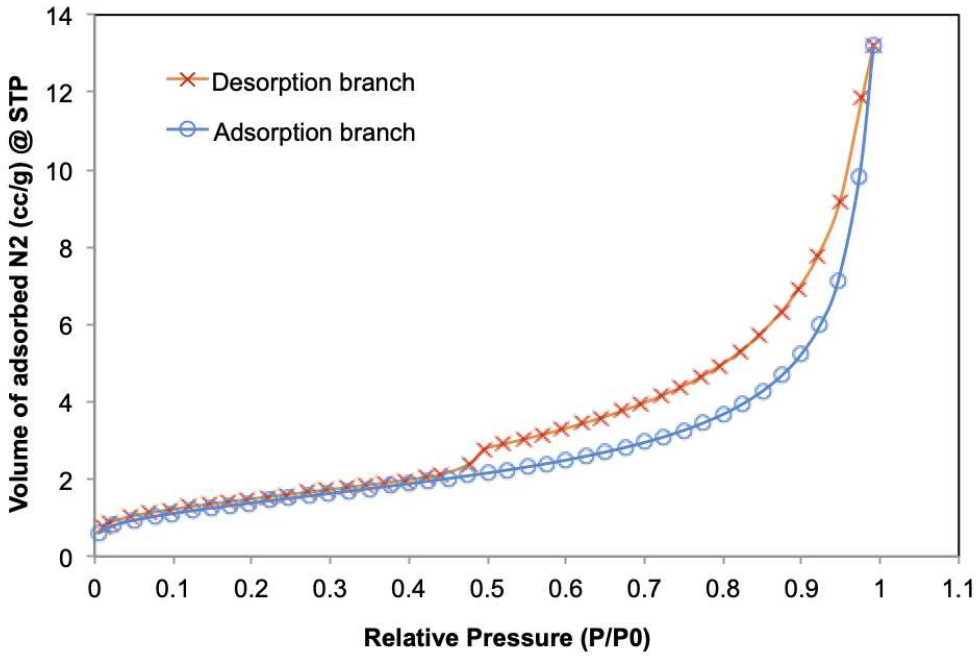

Figure 6.4: Nitrogen gas sorption for sample 2-19.

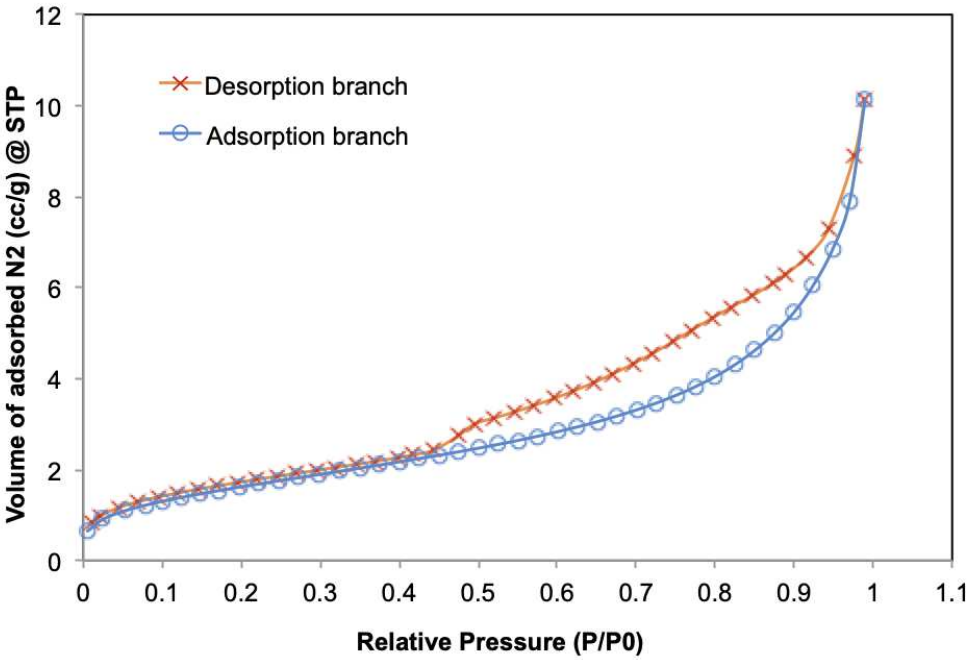

Figure 6.5: Nitrogen gas sorption for sample 3-42.

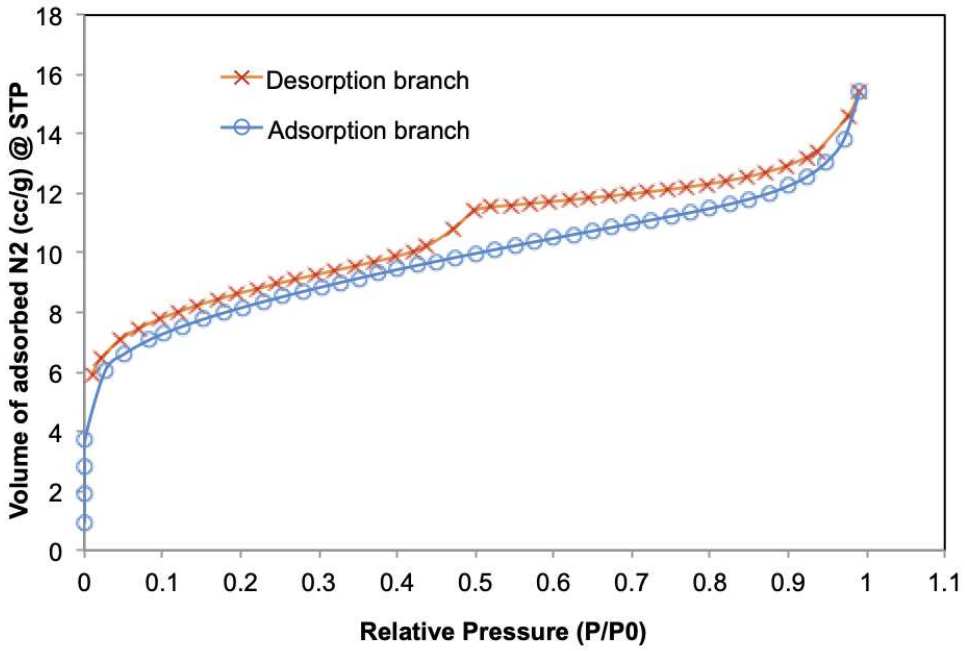

Figure 6.6: Nitrogen gas sorption for sample 3-55A.

Surface area is calculated using the cross-sectional area of a nitrogen molecule and V_M, which is obtained from the straight line analysis of the left hand side of the BET equation. Equation 6.2 is used to calculate specific surface area.

$$A_s = \frac{V_M N_A \delta_a}{22400} \tag{6.2}$$

where N_A is Avogadro's number; δ_a is the cross-sectional area of a nitrogen molecule, which is 0.162 nm^2.

The Kelvin equation is used to calculate the pore diameter at which condensation occurs for pores less than 200 nm wide. This is done by assuming the formation of a hemispherical meniscus in a cylinder pore of radius r_p.

$$\frac{1}{r_m} = \frac{2}{r_p} \tag{6.3}$$

where r_m is the meniscus radius.

However, for the purpose of BET adsorption, Equation 6.4 is used to calculate the pore radius using specific surface area.

$$r_p = \frac{2V_P}{A_S} \tag{6.4}$$

Non-Local Density Function (NLDFT) is used to calculate pore size distribution representing pore volume by given range of pore sizes. This method is based on statistical mechanics and assumes a surface and pore structure to characterize porous materials by calculating the electronic structure of a many-bodies system. Pores of different size are assumed to be of the same shape with each pore behaving independently. The process of pore-filling is controlled by fluid-fluid and fluid-grain interactions (capillary condensation). NLDFT differs from DFT by accounting for surface roughness. Assuming the adsorbent surface is homogenous, the derived energetic heterogeneity is then attributed to pore size distribution (Sing and Williams 2012). The relationship between surface area with pore pore diameter is shown in Figure 6.7 to Figure 6.10.

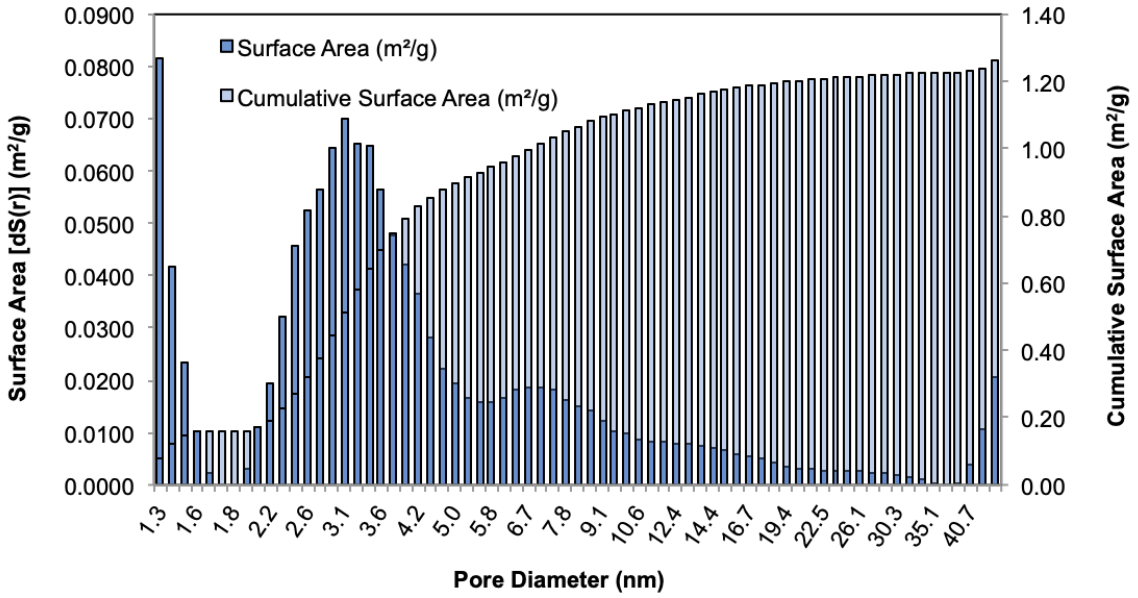

Figure 6.7: Relationship between surface area and pore diameter for sample 1-11.

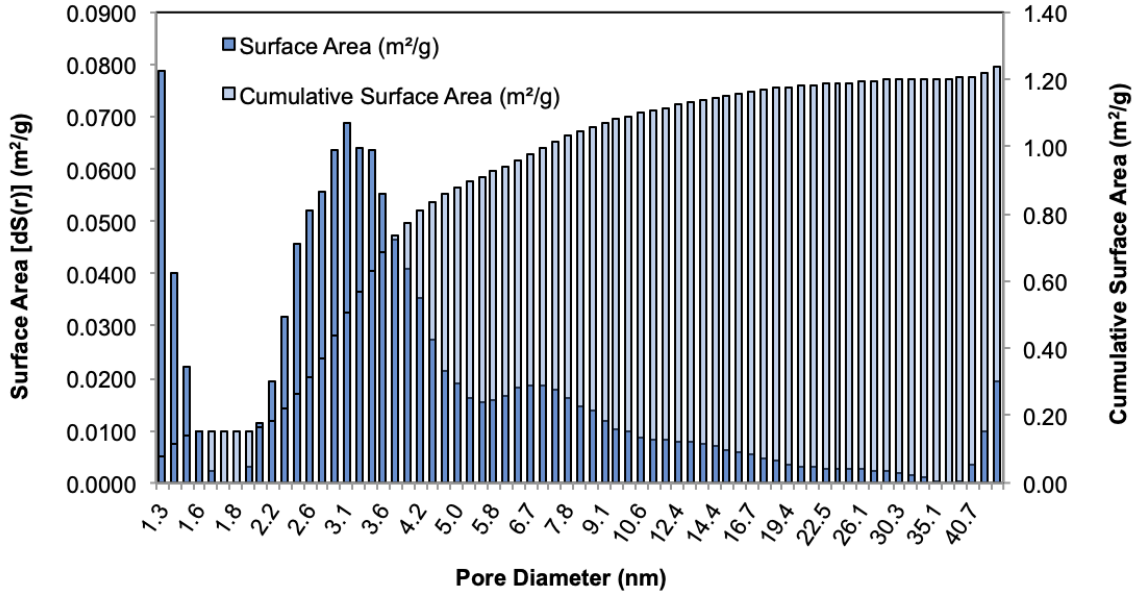

Figure 6.8: Relationship between surface area and pore diameter for sample 2-19.

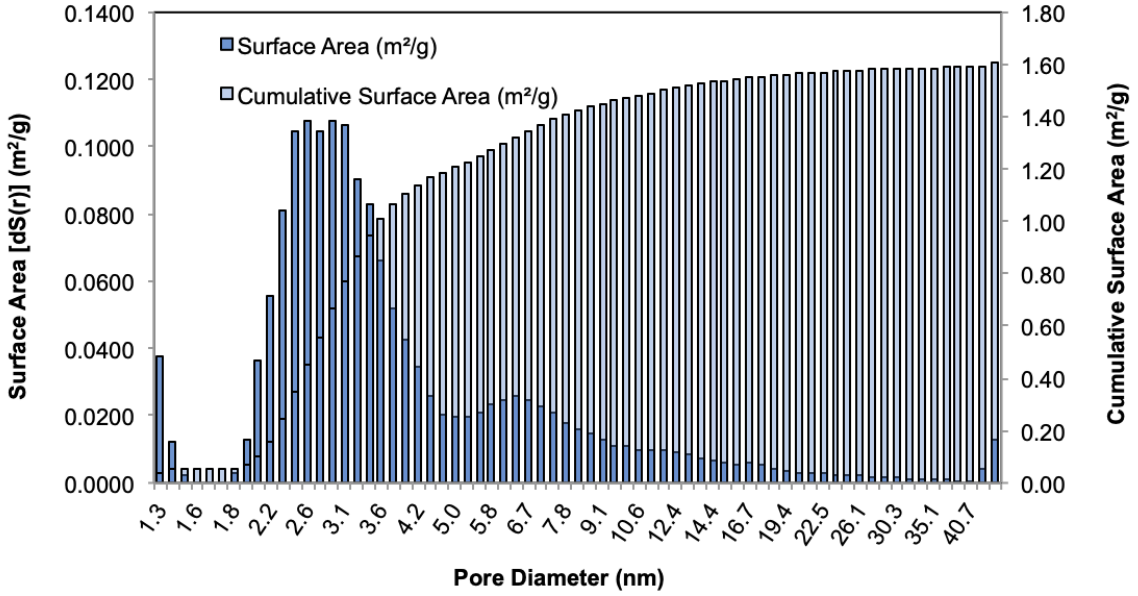

Figure 6.9: Relationship between surface area and pore diameter for sample 3-42.

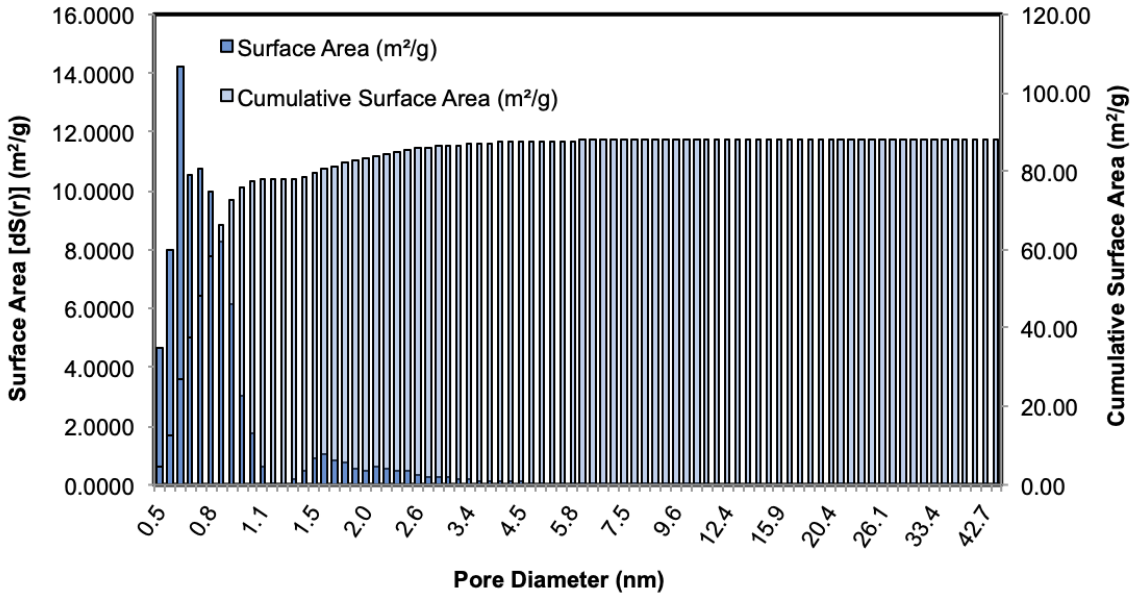

Figure 6.10: Relationship between surface area and pore diameter for sample 3-55A.

The pore volume V_P is determined from V_A below saturation pressure $\left(\frac{p}{p_o} \approx 0.995\right)$ using Equation 6.5.

$$V_P = \frac{V_M V_A p}{RT} \tag{6.5}$$

Using the adsorption isotherm model classification shown above, the shale core samples display Type II isotherm behavior indicating media with pores in all regime of size classification (micropores, mesopores and macropores). At low pressure, the inflection Point B indicated the end of monolayer adsorption and the start of multilayer adsorption. In order to determine BET A_s, data below Point B is analyzed whereas pore size distribution is determined above point B. Point B was used by BET as a point to denote the completion of the monolayer. The adsorption at Point B is equal to the monolayer capacity.

The hysteresis loop associated with type II isotherms is H3 and H4 indicating slit shaped pore geometry. The desorption behavior is similar to that of drying which involves penetration of the non-wetting phase. This behavior shows that when large pores are accessible through narrow throats, hysteresis occurs since the pore fills at a higher pressure that which it can be emptied (Gregg and Sing, 1991; Lowell et al., 2004; Thommes et al., 2015).

We observe that when the pore size distribution does not have a wide range (in the case of sample 3-55A), capillary condensation is observed at a wider range (wider range of relative pressure). Whereas in the three other cases, that window is reduced and starts at around relative pressure of 0.5. Also, since sample 3-55A has comparatively much smaller pores, interfacial tension forces are higher but the pore size is too small for any condensation or liquid to form inside.

Capillary condensation occurs when pores in the mesopore range condense. This process is secondary since it occurs as a direct result of multilayer adsorption on the pore walls. In these experiments, capillary condensation's signature is that of an upward deviation from the corresponding multilayer Type II isotherm with more condensation occurring at higher relative pressures. Macropores (>50 nm) condense only at high relative pressure.

The relationship between pore volume and cumulative pore volume with pore diameter is shown in the figures below. It is worth noting that samples 1-11, 2-19 and 3-42 have similar adsorption isotherms as well as pore volume/size distribution. Sample 3-55 has the narrowest pore size distribution with most pores < 4.5 nm. This can be expected by looking at the sample's adsorption isotherm which has the widest hysteresis loop that occurs early on ($p/p_o < 0.3$) and continues throughout. This signifies significant contribution from the micropores at that range before getting to the mesopore range.

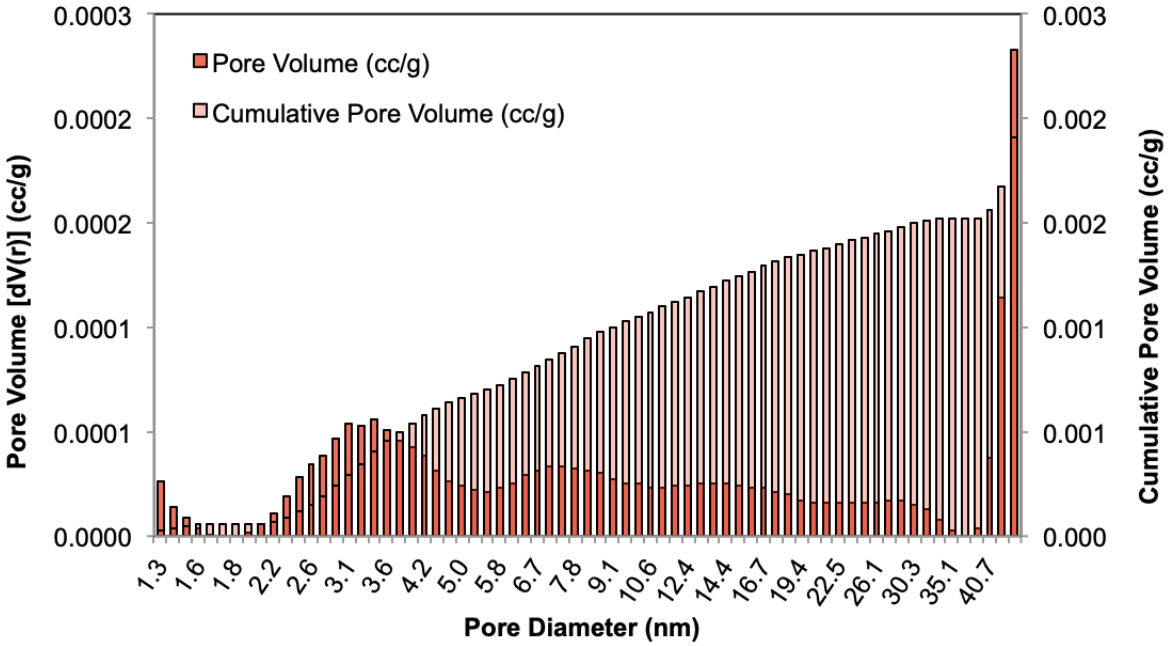

Figure 6.11: Pore volume versus pore diameter for sample 1-11.

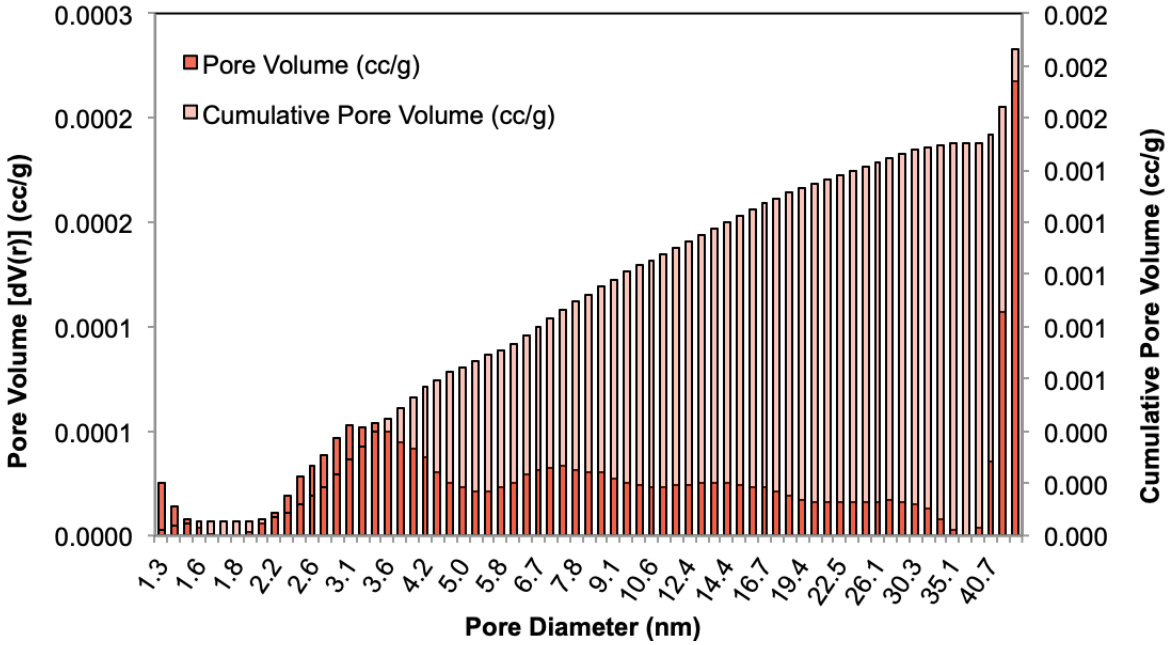

Figure 6.12: Pore volume versus pore diameter for sample 2-19.

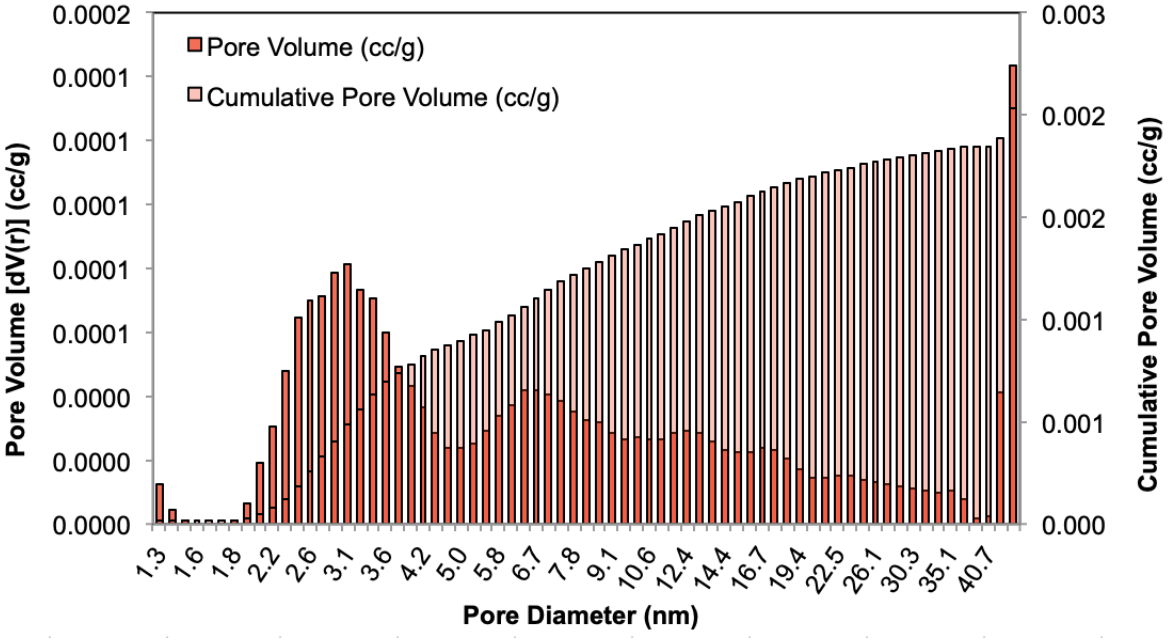

Figure 6.13: Pore volume versus pore diameter for sample 3-42.

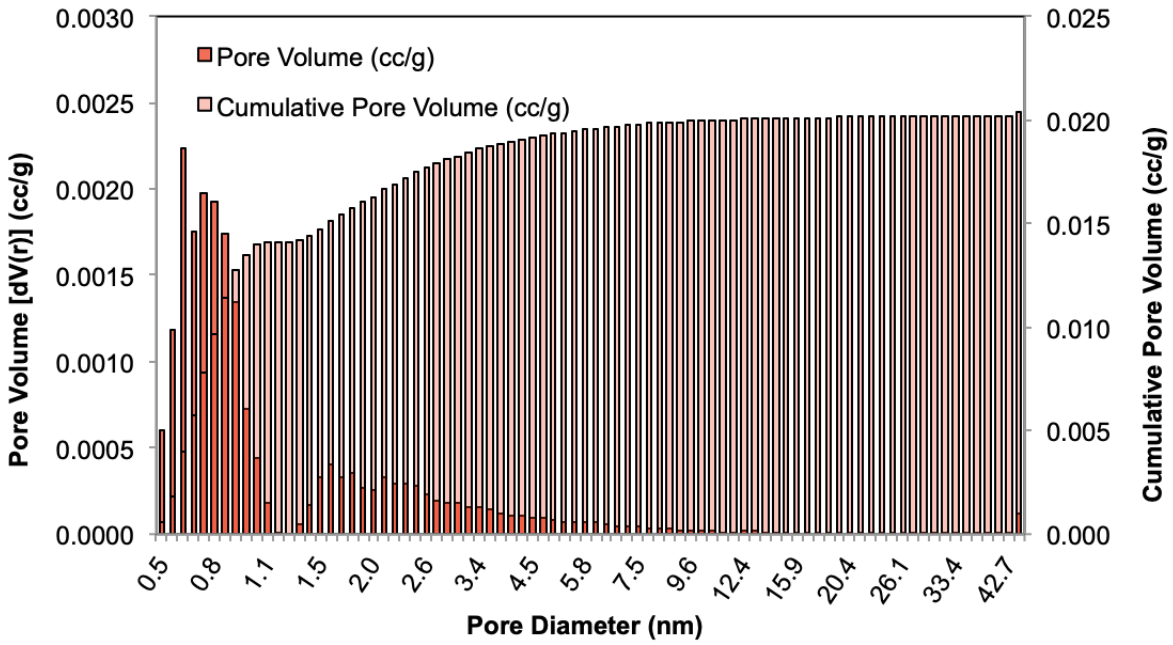

Figure 6.14: Pore volume versus pore diameter for sample 3-55A.

6.1.2 Mercury injection

Mercury injection capillary pressure (MICP) experiment was performed to measure the drainage only mercury injection capillary pressure and analyze the pore size distribution of the Diyab samples. However, since the pore sizes we are dealing with are in the nano-pore range, mercury injection will not yield meaningful results regarding pore size distribution due to the large size of mercury atomic structure. Nitrogen adsorption is a more useful tool in measuring pore size distribution in nanopores. However, MICP can shed light on the capillary pressure.

The lab measurement was performed by using Micromeritics AutoPore IV 9250 mercury porosimeter. Core samples were placed in the penetrometer and put under vacuum. Mercury is then injected at multiple pressures up to 60,000 psi with the volume of mercury injected at each stage is recorded. Apparent mercury injected volume is adjusted for each core sample for conformance. Conformance is the volume of mercury pressed into surface roughness and around the edges of the core after the penetrometer is filled with mercury (since mercury acts

as non-wetting fluid). Using the Swanson method, permeability of the cores is calculated. These measurements also shed light on the core's pore size distribution. As discussed in Chapter 5, pores can be divided into the categories shown in Figure 6.15 (Loucks et al. 2012).

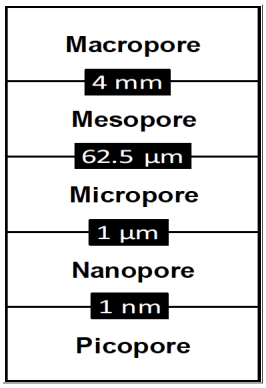

Figure 6.15: Pore size classification (Loucks et al. 2012).

Pore throat size (up to the micropore range) can be determined using the capillary law equation by assuming cylindrical pores using Equation 6.6.

$$r = \frac{2\gamma\cos\theta_c}{p_c} \tag{6.6}$$

where r is the radius of the pore throat, p_c is the capillary pressure measured, γ is the interfacial tension of mercury and θ_c is the contact angle of mercury in air. The contact angle θ_c varies depending on rock composition but an average of 140° is used as an industry standard. The mercury capillary data is then converted to reservoir conditions using Equation 6.7.

$$p_{c(g/w)} = \frac{(\gamma\cos\theta)_{c(g/w)}}{(\gamma\cos\theta_c)_{(m/a)}} p_{c(m/a)} \tag{6.7}$$

where $p_{c(g/w)}$ is the capillary pressure in gas-brine, $p_{c(m/a)}$ is the capillary pressure in mercury-air, $\gamma\cos\theta_{c(g/w)}$ is the surface tension of brine multiplied by cosine of the contact angle of brine in air and $\gamma\cos\theta_{c(m/a)}$ is the surface tension of mercury multiplied by cosine of the contact angle between mercury and air. For the air/water data, contact angle is 0° and

surface tension is 72 dyne/cm. Equation 6.8 is then used to calculate the height above free water:

$$H = \frac{p_{c(m/a)}(\gamma \cos\theta_c)_R}{(\gamma \cos\theta_c)_{(m/a)}(\rho_w - \rho_h)} \tag{6.8}$$

where $(\gamma \cos\theta_c)_R$ is the interfacial tension multiplied by cosine of the contact angle of the reservoir fluid and ρ_h is the reservoir density gradient of the hydrocarbon. ρ_w is water density with a gradient of 0.434 psi/ft. The hydraulic gradient for oil is 0.346 psi/ft and 0.100 psi/ft for gas. Figure 6.16 shows the relationship between mercury intrusion pressure and saturation for sample 3-55. All the cores follow a similar curve with a maximum intrusion pressure of 60,000 psi, which is equivalent to a minimum pore size of 3.6 nm. This is the technical maximum pressure due to the large atomic size of mercury as mentioned in the literature review section.

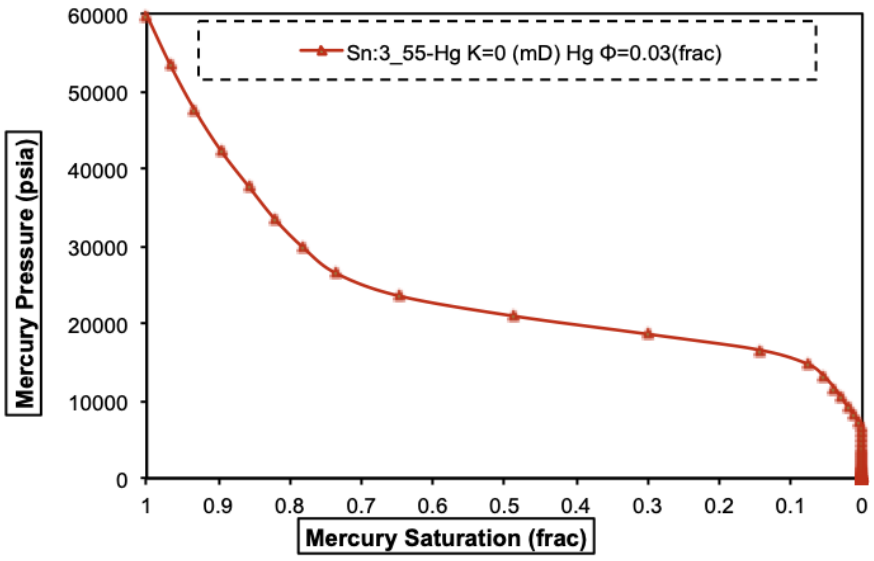

Figure 6.16: Mercury intrusion pressure.

6.2 Methane Adsorption Potential and TOC

The amount of gas in place in any shale play is heavily influenced by TOC and the adsorption potential of the rock's surface. Methane in shale is adsorbed by kerogen and various clay minerals. Adsorption in shale is purely a physical process which means that it is reversible. Methane molecules can completely adsorb/desorb onto the surface area of the pores. Since a large part of the gas in place is adsorbed, it is important to understand and study methane adsorption of the shale. Clarkson and Haghshenas (2013) classified five mechanisms for the existence of methane in shales: 1) adsorption onto the surface, 2) conventional compressed gas storage in natural and hydraulic fractures, 3) conventional storage in rock's matrix porosity, 4) solution in formation water, 5) adsorption solution in organic matter.

It is important to note that adsorbed gas has a higher density than that of the surrounding gas. The organic matter occupies part of the bulk rock and consists of micropores. The specific surface area, per gram of solid, is an important parameter in governing the adsorption of gas. The rougher surfaces and smaller pore sizes account for a larger specific surface area which leads to more adsorption.

Yu et al. (2016) studied and compared the BET and Langmuir methane adsorption isotherm in Marcellus. They found that their samples followed the BET adsorption curve. Figure 6.17 compares the adsorption of both Langmuir and BET isotherms. We notice that gas desorption in the BET isotherm is more significant at lower pressures than that of Langmuir's isotherm. This is due to the slope of the BET isotherm which is higher than that of Langmuir's isotherm at higher pressure causing more adsorbed gas is released earlier. We also notice that the amount of adsorbed gas released with BET isotherm is higher than that of Langmuir's isotherm using the same pressure differential between the reservoir pressure and the bottom hole pressure.

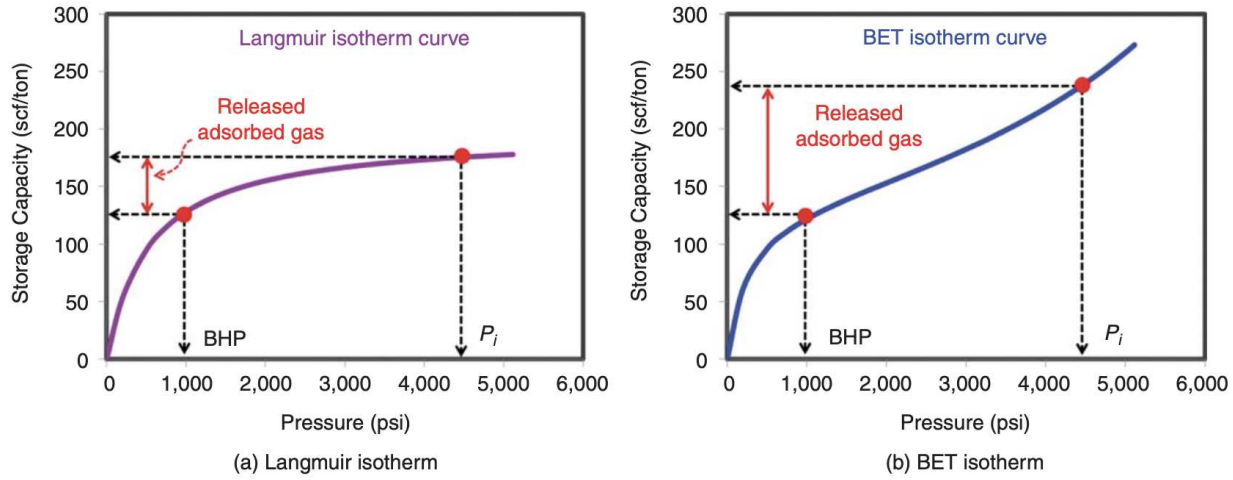

Figure 6.17: Comparison between Langmuir and BET adsorption isotherms (Yu et al. 2016).

The same samples used in nitrogen adsorption were used for methane adsorption testing. It was found that the cores obeyed the Langmuir adsorption isotherm curves as shown in Figure 6.18 to Figure 6.21.

Using the Langmuir equation, the Langmuir coefficient can be calculated as

$$V_a = \frac{V_L p}{p_L + p} \tag{6.9}$$

If we take sample 3-55 for instance, $V_a = 113.4\frac{p}{p + 948.8}$ where p_L in this case is 948.8 psi (pressure at which half of total gas is adsorbed) and V_L (maximum adsorption capacity) is 113.4 scf/ton. The table below summarizes the results of the methane adsorption tests along with TOC data. When assessing the richness of source rocks, TOC values of 1 - 2% are considered to be good, 2 - 5% are considered to be very good and anything above is considered excellent.

Table 6.3: Methane adsorption isotherm summary

Sample	Depth ft	TOC %	Langmuir Volume scf/ton	Langmuir Pressure psia
1_11	12442.65	1.17	15.4	991.7
2-19	12512.40	0.58	13.0	744.8
3-42	12852.10	2.43	51.2	2366.0
3-55	12868.15	5.72	113.4	948.8

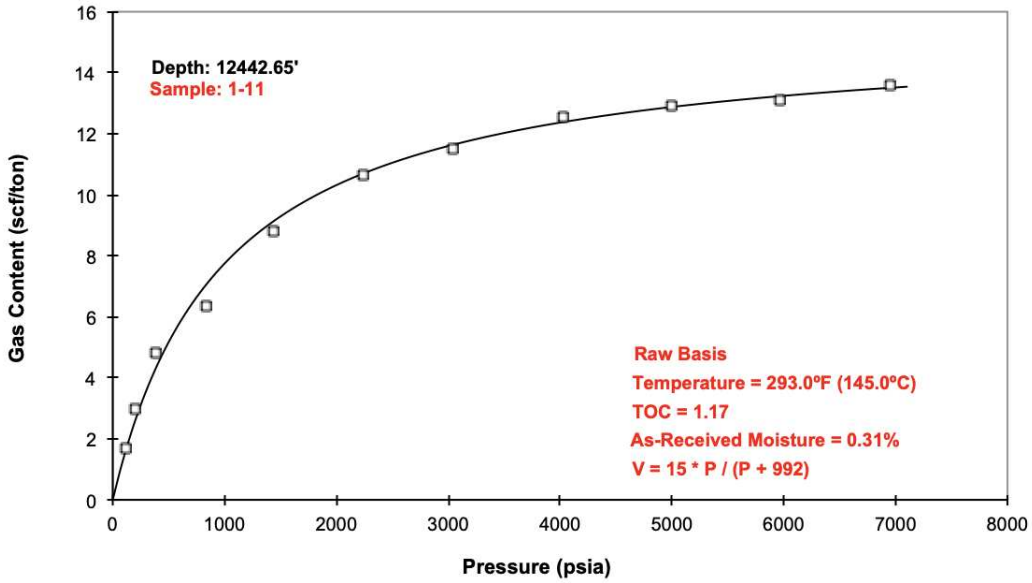

(a) Methane adsorption isotherm

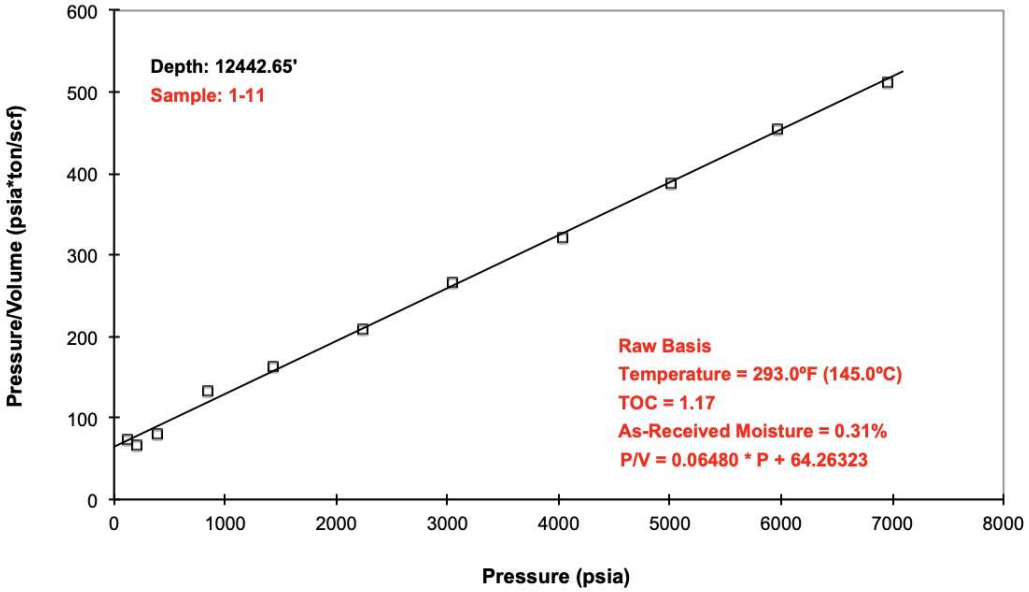

(b) Adsorption Langmuir plot

Figure 6.18: Sample 1-11 methane adsorption isotherm.

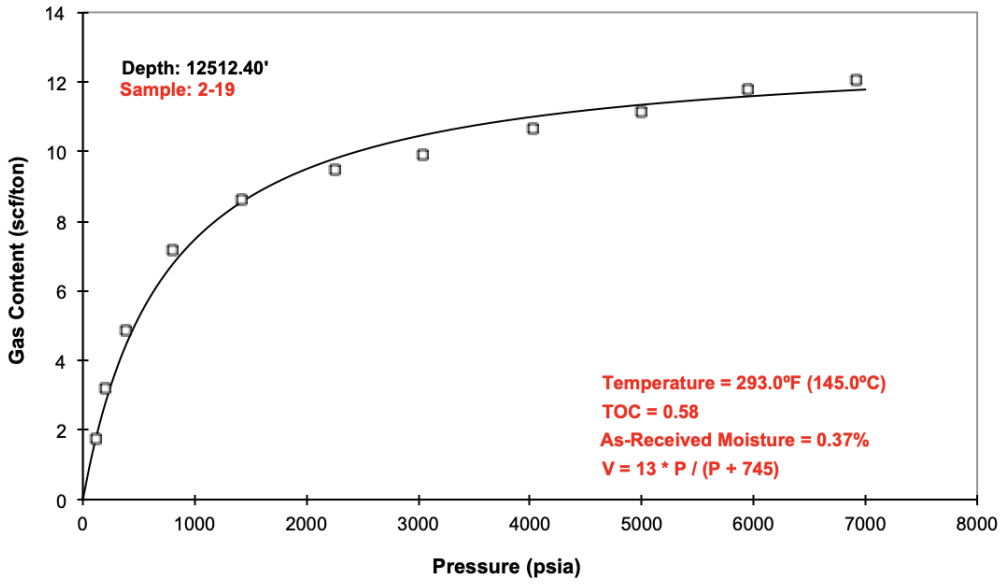

(a) Methane adsorption isotherm

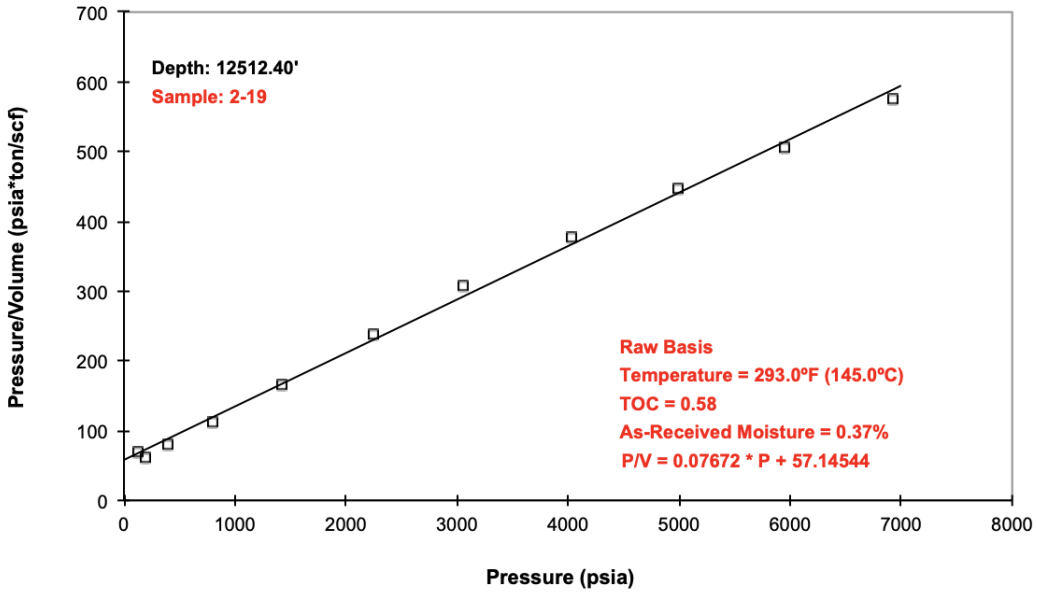

(b) Adsorption Langmuir plot

Figure 6.19: Sample 2-19 methane adsorption isotherm.

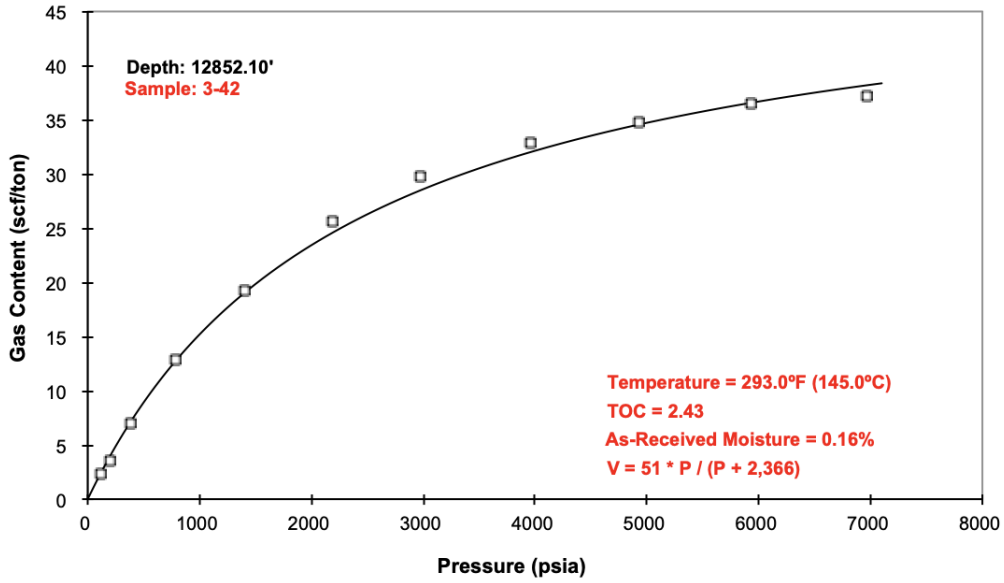

(a) Methane adsorption isotherm

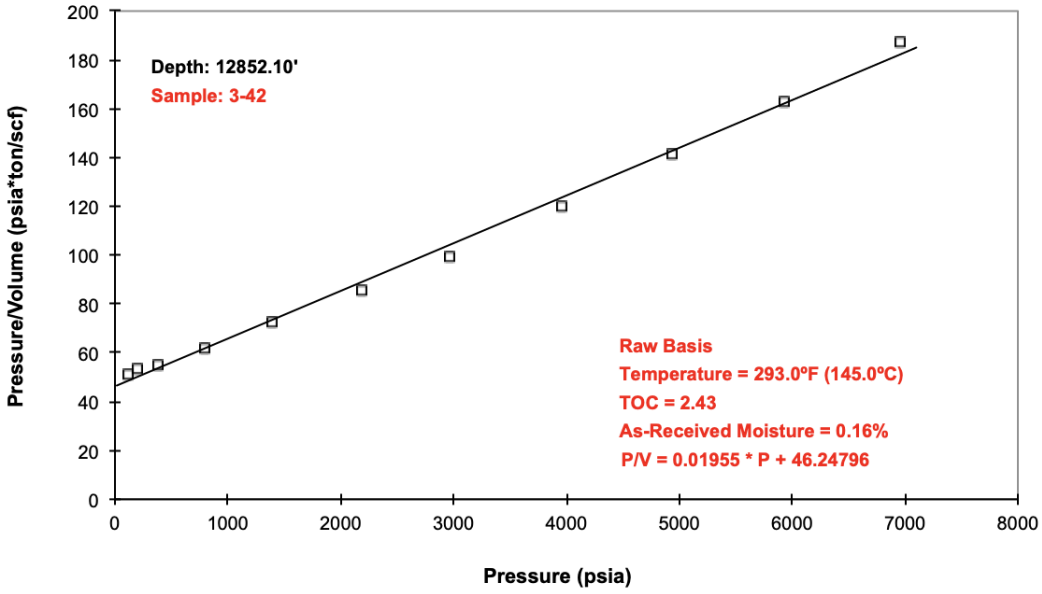

(b) Adsorption Langmuir plot

Figure 6.20: Sample 3-42 methane adsorption isotherm.

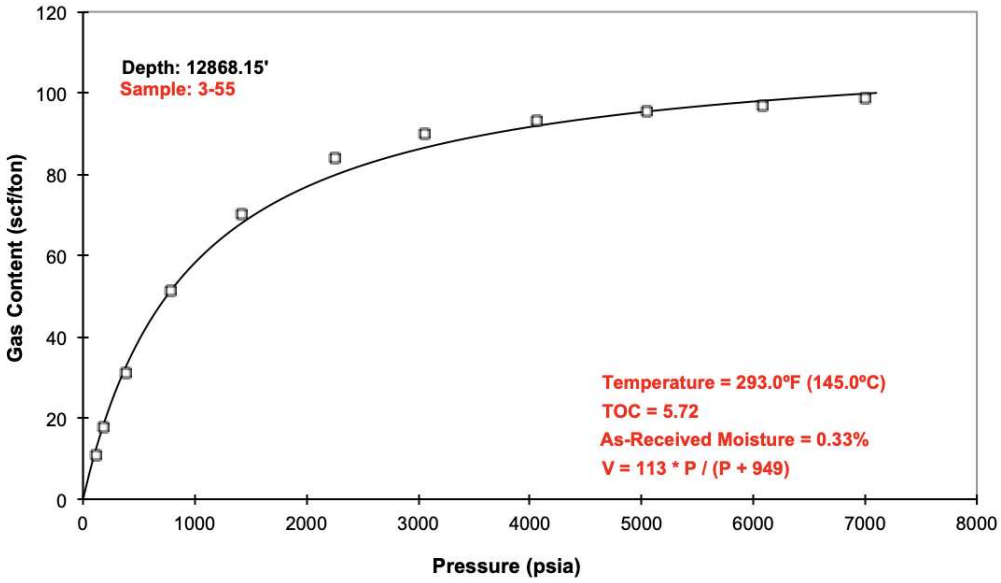

(a) Methane adsorption isotherm

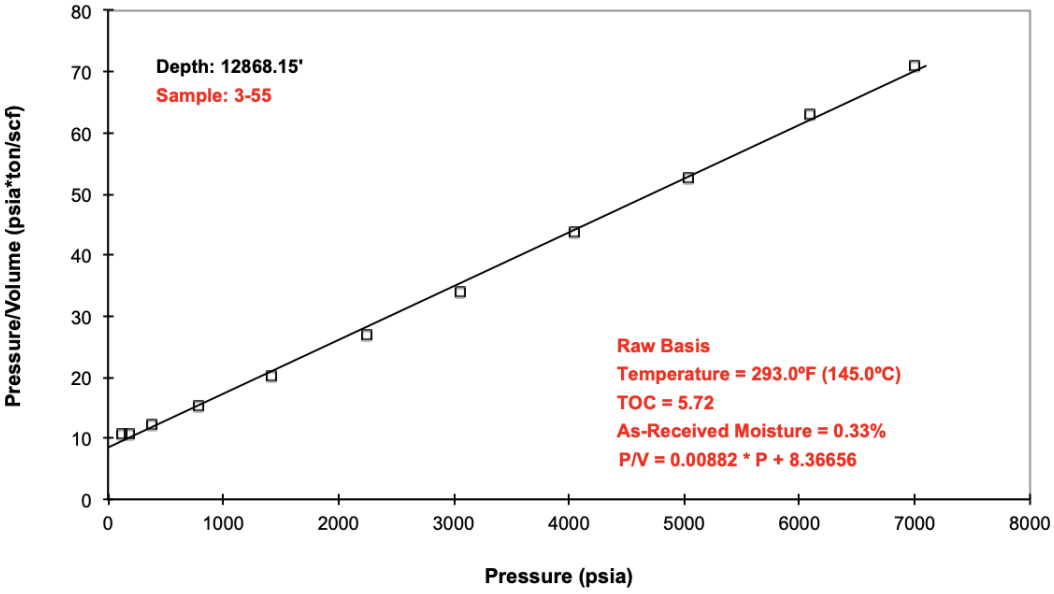

(b) Adsorption Langmuir plot

Figure 6.21: Sample 3-55 methane adsorption isotherm.

The Langmuir volume is then plotted against TOC to obtain a straight line with an equation as shown in Figure 6.22. The equation obtained from the straight line describes the relationship between adsorbed gas volume and TOC which is important when estimating GIP.

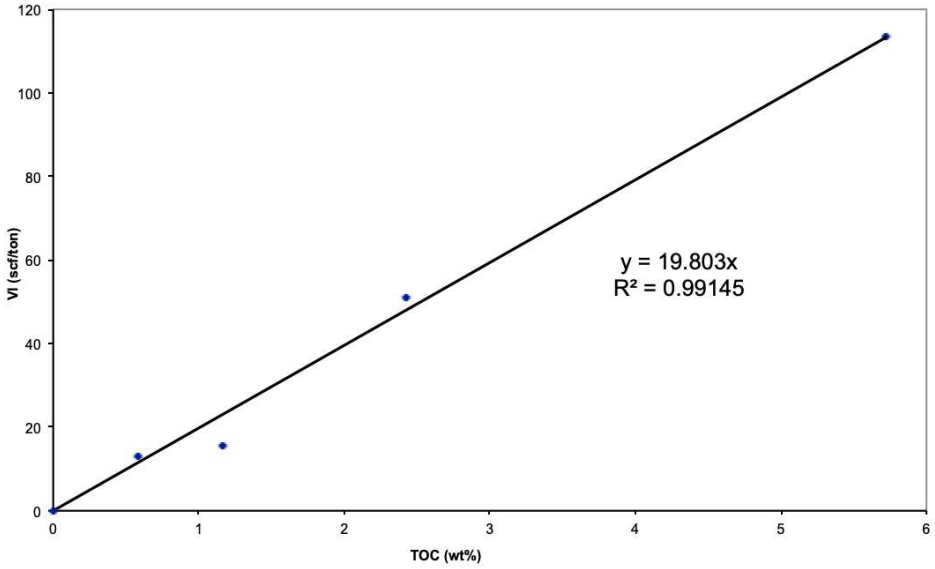

Figure 6.22: Volume adsorbed versus TOC.

6.3 Diyab Geomechanical Experiment

Four cores were tested for geomechanical parameters to determine their mechanical, elastic and strength behavior. Results for these tests are summarized in Table 6.4. The experimental data can then be inputed into the geomechanical model for in-situ stress calculations, wellbore stability assessments and hydraulic fracturing operations. The data can also be compared to the log-derived estimated mechanical properties.

Table 6.4: Diyab geomechanical tests summary

Depth	Plug	E_{dyn}	ν_{dyn}	E_{st}	ν_{st}	S_0	φ_f	UCS_{MC}	E_{UCS}	ν_{UCS}	UCS
ft	Type	Mpsi		Mpsi		psi		psi	Mpsi		psi
12275	H	10.8	0.30	8.2	0.33	6608	38	27204	8.58	0.32	27969
12276	V	10.4	0.31						6.25	0.25	25663
12350	H	10.6	0.30	7.68	0.31	5631	38	22940	6.53	0.31	24263
12351	V	9.48	0.29						5.95	0.32	14880
12736	H	9.21	0.29	6.26	0.29	5818	36	22705	6.32	-	13606
12737	V	9.05	0.27						5.03	0.28	22639
12802	H	11.1	0.30	8.99	0.33	5189	40	22490	8.39	0.31	17620
12803	V	11.3	0.32						8.65	0.38	18548

When conducting geomechanical stress tests such as axial testing on cores, we obtain static moduli. Dynamic moduli are obtained indirectly by interpreting sonic wave velocities and logs. Since sonic wave velocity and density logs are the most commonly available logs, it is very common to obtain dynamic modulus values this way. There are also many empirical correlations that calculate rock strength, Biot's coefficient and internal friction coefficient in both vertical and horizontal directions. It is important to note that these correlations are specific to lithology and geography.

Static and dynamic values could be noticeably different and therefore it is important to specify how these values were obtained. Static Young's Modulus is usually lower than dynamic Young's Modulus and the ratio of static to dynamic is stress-dependent. Static moduli are also referred to as drained whereas dynamic moduli are referred to as undrained since fluid saturation is the main reason to the discrepancy between the static and dynamic modulus values.

In order to obtain compressional and shear velocity values, the arrival time of the waveform passing through the core has to be first analyzed. This information is used in conjunction with strain-gauge data that measures the change in length in the core to obtain acoustic velocity. Figure 6.23 illustrates a compressional waveform from one of the experiments and the straight line represents the arrival time.

These waveforms are recorded and analyzed at varying effective stress levels. The effect of increased effective stress on P-wave arrival time is shown in Figure 6.24. As the effective stress is increased, the core sample is compressed which results in faster arrival time. This is confirmed with strain gauge data that quantifies the amount that the core has been compressed. Multiple waveforms are recorded and compared at the same conditions since the waveform can be difficult to interpret. The same analysis is applied to S-wave arrival.

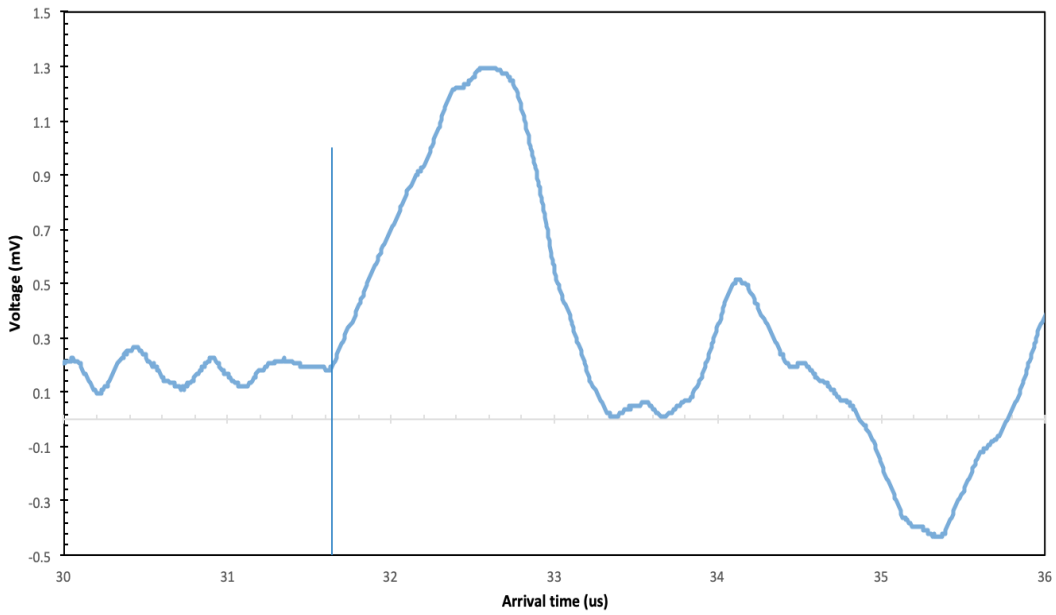

Figure 6.23: Sample arrival time wave analysis.

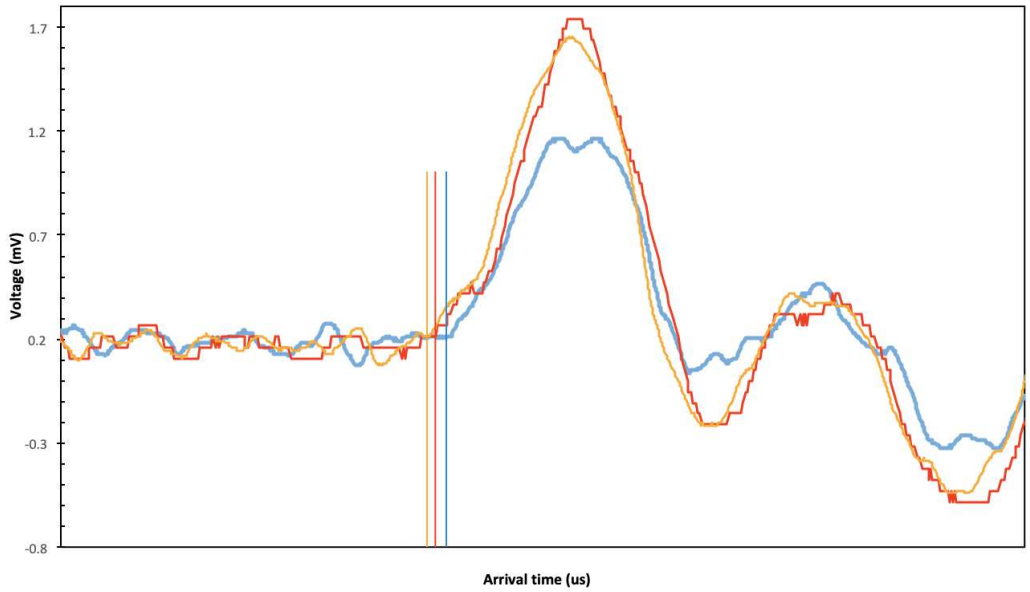

Figure 6.24: Effect of increased effective stress on compressional arrival time.

Ultrasonic measurements were conducted under hydrostatic stress to measure the dynamic elastic properties whereas single stage tri-axial compression tests were used to estimate the static properties. The compressional and shear velocity results obtained from the various cores are shown in Figure 6.25 and Figure 6.26.

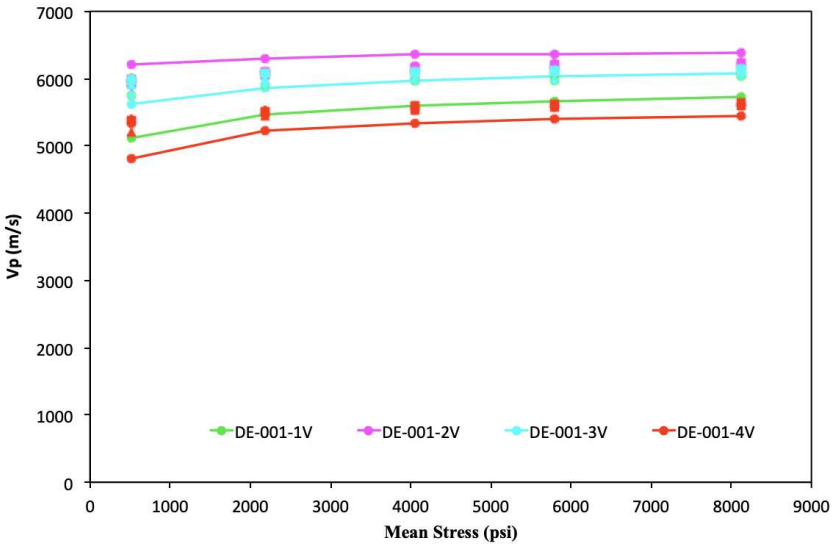

Figure 6.25: Compressional velocity versus stress.

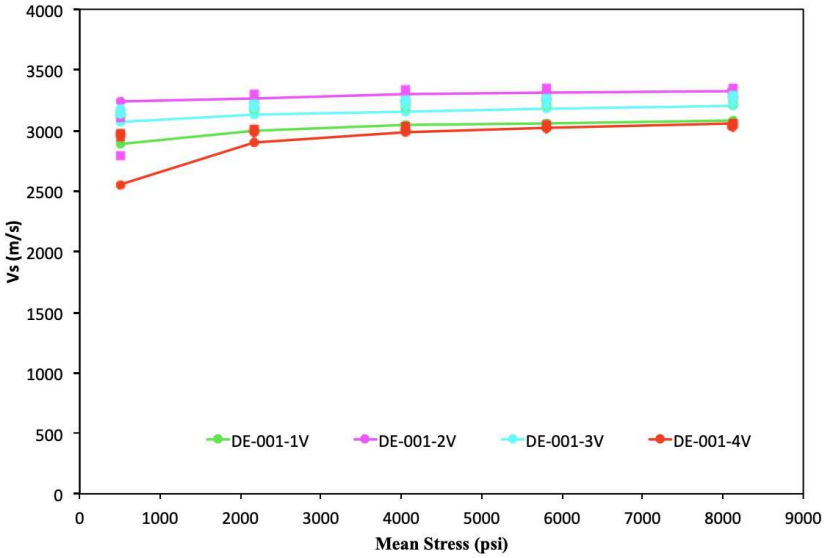

Figure 6.26: Shear velocity versus stress.

Two shear waves velocities were measured for vertical and horizontal plugs and were similar suggesting that the plugs are isotropic. The dynamic Young's Modulus and Poisson's Ratio are calculated from these velocities using Equations 6.10 and 6.11.

$$E_{dyn} = \frac{\rho_b V_s^2 (3V_p^2 - 4V_s^2)}{V_p^2 - V_s^2} \tag{6.10}$$

$$\nu_{dyn} = \frac{V_p^2 - 2V_s^2}{2(V_p^2 - V_s^2)} \tag{6.11}$$

The relationship between dynamic Young's Modulus and Poisson's Ratio with effective stress of the tested samples is shown in Figure 6.27.

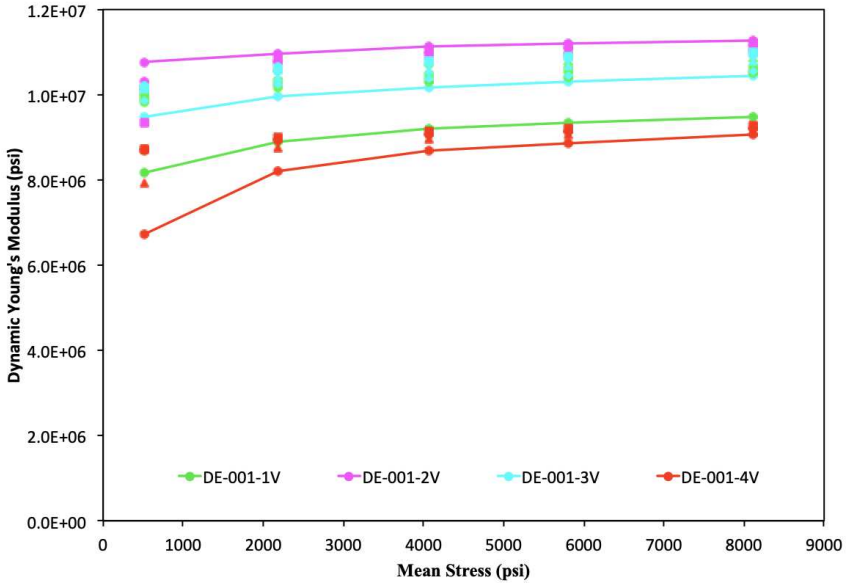

Figure 6.27: Dynamic Young's Modulus versus stress.

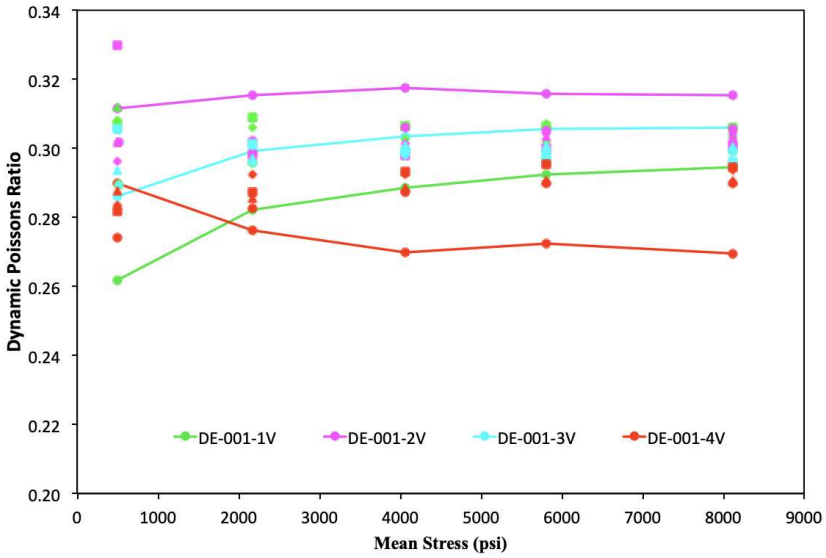

Figure 6.28: Dynamic Poisson's Ratio versus stress.

Although we observe that Young's Modulus increases as confining pressure increases, this effect becomes almost negligible at high stress. Poisson's Ratio is unaffected by confining pressure. Static elastic properties were then measured from mechanical tests. These values are more reliable when studying high deformation in analysis involving hydraulic fracturing and wellbore stability assessment. It was observed that horizontal plugs have a larger Young's Modulus than vertical plugs at the same depth. The variation of static Young's Modulus follows a similar pattern to dynamic values with depth. A correlation between the static and dynamic values is shown in Figure 6.29. Just as expected, the dynamic Young's Modulus is higher than the static. This is due to the nature of how the dynamic data is obtained from ultrasonic waves. Ultrasonic waves oscillate quickly through the medium and the fluid within the pore space does not have enough time to relax at high frequencies. This results in the fluid acting "stiffer" which explain the higher dynamic Young's Modulus. Alternatively, no relationship could be obtained for Poisson's Ratio as seen in Figure 6.30.

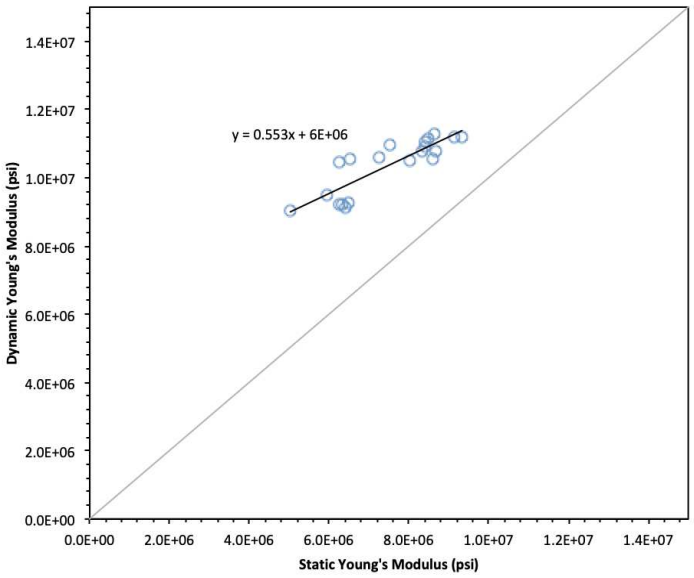

Figure 6.29: Static versus dynamic Young's Modulus.

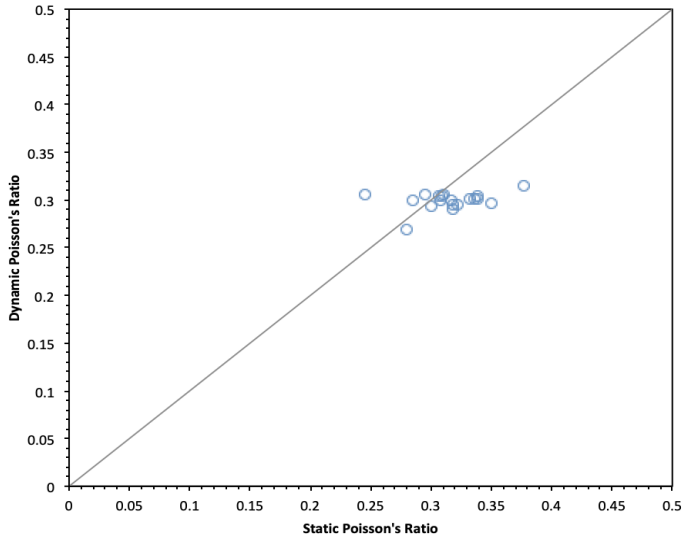

Figure 6.30: Static versus dynamic Poisson's Ratio.

The stress-strain relationship of a sample from the Diyab formation at different confining pressures is shown in Figure 6.31. The experiments were conducted until the sample failed.

The Mohr-Coulomb failure envelope was constructed from the peak axial stress and the confining pressure of each stage in the multistage triaxial compression tests for 3 samples as shown in Figure 6.32 to Figure 6.34. The Mohr-Coulomb failure envelopes match well the stress-state points obtained from the single-stage triaxial compressive tests. Table 6.5 summarizes the findings from these tri-axial experiments.

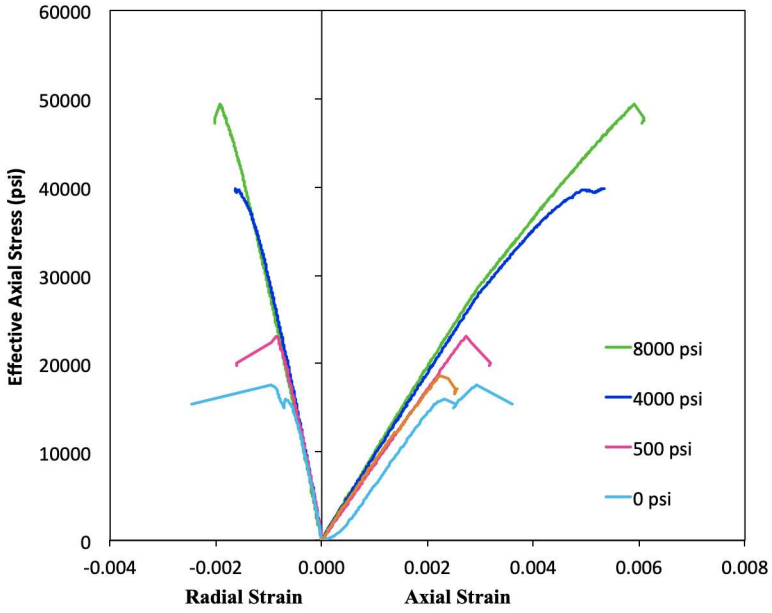

Figure 6.31: Stress-strain curve from tri-axial compression testing at different confining stresses.

Table 6.5: Parameters for Mohr-Coulomb failure criterion

Sample	Depth ft	S_o psi	φ_f deg.	UCS_{M-C} psi
D1	12776	6608	38	27204
D2	12802	5189	40	22490
D3	12350	5631	38	22940

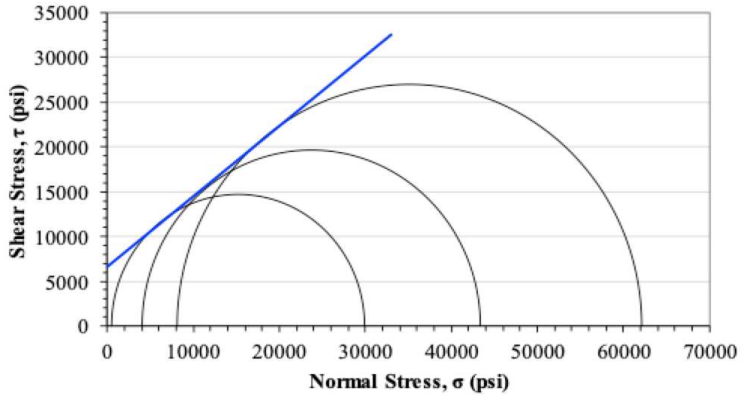

Figure 6.32: Mohr-Coulomb failure envelope of sample D1.

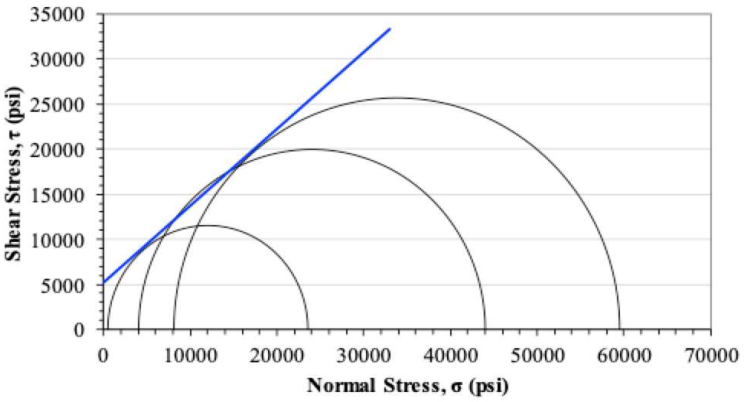

Figure 6.33: Mohr-Coulomb failure envelope of sample D2.

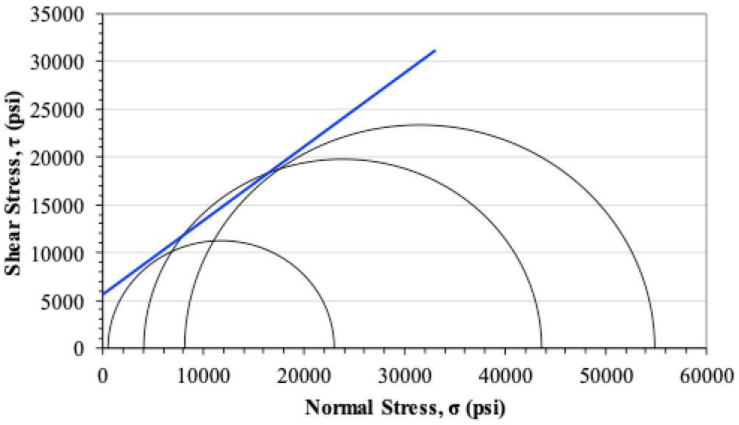

Figure 6.34: Mohr-Coulomb failure envelope of sample D3.

6.4 Model Validation

The grain contact model was used to match experimental acoustic velocity data. The input parameters are obtained from experiments and summarized in Table 6.6. Figure 6.35 and Figure 6.36 demonstrates that the grain contact model was able to generate fairly similar results with a good match to the experimental data for both compressional and shear velocity data. In order to estimate compressional and shear wave values, the model predicts gap stiffness which it calculates from separation distance of the grains. This separation distance between grains is calculated when the sum of total surface forces is equal to total external force.

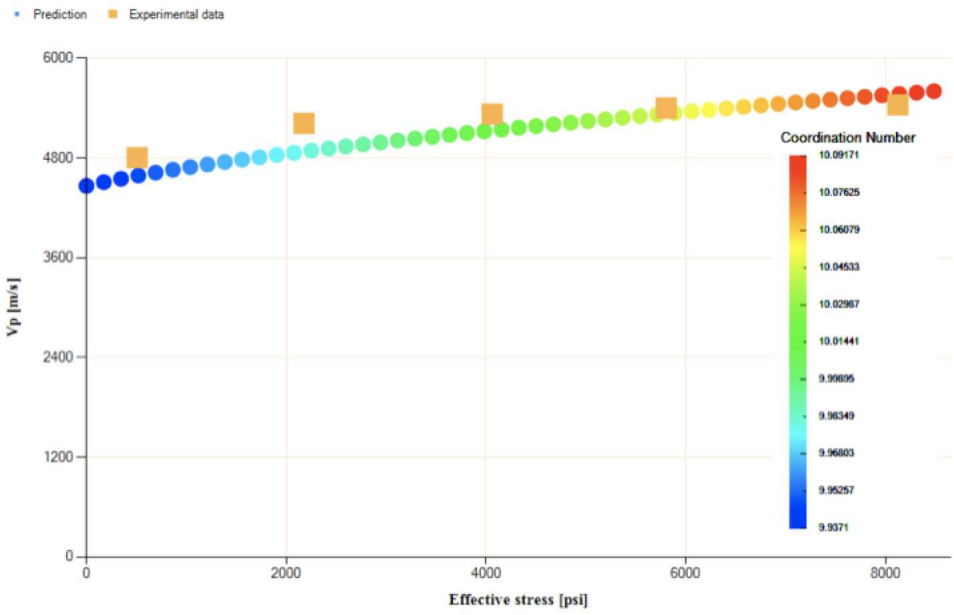

Figure 6.35: Matching experimental compressional velocity data to grain contact model simulated results.

Table 6.6: Input parameters for theoretical model

Parameter	Value	Unit
Sphere Radius	3	μm
P-wave Velocity	5451	m/s
S-wave Velocity	2987	m/s
Poisson's Ratio	0.29	
Porosity	3.3	%
CO_2 Refraction Index	1.00045	
Dispersive Coefficient	0.001	
Rock Density	2.65	g/cm^3
Rock Dielectric Constant	6	
CO_2 Dielectric Constant	1.07	
Rock Refraction index	1.45	
Molarity	1	
Valence	1	
Zeta Potential	-30	mV
Collision Diameter	4.5E-10	cm
Gas Saturation	3.8	%
Structural Constant K_l	500	dyne/cm^2
Structural Constant l	1E-7	cm
Absorption Frequency	3E+15	s
Boltzman Coefficient	1.381E-23	m^{2}kg^{-2}K^{-1}
Ionic Concentration	6.02*10^{20}*M	ion/mol
Temperature	25	$^\circ$C
CO_2 Viscosity	0.0146	cp
CO_2 Density	1.784	kg/m^3
M. Depth	12736	ft
Young's Modulus	6.28E+6	psi
Shear Modulus	2.43E+6	psi

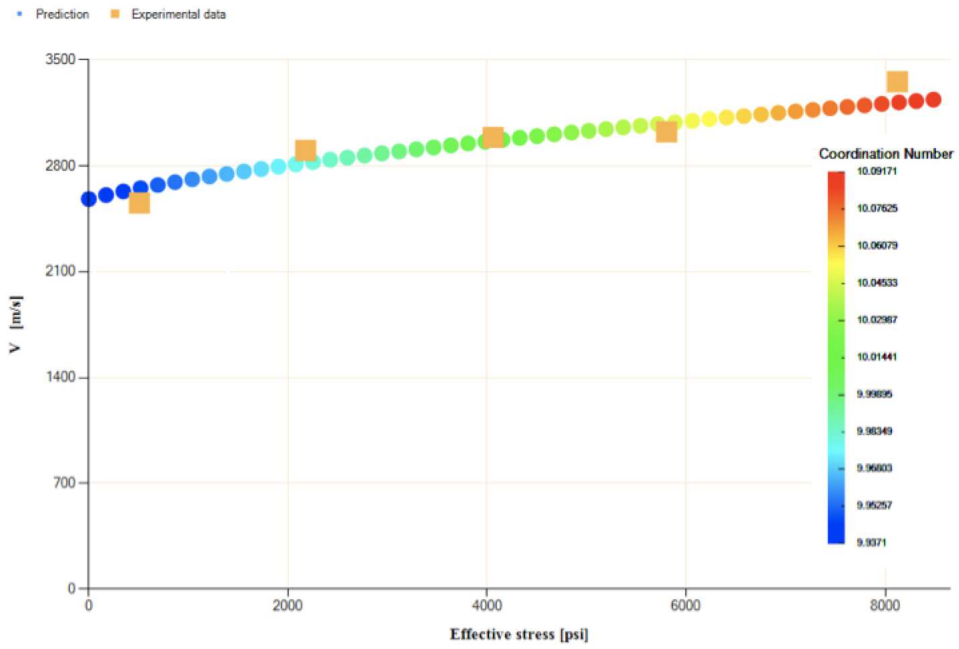

Figure 6.36: Matching experimental shear velocity data to grain contact model simulated results.

Figure 6.37 and Figure 6.38 show the effect of frequency dependence on acoustic velocity. This frequency dependence is explained by the rapidness at which the confined fluid between solid grains can escape from the contact area. At high frequency (fast oscillating loads), the confined fluid does not have enough time to escape which causes the rock-fluid system to act as if it is in an un-relaxed state, higher gap stiffness. Whereas at low frequency, the fluid has enough time to be pushed out resulting in a lower gap stiffness (softer rock). It is worth noting that the speed at which the confined fluid escapes the contact area is a function of the fluid's mobility. Since gas has a higher mobility, it can move out of the contact region more easily making a gas-saturated sample less frequency-dependent compared to a liquid saturated-sample.

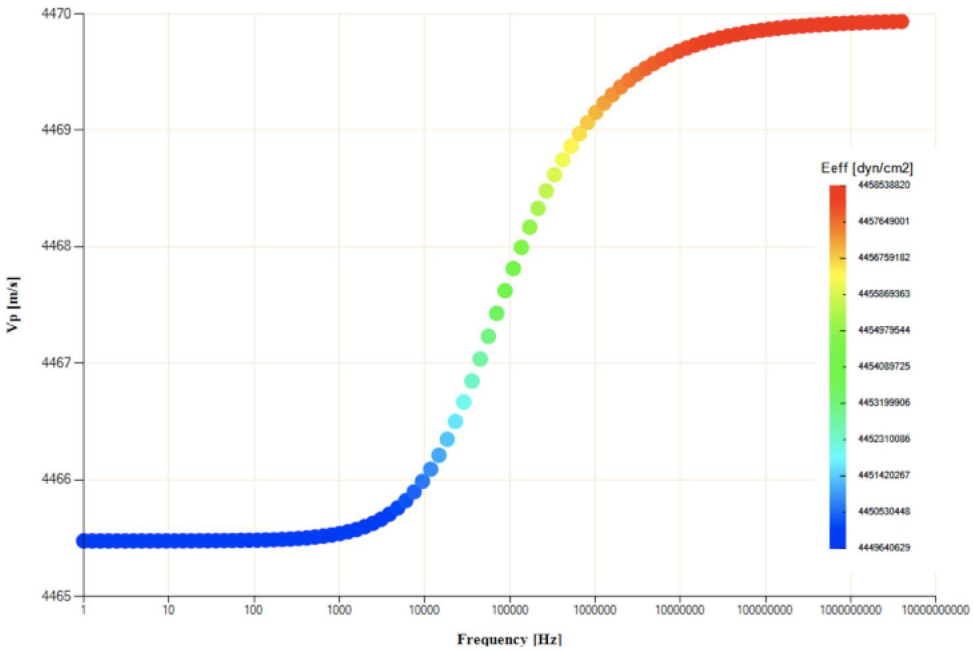

Figure 6.37: Effect of frequency on compressional wave velocity.

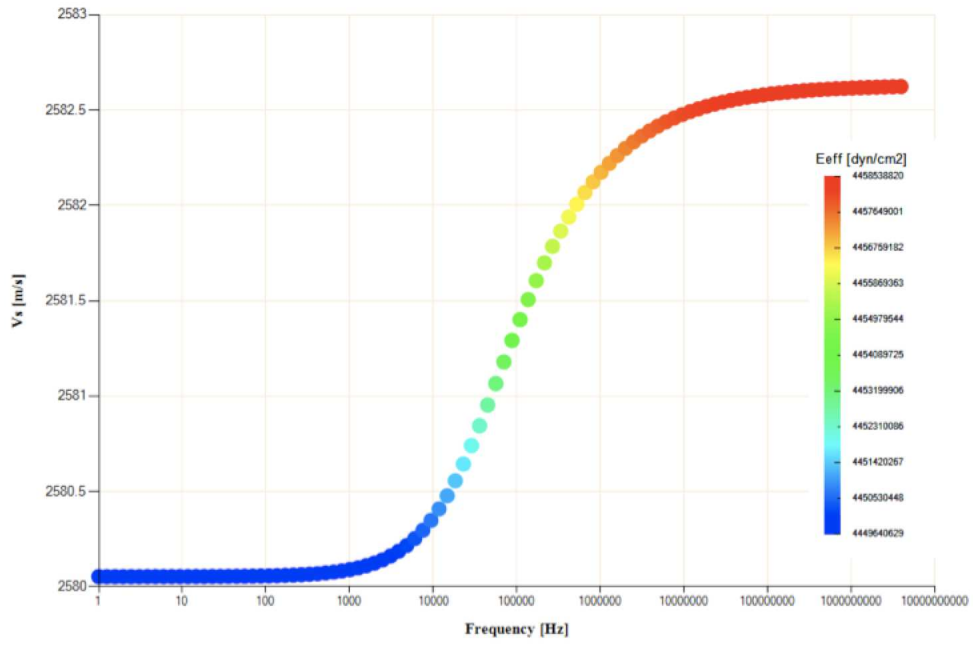

Figure 6.38: Effect of frequency on shear wave velocity.

The model allows the estimation of acoustic velocities in lieu of experimental data and demonstrates how the micro-mechanics at the grain contacts affect the moduli of the media. It can be used to predict acoustic velocities and deformation in fluid-saturated rocks. Based on sensitivity analysis, it was found that frequency, clay content, porosity, stress, saturation and anisotropy have the most significant effects on the simulated outcomes of the model. Fluid density, viscosity and its electrochemical interaction with solid surfaces also had a major influence in modeling the rock's ability to propagate acoustic waves.

Figure 6.39 shows a sensitivity map of the frequency dependence on effective stress and velocity. It can be observed that velocity/stress data is more frequency-dependent at higher frequencies. It is worth noting that the coordination number is calculated from the model proposed by Maske et al. (2004).

$$C_n = 6 + 9.1\,(0.37 - \phi)^{0.48} \tag{6.12}$$

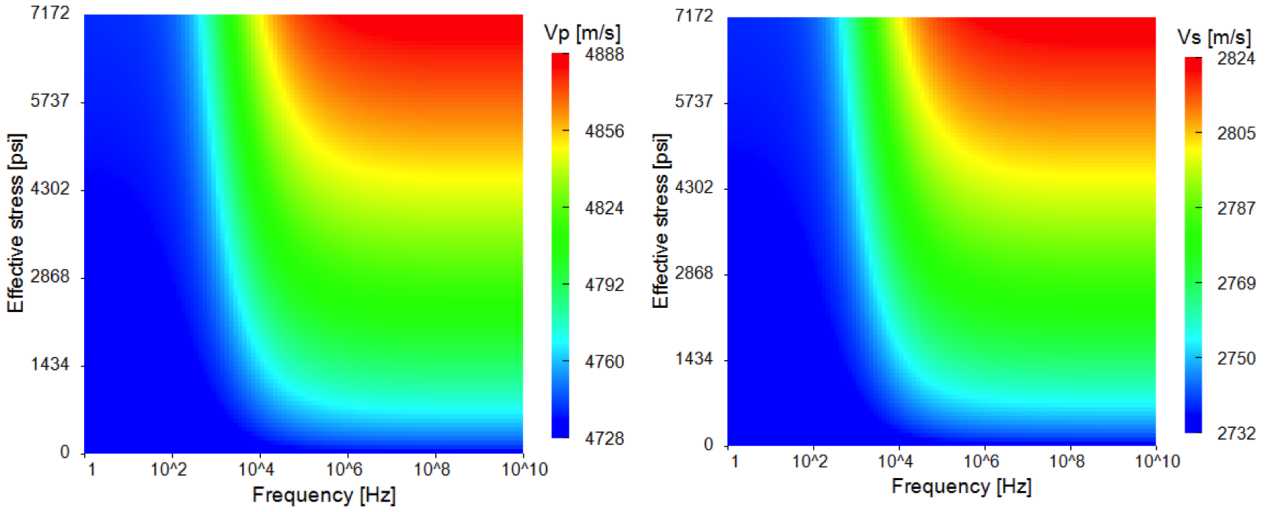

(a) Compressional velocity dependence

(b) Shear velocity dependence

Figure 6.39: The dependence of velocity on frequency and effective stress.

6.5 Effect of Capillary Condensation

6.5.1 Change in Acoustic Properties

Using the tri-axial cell set-up and the methodology described in the previous section to calculating ultrasonic velocity, the change in compressional velocity with pore pressure under the same effective stress for the sample is shown in the figure below.

We observe an initial decrease in compressional velocity as pore pressure increases before condensation occurs as shown in Figure 6.40. The initial decrease of compressional velocity is attributed to the expansion of the pore volume when pore pressure increases, which is similar to the observations made by (Wang et al., 2016) and (Gunther et al., 2008). After this initial decrease, we observe that compressional velocity slightly increases at a pressure around 750 - 800 psi which is close to the condensation pressure predicted by our theoretical model.

The change in shear wave velocity with pore pressure is shown in the figure below. Shear wave remains relatively unaffected up until the 750 - 800 psi pore pressure range where a change of trend is observed as shown in Figure 6.41. We theorize that as gas starts condensing in the nanopores, the confined fluid is trapped by such strong surface forces that the trapped fluid moves/ interacts as if they were part of the grains. This resistance to shear causes the shear velocity to increase. This also confirms the theoretical model estimate that capillary condensation occurs. The increase of shear wave velocity is because of the phase change from gas to liquid as condensation occurs. The condensed liquid has lower mobility and higher resistance to shear resulting in the increase of shear velocity.

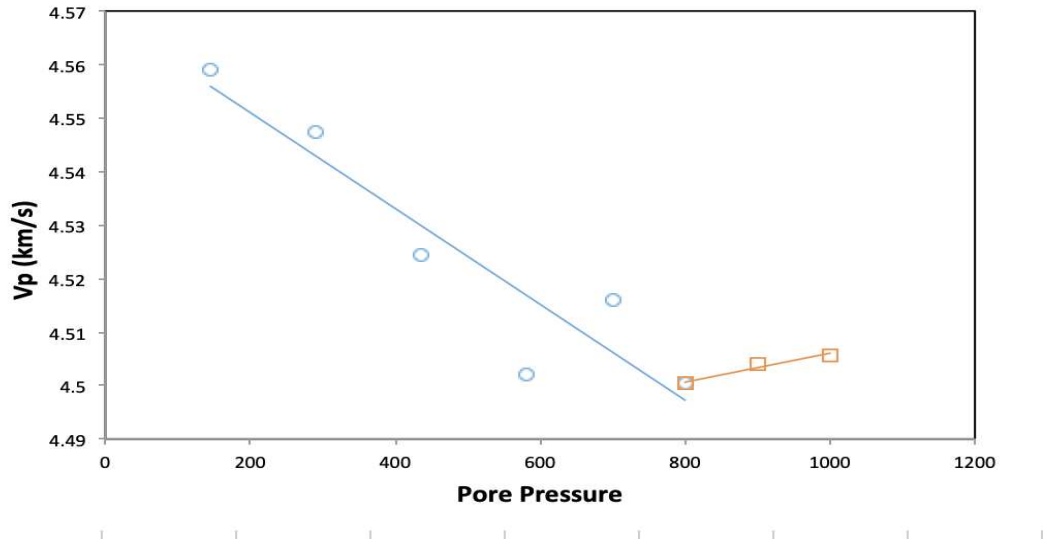

Figure 6.40: TQ-01 compressional wave velocity vs pore pressure.

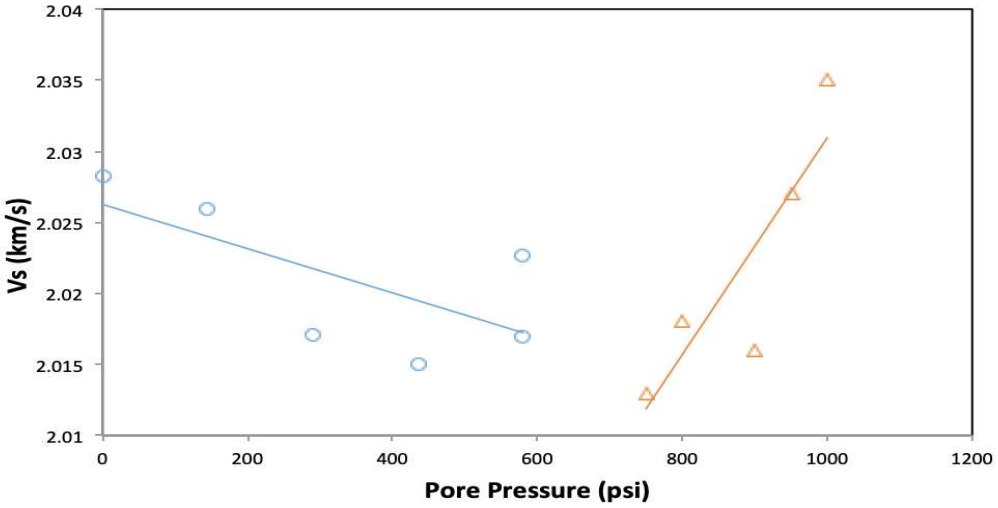

Figure 6.41: TQ-01 shear wave velocity vs pore pressure.

We also studied the effect of increased effective stress on wave velocity. As expected, wave velocity increases with effective stress. This increase is more noticeable at higher pore pressures as seen in Figure 6.42 and Figure 6.43. This indicates that as a larger portion of the pore space is filled with condensed liquid, the grain contact is reinforced, hence the rock is stronger.

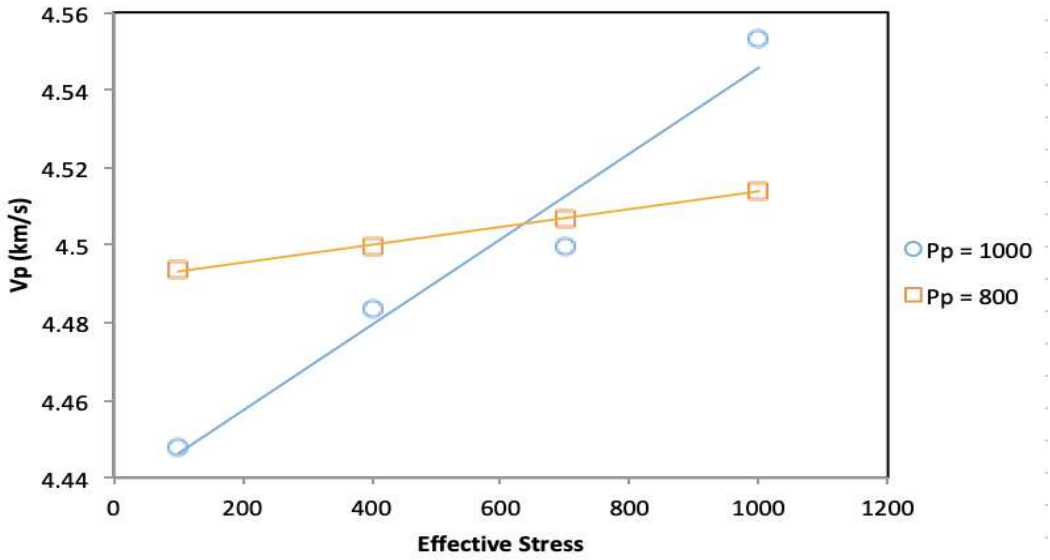

Figure 6.42: Effect of effective stress on compressional wave velocity.

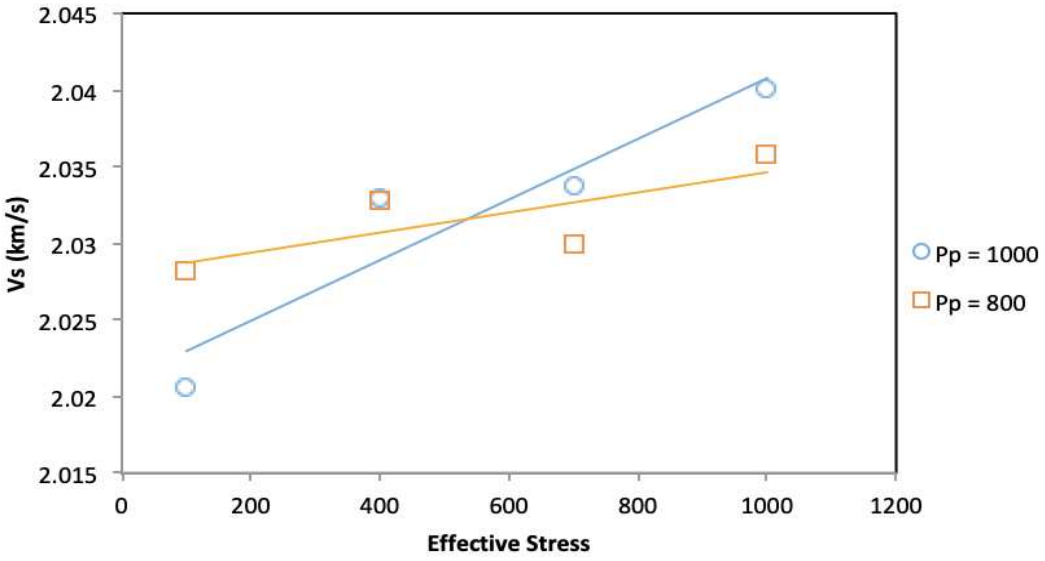

Figure 6.43: Effect of effective stress on shear wave velocity.

6.5.2 Change in Mechanical Behavior

Elastic modulus testing of AC-01 sample was conducted at increasing pore pressures. At each stage, axial stress was increased by 900 psi (loading) then decreased back to original level (unloading). The stress-strain relationship of the sample at increasing pore pressure

levels is shown in Figure 6.44. We notice that as pore pressure is increased, a more visible hysteresis loop is observed between the loading and unloading cycles. This represents the loss of energy to the fluid as more liquid condenses with increased pore pressure with the smallest nanopores condensing first at lower pressure.

Using the stress-strain data, the Young's Modulus of the sample was calculated as well. The change in Young's Modulus with pore pressure at varying effective stress levels is shown in Figure 6.45. We can observe that a change in trend occurs at around 750 - 800 psi where the modulus starts increasing which is an indication that capillary condensation occurs in the pore space of the sample. We observed that the Young's Modulus increase about 5% after condensation occurs. This increase in attributed to the increase in pore stiffness as condensation occurs reinforcing the grain contact. This is a clear indication of the effect of condensation on the mechanical properties of the sample.

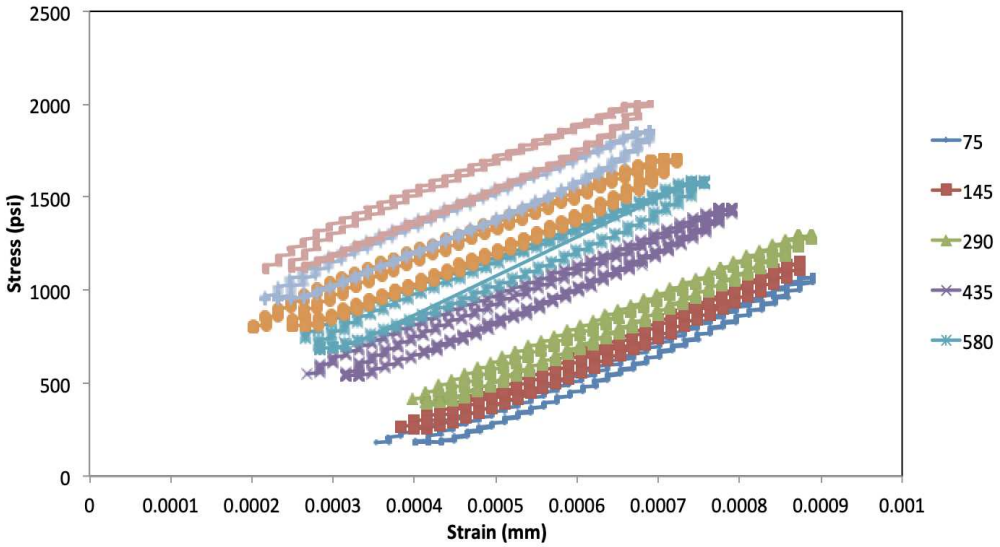

Figure 6.44: Stress-strain relationship at varying pore pressures.

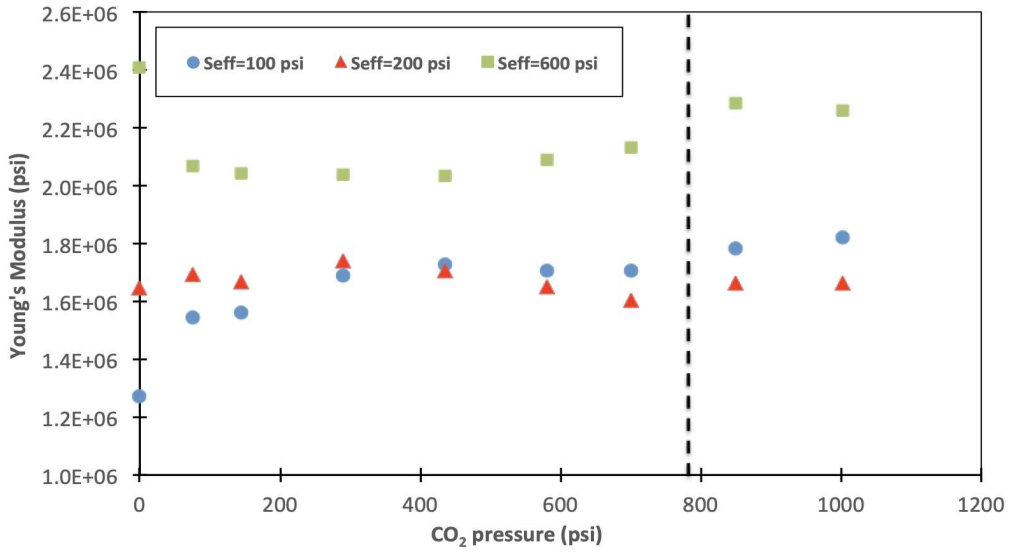

Figure 6.45: Change in Young's Modulus with increasing pore pressure at varying effective stress levels.

Using the data from Table 6.7, our model demonstrated that the change in velocity after accounting for capillary condensation is about 5% higher than when condensation is not accounted for. This effect is more pronounced at higher frequencies. This is shown in Figure 6.46 and Figure 6.47.

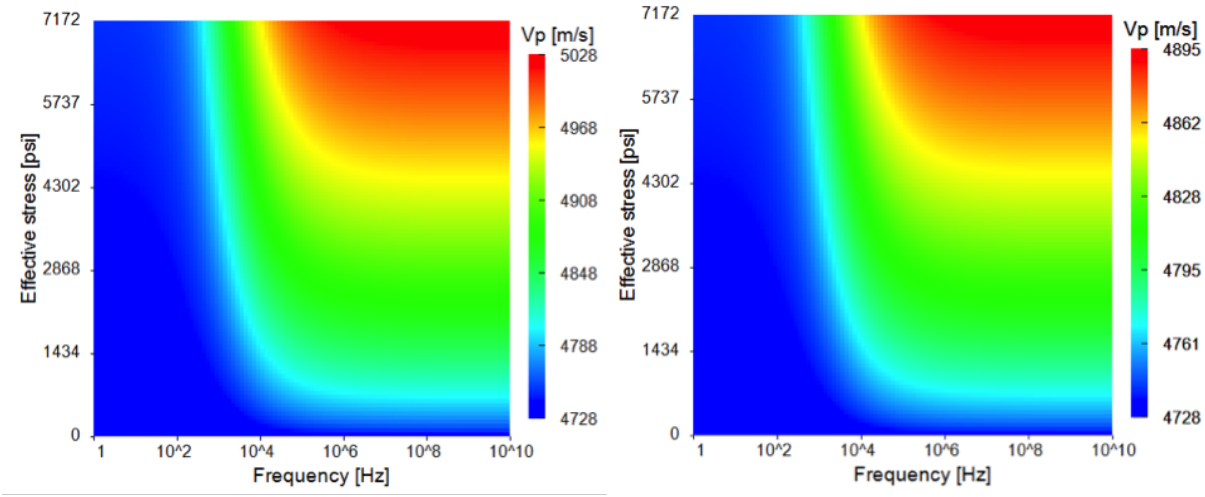

(a) With condensation (b) Without condensation

Figure 6.46: Effect of capillary condensation on compressional velocity.

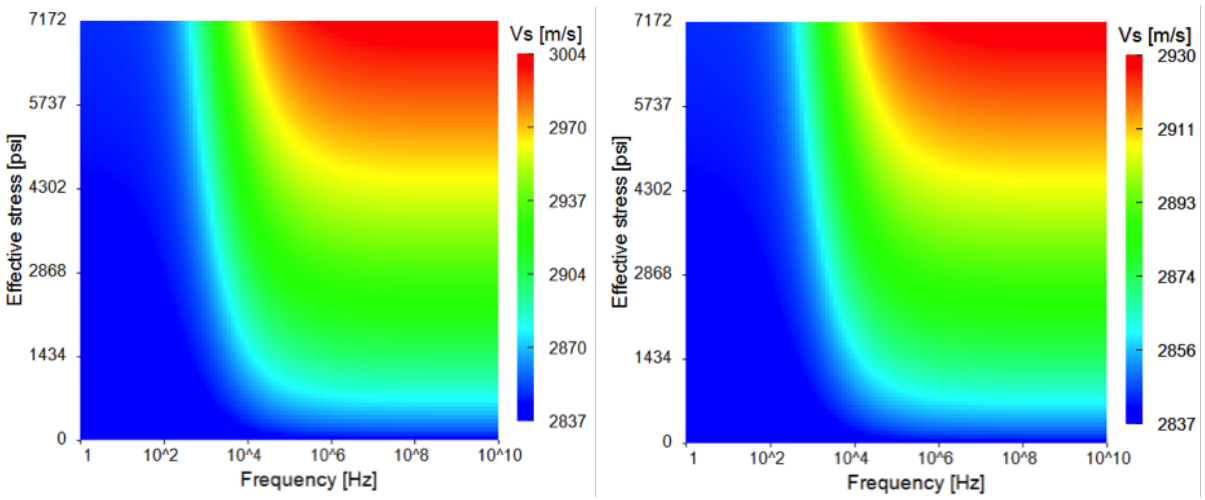

(a) With condensation (b) Without condensation

Figure 6.47: Effect of capillary condensation on shear velocity.

Table 6.7: Input parameters for theoretical model

Parameter	Value	Unit
Sphere Radius	3	μm
P-wave Velocity	4500	m/s
S-wave Velocity	2700	m/s
Poisson's Ratio	0.236	
Porosity	8	%
CO_2 Refraction Index	1.00045	
Dispersive Coefficient	0.001	
Rock Density	2.65	g/cm^3
Rock Dielectric Constant	6	
CO_2 Dielectric Constant	1.07	
Rock Refraction index	1.45	
Molarity	1	
Valence	1	
Zeta Potential	-30	mV
Collision Diameter	4.5E-10	cm
Gas Saturation	3.8	%
Structural Constant K_l	500	dyne/cm^2
Structural Constant l	1E-7	cm
Absorption Frequency	3E+15	s
Boltzman Coefficient	1.381E-23	m^{2}kg^{-2}K^{-1}
Ionic Concentration	6.02*10^{20}*M	ion/mol
Temperature	25	$^\circ$C
CO_2 Viscosity	0.0146	cp
CO_2 Density	1.784	kg/m^3
M. Depth	12736	ft
Young's Modulus	6.28E+6	psi
Shear Modulus	2.43E+6	psi

CHAPTER 7

CONCLUSIONS AND FUTURE STUDY RECOMMENDATIONS

"And once the storm is over, you won't remember how you made it through, how you managed to survive. You won't even be sure, whether the storm is really over. But one thing is certain. When you come out of the storm, you won't be the same person who walked in. That's what this storm's all about."

— Haruki Murakami, Kafka on the Shore —

In this chapter, a summary of my research results is presented with recommendations for further research and field application.

7.1 Summary and Remarks

The main objective of this research is to investigate the effect of capillary condensation on the geomechanical and acoustic properties of tight rocks. An experimental facility capable of conducting experiments at pressure up to 10,000 psi and temperature up to 100°C was built. The facility is equipped with a data collection system that allows collecting and analyzing acoustic and mechanical data during the experiment. CO_2 was used as pore fluid in this research to study the changes in acoustic and geomechanical properties of core samples from the Diyab and Austin Chalk formation.

The mechanical and acoustic characterization of the samples from the Austin Chalk and the Diyab formations was carried out experimentally using our state-of-the-art tri-axial facility. The pore size distribution for samples from the Diyab formation were characterized in our nitrogen adsorption experiments. The pore size characterization from nitrogen adsorption was used to estimate the pressure at which capillary condensation occurs.

A mathematical model was developed and validated with the experimental data. The model is capable of predicting the change of acoustic and mechanical properties with the changes in effective stress, temperature, pressure, frequency, and condensation.

Using the new experimental facility, we investigated the effect of CO_2 capillary condensation and observed a change in wave velocities and Young's Modulus as well as mechanical behavior at a pore pressure values around 750 - 800 psi for the Diyab and Austin Chalk samples tested. This indicates that CO_2 in nanopores of the core sample condenses at this pore pressure range which is in agreement with our model prediction. This confirms that condensation in nanopores occurs at a pressure lower than the bulk CO_2 dew point pressure of 977 psi at 27°C.

The results from this research provide the theoretical and experimental verification that acoustic measurements can be used as a method to detect the dew point and bubble point of fluids in the nanopores of tight formations.

7.2 Recommendation for Future Work

This research represents the first experimental endeavor of studying the effect of capillary condensation on nanopores and its effect on the acoustic and mechanical characteristics of tight samples. We succeeded in building an experimental facility capable of conducting such experimentation to be able to detect the signature of capillary condensation. This research sheds a light on formation characterization with condensation, and we therefore recommend to further investigate this phenomenon on the field-scale and to use acoustic data as a tool for monitoring the phase change during the lifecycle of the reservoir. This can help to identify the liquid bank around the wellbore and to determine whether condensation occurs in tight reservoirs. This could also be implemented in large-scale seismic surveys to monitor the phase change of fluid in the reservoir and to detect the condensation of gas near the wellbore.

Further experimental investigation would improve our understanding of this phenomenon. Due to facility restrictions, we were only able to use carbon dioxide as a pore fluid. Testing with different hydrocarbons would be beneficial as it better represents reservoir conditions. The findings from this research can be utilized to construct a phase envelope for tight formations accounting for the effect of nano-confinement by running a series of experiments at

different temperatures.

Finally, a new and improved set-up is being developed at our research center that could improve our understanding of changes in acoustic properties due to condensation. Processing the acoustic waveforms is sometime challenging and for that reason, a new cell is being built with the intention of addressing the tri-axial cell's shortcomings. This new smaller adsorption cell (Figure 7.1) is fitted with transducers while ensuring the chamber inside is leak-free. Therefore, we recommend using this new cell for future investigation.

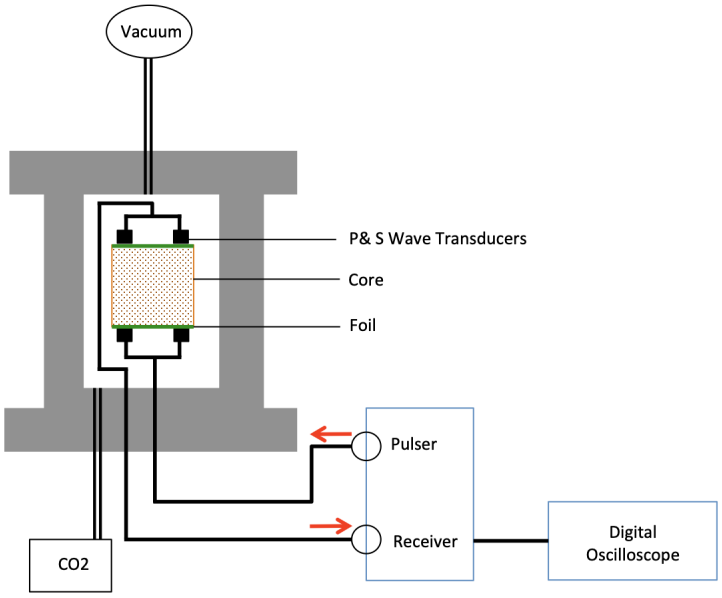

Figure 7.1: Schematic of new adsorption cell.

In the new set-up, the core sample is suspended in the cell and held by a coil. This is to ensure that the transducer crystals and the sample do not come in contact with the cell walls which could affect wave propagation and attenuation. Pore pressure is increased in stages and wave analysis is performed after each step. This set-up would be a significant improvement from than the tri-axial cell for the following reasons:

- Clearer ultrasonic waveforms since the wavelets travel a shorter distance and encounter less interfaces that could attenuate the waveform.

- No confinement/confining fluid is needed. This eliminates the possibility of cross-contamination between pore pressure fluid and confining fluid.
- The cores do not require to be perfectly lathed and flattened.
- Easier and faster to set-up/disassemble and does not require epoxy or curing time.
- Less pore fluid is used since the cell is smaller.

REFERENCES CITED

Alharthy, N. S., Nguyen, T., Teklu, T., Kazemi, H., and Graves, R. 2013. Multiphase Compositional Modeling in Small-Scale Pores of Unconventional Shale Reservoirs. Paper presented at the SPE Annual Technical Conference and Exhibition, New Orleans, Louisiana, USA, 30 September- 2 October. SPE 166306-MS.

Alqahtani, A. 2015. *The Role of Rock Composition, Organic Matter and Rock Fabric as Controlling Factors for Acoustic and Geomechanical Characteristics of Orgaic-rich Shales*. Ph.D. thesis, Colorado School of Mines.

Ambrose, R. J., Hartman, R. C., and Akkutlu, I. Y. 2010. Multi-component Sorbed-phase Considerations for Shale Gas-in-place Calculations. Paper presented at the SPE Production and Operations Symposium, Oklahoma City, Oklahoma, USA, 27-29 March. SPE-141416-MS.

Baig, M. Z., Van Laer, P., Leyrer, K., Makrachev, G., Almarzooqi, H., Alsuwaidi, S., Raina, I., and Dasgupta, S. 2017. Assessing Reservoir Quality of the Diyab Source Rock in UAE. Paper presented at the Abu Dhabi International Petroleum Exhibition Conference, Abu Dhabi, UAE, 13-16 November. SPE-188433-MS.

Barsotti, E., Tan, S. P., Saraji, S., Piri, M., and J., C. 2016. A Review on Capillary Condensation in Nanoporous Media: Implications for Hydrocarbon Recovery from Tight Reservoirs. *Fuel*, **184**: 344–361.

Bowers, G. L. 1995. Pore Pressure Estimation from Velocity Data: Accounting for Overpressure Mechanisms Besides Compaction. *SPE Drilling and Completions*, **10**(02).

Bui, B. T., Liu, H. H., Chen, J., and Tutuncu, A. N. 2016. Effect of Capillary Condensation on Gas Transport in Shale: A Pore-Scale Model Study. *SPE Journal*, **21**(02): 601–612.

Bui, B. T. and Tutuncu, A. N. 2014. Rock-fluid Interaction Impact on Geomechanical and Acoustic Properties of Shale Reservoirs: Anisotropic Grain Contact Adhesion Model. Paper presented at the Unconventional Resources Technology Conference, Denver, Colorado, USA, 25-27 August. URTEC-1921938-MS.

Bui, B. T. and Tutuncu, A. N. 2015. Effect of Capillary Condensation on Geomechanical and Acoustic Properties of Shale Formations. *Journal of Natural Gas Science and Engineering*, **21**(02): 1213–1221.

Chen, J., Mehmani, A., Li, B., Jin, G., and Georgi, D. 2013. Estimation of Total Hydrocarbon in the Presence of Capillary Condensation for Unconventional Shale Reservoirs. Paper presented at the SPE Middle East Oil and Gas Show and Conference, Manama, Bahrain, 10-13 March. SPE-166306-MS.

Chen, J., Zhang, J., Jin, G., Quinn, T., Frost, E., and Chen, J. 2012. Capillary Condensation and NMR Relaxation Time in Unconventional Shale Hydrocarbon Resources. Paper SPWLA-2012-186 presented at the SPWLA 53rd Annual Logging Symposium. Paper presented at the SPWLA 53rd Annual Logging Symposium, Cartagena, Columbia, 16-20 September. SPWLA-2012-186.

Civan, F., Rai, C. S., and Sondergeld, C. H. 2011. Shale-Gas Permeability and Diffusivity Inferred by Improved Formulation of Relevant Retention and Transport Mechanisms. *Transport in Porous Media*, **86**(3): 925–944.

Clarkson, C. R. and Haghshenas, B. 2013. Modeling of Supercritical Fluid Adsorption on Organic-Rich Shales and Coal. Paper presented at the SPE Unconventional Resources Conference, The Woodlands, Texas, USA, 10-12 April. SPE-164532-MS.

Curtis, M. E., Ambrose, R. J., and Sondergeld, C. H. 2010. Structural Characterization of Gas Shales on the Micro- and Nano-Scales. Paper presented at the Canadian Unconventional Resources and International Petroleum Conference, Calgary, Alberta, Canada, 19-21 October. SPE-137693-MS.

Didar, B. R. and Akkutlu, I. Y. 2013. Pore-Size Dependence of Fluid Phase Behavior and the Impact on Shale Gas Reserves. Paper presented at the SPE International Symposium on Oilfield Chemsitry, The Woodlands, Texas, USA, 8-10 April. SPE-164099-MS.

EIA. 2014. Annual Energy Outlook 2014 with Projections to 2040. Technical report, U.S. Energy Information Administration.

Espósito, R. O., Tavares, F. W., and Castier, M. 2005. Phase Equilibrium Calculations for Confined Fluids, Including Surface Tension Prediction Models. *Brazilian Journal of Chemical Engineering*, **18**(01): 27–37.

Fathi, E. and Akkutlu, I. Y. 2011. Lattice Boltzmann Method for Simulation of Shale Gas Transport in Kerogen. Paper presented at the SPE Annual Technical Conference and Exhibition, Denver, Colorado, USA, 30 October-2 Novemeber. SPE-146821-MS.

Gelb, L. D., Gubbins, K. E., and Radhakrishnan, R. 1999. Phase Separation in Confined Systems. *Reports on Progress in Physics*, **62**(12): 1573–1659.

Gor, G. Y., Paris, O., Prass, J., Russo, P. A., Ribeiro, M., and Neimark, A. V. 2013. Adsorption of n-Pentane on Mesoporous Silica and Adsorbent Deformation. *Langmuir*, **29**(27): 8601–8.

Gouth, F., Collell, J., and Galliero, G. 2013. Molecular Simulation to Determine Key Shale Gas Parameters, and Their Use in a Commercial Simulator for Production Forecasting. Paper presented at the EAGE Annual Conference Exhibition incorporating SPE Europec, London, UK, 10-13 June. SPE-164790-MS.

Gregg, S. J. and Sing, K. S. W. 1991. *Adsorption, Surface Area, and Porosity*. Second Edition. Ann Arbor, Michigan: Academic Press.

Gunther, G., Prass, J., Paris, O., and M., S. 2008. Novel Insights into Nanpore Deformation Casued by Capillary Condensation. *Physics Review Letter*, **101**(8): 20–3.

Gurevich, B., Maraynska, D., de Paula, O. B., and Pervukhina, M. 2010. A Simple Model for Squirt-Flow Dispersion and Attentuation in Fluid-Saturated Granular Rocks. *Geophysics*, **75**(6): 109–120.

Hovorka, S. D. and Nance, H. S. 1994. Dynamic Depositional and Early Diagenetic Processes in a Deep-Water Shelf Setting, Upper Cretaceous Austin Chalk. *Gulf Coast Association of Geological Societies*, **44**: 269–276.

Javadpour, F., Fisher, D., and Unsworth, M. 2007. Nanoscale Gas Flow in Shale Gas Sediments. *Journal of Canadian Petroleum Technology*, **46**(10): 16–21.

Karimi, S. and Kazemi, H. 2015. Capillary Pressure Measurement Using Reservoir Fluids in a Middle Bakken Core. Paper presented at the SPE Western Regional Meeting, Garden Grove, California, USA, 27-30 April. SPE-174065-MS.

King, M. S. 1966. Wave Velocities in Rocks as a Function of Changes in Overburden Pressure and Pore Fluid Saturants. *Geophysics*, **31**(1): 50–73.

Li, B., Mehmani, A., Chen, J., Georgi, D. T., and Jin, G. 2013. The Condition of Capillary Condensation and Its Effects on Adsorption Isotherms of Unconventional Gas Condensate Reservoirs. Paper presented at the SPE Annual Technical Conference and Exhibition, New Orleans, Louisiana, USA, 30 September- 2 October. SPE 166162-MS.

Li, W., Wang, C., Shi, Z., Wei, Y., Zhou, H., and Deng, K. 2016. The Description of Shale Reservoir Pore Structure Based on Method of Moments Estimation. *PLoS ONE*, **11**(3).

Li, Z., Jin, Z., and Firoozabadi, A. 2014. Phase Behavior and Adsorption of Pure Substances and Mixtures and Characterization in Nanopore Structures by Density Functional Theory. *Society of Petroleum Engineers*, **19**(06): 1096–1109.

Liu, X., Vernik, L., and Nur, A. 1994. Effects of Saturating Fluids on Seismic Velocities in Shale. Paper presented at the SEG Annual Meeting, Los Angeles, California, USA, 23-28 October. SEG-1994-1121.

Long, Y., Sliwinska, M. S., Drozdowski, H., Kempinski, M., Phillips, K. A., Palmer, J. C., and E., G. K. 2013. High Pressure Effect in Nanoporous Carbon Materials: Effects of Pore Geometry. *Colloids Surf a Physicochem Eng Aspects*, **437**: 33–41.

Loucks, R. G., Reed, R. M., Ruppel, S. C., and Hammes, U. 2012. Spectrum of Pore Types and Networks in Mudrocks and a Descriptive Classification from Matrix-Related Mudrock Pores. *AAPG Bulletin*, **96**(6): 1071–1098.

Lowell, S., Shields, J. E., Thomas, M. A., and Thommes, M. 2004. *Characterization of Porous Solids and Powders: Surface Area, Pore Size, and Density*. First Edition. Dordrecht, The Netherlands: Springer Netherlands.

Ma, Y., Chen, J. H., and Jamili, A. 2016. Adsorption and Capillary Condensation in Heterogeneous Nanoporous Shales. Paper presented at the Unconventional Resources Technology Conference, San Antonio, Texas, USA, 1-3 August. URTEC-2432657-MS.

Martin, R., Baihly, J. D., Malpani, R., Lindsay, G. J., and Atwood, W. K. 2011. Understanding Production from Eagle Ford-Austin Chalk System. Paper presented at the SPE Annual Technical Conference and Exhibition, Denver, Colorado, USA, 30 October-2 Novemeber. SPE-145117-MS.

Maske, H. A., Gland, N., Johnson, D. L., and Schwartz, L. 2004. Granular Packings: Nonlinear Elasticity, Sound Propagation and Collective Relaxtion Dynamics. *Physics Review E*, **70**(061302).

Mavko, G. M. 1979. Frictional Attenuation: An Inherent Amplitude Dependence. *Journal of Geophysical Research*, **84**: 4769–4776.

Mehmani, A., Prodanovic, M., and Javadpour, F. 2013. Multiscale, Multiphysics Network Modeling of Shale Matrix Gas Flows. *Transport in Porous Media*, **99**(2): 377–390.

Monson, P. A. 2005. Recent Progress in Molecular Modeling of Adsorption and Hysteresis in Mesoporous Materials. *Journal of the International Adsorption Society*, **11**(1): 29–35.

Morishige, K., Kawai, T., and Kittaka, S. 2014. Capillary Condensation of Water in Mesoporous Carbon. *Journal of Physical Chemistry*, **118**(9): 4664–4669.

Morishige, K. and Nakamura, Y. 2004. Nature of Adsorption and Desorption Branches in Cylinderical Pores. *Langmuir*, **20**(11): 4503–4506.

Murphy, W. F. 1982. *Effects of Microstructure and Pore Fluids on the Acoustic Properties of Granular Sedimentary Media*. Ph.D. thesis, Stanford University.

Murphy, W. F. 1984. Acoustic Measures of Partial Gas Saturation in Tight Sandstones. *Journal of Geophysical Research*, **89**(13): 11549–11559.

Murphy, W. F., Winkler, K. W., and Kleinberg, R. L. 1986. Acoustic Relaxation in Sedimentary Rocks: Dependence on Grain Contacts and Fluid Saturation. **51**(9): 757–766.

Naumov, S., Valiullin, R., Monson, P. A., and Karger, J. 2008. Probing Memory Effects in Confined Fluids Via Diffusion Measurements. *Langmuir*, **24**(13): 6429–6432.

Nelson, P. H. 2009. Pore-Throat Sizes in Sandstones. *AAPG Bulletin*, **93**(3): 329–340.

Nojabaei, B., Johns, R. T., and Chu, F. 2013. Effect of Capillary Pressure on Phase Behavior in Tight Rocks and Shales. *SPE Reservoir Evaluation Engineering*, **16**(3): 281–289.

O'Connell, R. J. and Budiansky, B. 1974. Seismic Velocities in a Dry and Saturated Cracked Solids. *Journal of Geophysical Research*, **79**(35): 5412–5426.

Palmer, I. D. and Traviolia, J. L. 1980. Attenuation by Squirt Flow in Undersaturated Gas Sands. *Geophysics*, **45**(12): 1780–1792.

Parsa, E., Yin, X., and Ozkan, E. 2015. Direct Observation of the Impact of Nanopore Confinement on Petroleum Gas Condensation. Paper presented at the SPE Annual Technical Conference and Exhibition, Houston, Texas, USA, 28-30 September. SPE-175118-MS.

Pendersen, K. S., Christensen, P. L., and Shaikh, J. A. 2007. *Phase Behavior of Petroleum Reservoir Fluids*. Second edition, Boca Raton, Florida: CRC Press, Taylor Francis Group.

Peselnick, L. and Outerbridge, W. F. 1961. Internal Friction in Shear and Shear Modulus of Solenhofen Limestone. *Journal of Geophysical Research*, **66**(2).

Rahmanian, M., Aguilera, R., and Kantzas, A. 2012. A New Unified Diffusion-Viscous-Flow Model Based on Pore-Level Studies of Tight Gas Formations. *Society of Petroleum Engineers*, **18**(01): 38–49.

Rowlinson, J. S. and Widom, B. 1982. *Molecular Theory of Capillarity*. First edition. Oxford, Oxfordshire: Clarendon Press.

Roy, S., Raju, R., Chuang, H. F., Cruden, B. A., and Meyyappan, M. 2003. Modeling Gas Flow through Microchannels and Nanopores. *Journal of Applied Physics*, **93**(8): 4870–4879.

Sandoval, D. R., Yan, W., Michelsn, M. L., and Stenby, E. H. 2016. The Phase Envelope of Multicomponent Mixtures in the Presence of The Phase Envelope of Multicomponent Mixtures in a Capillary Pressure Difference. *Industrial Engineering Chemistry Research*, **55**(22): 6530–6538.

Sangwichien, C., Aranovich, G. L., and Donohue, M. D. 2002. Density Functional Theory Predictions of Adsorption Isotherms with Hysteresis Loops, Colloids and Surfaces. *Physicochemical and Engineering Aspects*, **206**(1): 313–320.

Satik, C., Horne, R. N., and Yortsos, Y. C. 1995. A Study of Adsorption of Gases in Tight Reservoir Rocks. Paper presented at the SPE Annual Technical Conference and Exhibition, Dallas, Texas, USA, 22-25 October. SPE-30732-MS.

Seigh, S. K., Sinha, A., Deo, G., and Singh, J. K. 2009. Vapor-Liquid Phase Coexistence, Critical Properties, and Surface Tension of Confined Alkanes. *Journal of Petroleum Chemistry*, **113**(17): 7170–7180.

Shapiro, A. A. and Stenby, E. H. 1996. Effects of Capillary Forces and Adsorption on Reserves Distribution. Paper presented at the SPE European Petroleum Conference, Milan, Italy, 22-24 October. SPE-36922-MS.

Shapiro, A. A. and Stenby, E. H. 1997. Kelvin Equation for a Non-ideal Multicomponent Mixture. *Fluid Phase Equilibria*, **134**(1-2): 87–201.

Shapiro, S. A. 2003. Elastic Piezosensitivity of Porous and Fractured Rocks. *Geophysics*, **68**(2).

Sigal, F. R. 2013. Mercury Capillary Pressure Measurements on Barnett Core. *SPE Reservoir Evaluation Engineering*, **16**(04): 432–442.

Sing, K. and Williams, R. 2012. Historical Aspects of Capillarity and Capillary Condensation. *Micro-pore Meso-pore Mater*, **154**: 16–18.

Sondergeld, H. C., Ambrose, J. R., and Rai, S. C. 2010. Micro-Structural Studies of Gas Shales. Paper presented at the SPE Unconventional Gas Conference, Pittsburgh, Pennsylvania, USA, 23-25 February. SPE-131771-MS.

Spencer, J. W. 1981. Stress Relaxations at Low Frequencies in Fluid Saturated Rocks, Attenuation and Modulus Dispersion. *Geophysical Research Letters*, **86**(3): 1803–1812.

Tan, S. P. and Piri, M. 2015. Equation-of-State Modeling of Confined-Fluid Phase Equilibria in Nanopores. *Fluid Phase Equilibria*, **393**: 48–63.

Tanchoux, N., Trens, P., Maldonado, D., Di Renzo, F., and Fajula, F. 2004. The Adsorption of Hexane Over MCM-41 Type Materials. *Colloids and Surfaces A: Physicochemal and Engineering Aspects*, **246**(1-3): 1–8.

Tarazona, P., Marconi, M. B. U., and Evans, R. 1987. Phase Equilibria of Fluid Interfaces and Confined Fluids Non-local versus Local Density Functional. *Molecular Physics*, **60**(3): 573–595.

Teklu, T. W., Alharthy, N., Kazemi, H., Yin, X., Graves, R. M., and AlSumaiti, A. M. 2014. Phase Behavior and Minimum Miscibility Pressure in Nanopores. *SPE Reservoir Evaluation Engineering*, **17**(03).

Thommes, M., Kaneko, K., Neimark, A. V., Olivier, J. P., Rodriguez-Reinoso, F., Rouquerol, J., and Sing, K. S. W. 2015. Physisorption of Gases, with Special Reference to the Evaluation of Surface Area and Pore Size Distribtion. *Pure and Applied Chemistry*, **87**(9-10): 1051–1069.

Thomson, W. 1871. On the Equilibrium of Vapor at a Curved Surface of Liquid (Lord Kelvin). *Philosophical Magazine*, (42): 448–452.

Tittmann, B. R., Clark, V. A., Richardson, J. M., and Spencer, T. W. 1980. Possible Mechanisms for Seismic Attenuation in Rocks Containing a Small Amount of Volatiles. *Journal of Geophysical Research*, **85**(B10): 5199–5208.

Tutuncu, A. N. 1992. *Velocity Dispersion and Attenuation of Acoustic Waves in Granular Sedimentary Media*. Ph.D. thesis, University of Texas at Austin, Austin, Texas.

Tutuncu, A. N., Podio, A. N., and Sharma, M. M. 1993. Effect of Macro Fractures on Acoustic Properties of Rocks. Paper presented at the SEG Annual Meeting, Washington DC, USA, 26-30 Deptember. SEG-1993-0765.

Tutuncu, A. N. and Sharma, M. M. 1992. The Influence of Fluids on Grain Contact Stiffness and Frame Moduli in Sedimentary Rocks. *Geophysical Journal*, **57**(12): 1571–1583.

Umeda, K., Li, R., Sawa, Y., Yamabe, H., Liang, Y., Honda, H., Murata, S., Matsuoka, T., Akai, T., and Takagi, S. 2014. Multiscale Simulations of Fluid Flow in Nanopores for Shale Gas. Paper presented at the International Petroleum Technology Conference, Kuala Lumpur, Malaysia, 10-12 December. IPTC-17949-MS.

Vahrenkamp, V. C., Van Laer, P., Franco, B., Celentano, M. A., Grelaud, C., and Razin, P. 2015. Late Jurassic to Cretaceous Source Rock Prone Intra-Shelf Basins of the Eastern Arabian Plate - Interplay between Tectonism, Global Anoxic Events and Carbonate Platform Dynamics. Paper presented at the International Petroleum Technology Conference, Doha, Qatar, 6-9 December. IPTC-18470-MS.

Walton, J. P. R. B. and Quirke, N. 1989. Capillary Condensation: a Molecular Simulation Study. *Molecular Simulation*, **2**: 361–91.

Wang, H., Seltzer, S. J., Sun, B., Stallmach, F., Li, B., Thern, H., Mezzatesta, A., Arro, R., and Zhang, H. 2016. An NMR Experimental Study and Model Validation on Capillary Condensation of Hydrocarbons Confined in Shale Gas Condensate Reservoirs. Paper presented at the SPE Annual Technical Conference and Exhibition, Dubai, UAE, 26-28 September. SPE-181652-MS.

Whitson, C. H. and Brulé, M. R. 2000. *Phase Behavior*. Volume 20. SPE Monograph Series, Richardson, Texas.

Winkler, K. W. 1983. Contact Stiffness in Granular Porous Materials, Comparison Between Theory and Experiments. *Geophysical Research Letters*, **10**(11): 1073–1076.

Winkler, K. W. 1985. Dispersion Analysis of Velocity and Attenuation in Berea Sandstone. *Geophysical Research Letters*, **90**(B8): 6793–6800.

Winkler, K. W. and Nur, A. 1979. Pore Fluids and Seismic Attenuation in Rocks. *Geophysical Research Letters*, **6**(1).

Wyllie, M. R., Gregory, A. R., and Gardner, L. W. 1956. An Experimental Investigation of Factors Affecting Elastic Wave Velocities in Porous Media. *Geophysics*, **23**(2): 459–493.

Xiong, Y., Winterfeld, P. H., Wu, Y., and Huang, Z. 2014. Coupled Geomechanics and Pore Confinement Effects for Modeling Unconventional Shale Reservoirs. Paper presented at the Unconventional Resources Technology Conference, Denver, Colorado, USA, 25-27 August. URTEC-1923960-MS.

Yu, W., Sephernoori, K., and Patzek, T. W. 2016. Modeling Gas Adsorption in Marcellus Shale with Langmuir and BET Isotherms. *SPE Journal*, **21**(02).

Zarragoicoechea, J. G. and Kuz, A. V. 2004. Critical Shift of a Confined Fluid in a Nanopore. *Fluid Phase Equilibria*, **200**(1): 7–9.

Zhang, X., Xiao, L., Shan, X., and Guo, L. 2014. Lattice Boltzmann Simulation of Shale Gas Transport in Organic Nano-Pores. *Scientific Reports*, **4**(4843).